Faculty of Sciences

Department of Astrophysics, Geophysics, and Oceanography (AGO)

UR Spheres

Groupe Infra-Rouge de Physique Atmosphérique et Solaire (GIRPAS)

Assessing the success of the Montreal Protocol: trends of halogenated gases from ground-based, satellite, and model data

A dissertation presented in fulfilment of the thesis requirement for the degree of *Philosophiae Doctor* in Sciences at the University of Liège (College of Space Sciences)

by

Irene PARDO CANTOS

Academic Year 2024 – 2025

Jury members:

Emmanuel Mahieu	Supervisor	Université de Liège, Belgium
Denis Grodent	Jury chairman	Université de Liège, Belgium
Guy Munhoven	Secretary	Université de Liège, Belgium
Andreas Engel	External examiner	Goethe-Universität Frankfurt, Germany
Bruno Franco	External examiner	Université Libre de Bruxelles, Belgium
Yao Té	External examiner	Sorbonne Université, France

A Bagheera,
mi panterita, mi todo.

Acknowledgements

This thesis is not only the final step of an intense period of my life but the culmination of all the efforts I have made since the beginning of my academic journey. Learning to become a scientist has been a dream come true, and I must acknowledge the many people who have contributed to this journey.

First, I would like to thank my thesis jury for accepting to read this work and for helping me grow as a scientist. I hope you enjoy reading this text as much as I enjoyed writing it, at least on most days!

Merci au département AGO et à l'Université de Liège qui m'ont donné l'opportunité de commencer mon aventure belge en 2015 avec un Erasmus, et qui m'ont fait sentir le besoin de revenir en 2017 pour continuer à apprendre et vivre des merveilleuses aventures. Merci de m'avoir permis de découvrir ce passionnant métier. Merci spécialement à Michäel et Angela de toujours veiller au bien-être de vos collègues. C'est merveilleux de vous avoir rencontrés. Merci également à Louis et Guy de m'avoir confié une partie de vos cours et de m'avoir permis d'exercer mon deuxième métier de rêve, l'enseignement.

Merci à mon comité de thèse. À Denis pour être un si bon conseiller, guide et même psychologue. Et à Guy de m'avoir appris autant, scientifiquement, pédagogiquement et humainement, ainsi que de tenir toujours en compte mon avis. Merci à tous les deux d'être des si bons scientifiques, collègues et belles personnes. Je ne me suis pas trompée quand je vous ai choisis pour me suivre dans cette étape de ma vie.

Merci à toute l'équipe du GIRPAS, anciens et actuels collègues. Merci à mon promoteur, Manu, de m'avoir donné l'opportunité d'apprendre le merveilleux métier de chercheur et d'avoir toujours ta porte ouverte pour m'écouter. Ton positivisme m'a aidé à croire en moi et à arriver à cette étape finale. Merci Diane d'être la pièce indispensable pour maintenir l'équipe unie et nous offrir des bons chocolats pour apporter un peu de sucre à nos cerveaux. Je tiens à remercier également Maxime, de m'avoir aidé au démarrage de ma thèse malgré la mauvaise situation sanitaire. Merci aussi au dernier arrivé, Florentin, que j'ai pu voir grandir en tant que scientifique, bon courage pour la suite ! Merci énormément à Olivier et PH, sans vous, nous ne pourrions sans doute pas effectuer nos recherches. Je n'oublie pas nos collègues congolais, qui ont apporté une collaboration magnifique et une touche culturelle toujours bienvenue.

Thanks to the NDACC network and its members for the enriching exchanges and collaboration. Through our work, we can better understand the state and evolution of the Earth's atmosphere. Thanks also to our colleagues from the AGAGE network for sharing their observations and allowing me to improve my work.

Muchas gracias Omaira por enseñarme tanto y compartir conmigo esas dos semanas en la

preciosa Tenerife. Me has dado el último empujón para poder terminar este trabajo y apreciar todavía más la importancia del mismo. Espero que podamos seguir colaborando juntas.

Merci aux extraordinaires Maïté et Clémentine qui m'ont accueillie à mon début en tant qu'assistante. Merci pour les bons conseils et les bons moments partagés dans les labos de physique. Vous êtes beaucoup plus que des collègues.

Merci à toute l'équipe des Young Minds Liège avec qui j'ai pu partager des extraordinaires moments en diffusant la science. Merci Antoine, Guillaume et Linus pour la belle équipe que nous faisons.

Gracias a todos los profesores que me han acompañado durante toda mi vida, desde que empecé a leer y colorear. Gracias a vosotros he podido escribir este texto y comprender cómo funciona una pequeña parte del mundo. Me gustaría agradecer especialmente a Trini, ¡la gran maestra! Así como a Rafael Pérez Mengual, por hacerme amar las matemáticas, y a Rafael Garcia Molina, por enseñarme a transmitir la ciencia y hacer que la gente disfrute al aprender, al igual que yo lo hago.

Gracias a mi cuarteto infernal, porque hemos crecido y casi nacido juntas. Espero que podamos seguir compartiendo cada una de las etapas de nuestras vidas. Gracias también a mis bailarines, por compartir esa sensibilidad y buenos momentos que espero que podamos seguir disfrutando pese a la distancia. Gracias Ana por los tantos paseos y conversaciones que hemos tenido, es tan fácil hablar y disfrutar contigo! Te echo mucho de menos. Sois familia.

Gracias a mis colombianas bellas que siempre están ahí creyendo en mí y animándome. No soy tan cerebrito como vosotras creéis, pero parece que estoy a un paso de terminar esta etapa. Gracias por compartirla conmigo y vivir tantos momentos juntas. Gracias a Enzo, mi gran amigo y confidente, que la distancia y el tiempo no nos separe nunca. Nos vemos muy pronto para tomar un mate en el otro lado del mundo. Merci également à Mathieu, qui trouve toujours le moyen de nous faire rire et nous donner de l'énergie.

Merci a tous les amis que j'ai rencontrés en Belgique et qui m'ont fait aimer encore plus ce merveilleux pays. Vous m'avez fait me sentir une parmi vous et vous m'avez appris énormément de choses qui m'ont fait grandir et m'améliorer comme personne.

Merci Bagheera, ma petite panthère, pour toutes les heures d'écriture pendant lesquelles tu m'as accompagnée et encouragée sans dire un seul mot. Merci de m'avoir appris toute une nouvelle forme d'amitié et amour.

Gracias a toda mi familia, especialmente a mis padres, por haberme educado y regalado la oportunidad de estudiar y crecer como persona. Sin vosotros, yo no estaría aquí hoy. Gracias a mi hermano, por escucharme y haber estado orgulloso de cada uno de mis éxitos.

Finalement, je souhaiterais remercier Benji pour tes encouragements, ta confiance, ton inspiration et tes relectures. Merci d'être toujours là, à la fin de chacune de mes étapes académiques, avec un grand sourire, de bons conseils et la paix dont j'ai besoin pour réussir. Gracias por compartir tu vida conmigo. Gracias por creer en mí. Tu es mon plus beau projet.

Abstract

Our atmosphere acts as a protective shell, sustaining life on Earth and protecting ecosystems. Its current state and evolution over the past century have become a major concern for the scientific community and the general population. Two primary issues are considered: the reduction of the ozone layer and global warming. To protect the ozone layer, the Montreal Protocol was signed in 1987 and has proven successful, as evidenced by the observed reduction of ozone-depleting substances, such as chlorofluorocarbons (CFCs). When CFCs reach the stratosphere, they undergo photodissociation, releasing chlorine atoms that contribute to ozone destruction. Through various decisions and amendments to the Protocol, these substances have been replaced by alternatives with reduced contributions to ozone depletion, such as hydrochlorofluorocarbons (HCFCs) and hydrofluorocarbons (HFCs), the last ones not contributing to ozone depletion. However, HFCs emerged as highly potent greenhouse gases, leading to the Kigali Amendment (2016) which aims at controlling their use. Monitoring the atmospheric evolution of gases regulated by the Montreal Protocol requires long-term, high-quality measurements to track trends and assess the impact of international regulations.

This research analyses long-term data on halogenated gases using ground-based Fourier Transform Infrared (FTIR) spectroscopy, TOMCAT 3-D model simulations, *in situ* measurements, and satellite observations, as well as advanced statistical tools for trend analysis. Initially, it was observed that the decline of atmospheric CFC-11 had slowed, likely due to undeclared production and emissions. To investigate this unexpected phenomenon, measurements from two NDACC stations were used: the Jungfraujoch station in the Swiss Alps and the Lauder station in New Zealand. For the first time, the Jungfraujoch CFC-11 time series was harmonised, enabling its analysis on an extended time period, ranging from 1986 to 2020. The results revealed a slowdown in the CFC-11 decay starting in 2011 in the Northern Hemisphere and in 2014 in the Southern Hemisphere. This delay is explained by the transport time from the Northern Hemisphere, where most emissions occur, to the Southern Hemisphere.

This thesis also explores, for the first time using ground-based FTIR spectra, the detection of HFC-134a, the most abundant HFC. An optimal spectral window was identified to minimise interference from other gases, making possible the total column retrievals at other NDACC stations. The FTIR retrievals of HFC-134a were consistent with other measurement methods, indicating a continuous increase in its concentration of about 7% per year since the early 2000s. The effects of the Kigali Amendment are expected to become observable in the coming years, motivating the expansion of this work to other stations and in the future.

The importance of continuous atmospheric monitoring has been demonstrated, along with the need for near-global coverage to better understand changes in atmospheric composition and detect potential undeclared production of harmful substances.

Résumé

Notre atmosphère agit comme une enveloppe protectrice, permettant la vie sur Terre et protégeant les écosystèmes. Son état actuel et son évolution lors du dernier siècle ont suscité de vives inquiétudes dans la communauté scientifique et la population en général. Deux grandes problématiques sont en jeu : l'amincissement de la couche d'ozone et le réchauffement global. Afin de protéger la couche d'ozone, le Protocole de Montréal a été signé en 1987 et il s'est révélé efficace, comme en témoigne la réduction des substances appauvrissant la couche d'ozone, tels que les chlorofluorocarbures (CFCs). Lorsque les CFCs atteignent la stratosphère, ils sont photodissociés, libérant des atomes de chlore qui contribuent à la destruction de l'ozone. Suite à plusieurs décisions et amendements au Protocole, ces substances ont été remplacées par des alternatives avec des contributions réduites à l'amincissement de la couche d'ozone, comme les hydrochlorofluorocarbures (HCFCs), ou encore par la suite les hydrofluorocarbures (HFCs), ces derniers ne contribuant pas à la destruction de l'ozone. Néanmoins, les HFCs sont de très puissants gaz à effet de serre, motivant l'adoption de l'Amendement de Kigali (2016) qui contrôle leur utilisation. La surveillance de l'évolution atmosphérique des gaz régulés par le Protocole de Montréal exige des observations de haute qualité et sur le long terme afin de pouvoir ainsi caractériser avec précision leurs concentrations et évaluer l'impact des réglementations internationales.

La recherche réalisée lors de cette thèse analyse des données à long terme de gaz halogénés en utilisant la spectroscopie infrarouge à transformée de Fourier (FTIR, de l'anglais Fourier Transform Infrared spectroscopy), des simulations du modèle 3-D TOMCAT, des mesures *in situ* et des observations par satellite, ainsi que des outils statistiques avancés pour l'analyse de tendances. Initialement, il avait été observé que la décroissance du CFC-11 atmosphérique présentait un ralentissement, résultant probablement de productions et d'émissions non-déclarées. Pour examiner ce phénomène inattendu, des mesures prises depuis deux stations du NDACC ont été utilisées : la station du Jungfraujoch dans les Alpes suisses et la station Lauder en Nouvelle-Zélande. La série temporelle du CFC-11 au Jungfraujoch a été soigneusement harmonisée, permettant ainsi et pour la première fois son analyse sur une période prologée, s'étendant de 1986 à 2020. Les résultats ont révélé un ralentissement de la décroissance du CFC-11 à partir de 2011 dans l'hémisphère Nord et depuis 2014 dans l'hémisphère Sud. Ce retard s'explique par le temps nécessaire au transport des masses d'air de l'hémisphère Nord, où la plupart des émissions ont lieu, jusqu'à l'hémisphère Sud.

Cette thèse explore également, pour la première fois avec des données obtenues par spectroscopie FTIR au sol, la détection du HFC-134a, le HFC le plus abondant. Une fenêtre spectrale optimale a été identifiée pour réduire au maximum les interférences d'autres gaz, permettant ainsi la restitution (en anglais, retrieval) des colonnes totales dans d'autres stations du réseau NDACC. Les retrievals FTIR du HFC-134a obtenus sont concordants avec d'autres méthodes

de mesure et ont indiqué une augmentation de sa concentration d'environ 7% par an depuis le début des années 2000. Les effets de l'Amendement de Kigali seront probablement perceptibles dans les années à venir, motivant l'extension de ce travail à d'autres stations et dans le futur.

Cette thèse a montré l'importance d'une surveillance de l'atmosphère en continu, ainsi que le besoin d'une couverture quasi-globale pour mieux comprendre les changements dans la composition atmosphérique à échelle mondiale et détecter des potentielles productions non-déclarées de substances nocives.

Resumen

Nuestra atmósfera actúa como una coraza protectora, permitiendo la vida en la Tierra y protegiendo los ecosistemas. Su estado actual y su evolución a lo largo del último siglo se han convertido en una inquietud principal de la comunidad científica y la población en general. Dos problemas principales están en juego: la disminución de la capa de ozono y el calentamiento global. Para proteger la capa de ozono, el Protocolo de Montreal fue firmado en 1987 y ha demostrado su éxito, como manifiesta la reducción de sustancias agotadoras de la capa de ozono, tales como los clorofluorocarbonos (CFCs). Cuando los CFCs llegan a la estratosfera son fotodisociados, liberando átomos de cloro que contribuyen a la destrucción del ozono. A través de varias decisiones y enmiendas al Protocolo, estas sustancias se han remplazado por alternativas con contribuciones reducidas al agotamiento del ozono, como los hidroclorofluorocarbonos (HCFCs) y los hidrofluorocarbonos (HFCs), estos últimos no contribuyendo a la destrucción del ozono. Sin embargo, los HFCs son gases de efecto invernadero muy potentes, llevando a la adopción de la Enmienda de Kigali (2016), creada con el objetivo de controlar su uso. La vigilancia de la evolución atmosférica de los gases regulados por el Protocolo de Montreal exige observaciones de alta calidad y a largo plazo para así poder caracterizar con precisión sus concentraciones y evaluar el impacto de las normativas internacionales.

La investigación realizada en esta tesis analiza los datos a largo plazo de gases halogenados, utilizando la espectroscopía infrarroja por transformada de Fourier (FTIR, del inglés Fourier Transform Infrared spectroscopy), simulaciones del modelo 3-D TOMCAT, medidas *in situ* y observaciones por satélite, así como herramientas estadísticas avanzadas para el análisis de tendencias. Inicialmente, se observó que el CFC-11 atmosférico estaba reduciéndose a una velocidad cada vez menor, debido probablemente a una producción y unas emisiones no declaradas. Para examinar este fenómeno inesperado se han utilizado medidas tomadas desde dos estaciones de la red NDACC: la estación de Jungfraujoch en los Alpes suizos y la estación Lauder en Nueva Zelanda. La serie temporal del CFC-11 de Jungfraujoch ha sido cuidadosamente harmonizada por la primera vez, permitiendo el análisis de un período prolongado, desde 1986 hasta 2020. Los resultados revelan una ralentización de la disminución del CFC-11 a partir de 2011 en el hemisferio norte y a partir de 2014 en el hemisferio sur. Este retraso se explica por el tiempo necesario para el transporte de las masas de aire del hemisferio norte, donde la mayoría de las emisiones tienen lugar, hasta el hemisferio sur.

Esta tesis explora igualmente la detección del HFC-134a, el HFC más abundante, utilizando por primera vez datos obtenidos por espectroscopía FTIR desde Tierra. Se ha identificado una ventana espectral óptima para minimizar las interferencias de otros gases, haciendo posible la recuperación (del inglés, retrieval) de las columnas totales en otras estaciones NDACC. Los retrievals FTIR del HFC-134a obtenidos concuerdan con otros métodos de medición e indican un aumento de su concentración aproximado de 7% al año desde el principio de la década de los

2000. Probablemente, los efectos de la Enmienda de Kigali serán perceptibles en los próximos años, lo que motiva la ampliación de este trabajo en el fututo así como a otras estaciones.

Esta tesis demuestra la importancia de una vigilancia de la atmósfera de forma continua, así como la necesidad de una cobertura casi global para entender mejor los cambios en la composición atmosférica a escala mundial y detectar una potencial producción no declarada de sustancias nocivas.

Contents

Glossary of Acronyms

ACE Atmospheric Chemistry Experiment

ACE-FTS ACE-Fourier Transform Spectrometer

AEMet Agencia Estatal de Meteorología

AGAGE Advanced Global Atmospheric Gases Experiment

AGO Astrophysics, Geophysics, and Oceanography

ALE Atmospheric Lifetime Experiment

AWB Auto-regressive Wild Bootstrap

BDC Brewer-Dobson Circulation

CFC Chlorofluorocarbon

CMIP6 Coupled Model Intercomparison Project Phase 6

CTM Chemical Transport Model

DCC Danish Climate Center

DMI Danish Meteorological Institute

DOFS Degrees Of Freedom for Signal

DPC Dry air Pressure Column

ECMWF European Centre for Medium-range Weather Forecasts

ECD Electron Capture Detector

EESC Equivalent Effective Stratospheric Chlorine

ESRL Earth System Research Laboratories

FOV Field Of View

FTIR Fourier Transform Infrared

FTS Fourier Transform Spectrometer

FWHM Full Width at Half-Maximum

GAGE Global Atmospheric Gases Experiment

GC Gas Chromatographic

GC-ECD Gas Chromatograph with Electron-Capture Detectors

GC-FID Gas Chromatograph with Flame-Ionization Detectors

GC-HgORD Gas Chromatograph with Mercuric Oxide (HgO) Reduction Detectors

GC-MSD Gas Chromatograph with Mass Spectrometric Detectors

GCM General Circulation Model

GCMS Gas Chromatography with Mass Spectrometry

GCMS-ADS GCMS adsorption/desorption

GHG Greenhouse gas

GWP Global Warming Potential

HCFC Hydrochlorofluorocarbon

HFC Hydrofluorocarbon

HITRAN HIgh-resolution TRANsmission molecular absorption database

IASB/BIRA Royal Belgian Institute for Space Aeronomy

ICAyCC Instituto de Ciencias de la Atmósfera y Cambio Climático

ILS Instrument Line Shape

IMK-IFU Karlsruhe Institute of Technology - Institute for Meteorology and Climate Research

IPCC Intergovernmental Panel on Climate Change

IR Infrared

IRWG Infrared Working Group

ITCZ InterTropical Convergence Zone

JFJ Jungfraujoch

JPL Jet Propulsion Laboratory

LACy Laboratoire de l'Atmosphère et des Cyclones

LAU Lauder

LEO Low Earth Orbit

MAESTRO Measurement of Aerosol Extinction in the Stratosphere and Troposphere Retrieved by Occultation

MCT Mercury Cadmium Telluride

MW Micro-Window

NASA National Aeronautics and Space Administration

NCEP National Centers for Environmental Prediction

NDACC Network for the Detection of Atmospheric Composition Change

NDSC Network for the Detection of Stratospheric Change

NH Northern Hemisphere

NIWA National Institute of Water and Atmospheric research

NOAA National Oceanic and Atmospheric Administration

ODP Ozone Depletion Potential

ODS Ozone-Depleting Substance

OEM Optimal Estimation Method

OLS Ordinary Least Squares

OPD Optical Path Difference

PBL Planetary Boundary Layer

PFC Perfluorocarbon

PLL Pseudo-LineList

PSC Polar Stratospheric Clouds

RMS Root Mean Square

SH Southern Hemisphere

SIO Scripps Institution of Oceanography

SNR Signal-to-Noise Ratio

SSP Shared Socioeconomic Pathway

SZA Solar Zenith Angle

TCO Total Column Ozone

TOA Top Of the Atmosphere

UCAR University Corporation for Atmospheric Research

UCI University of California, Irvine laboratory

UNFCCC United Nations Framework Convention on Climate Change

UTC Coordinated Universal Time

UV Ultraviolet

VMR Volume Mixing Ratio

VOC Volatile Organic Compound

VSLS Very Short-Lived Substance

WACCM Whole Atmosphere Community Climate Model

WG Working Group

WMO World Meteorological Organisation

ZPD Zero Path Difference

List of Figures

List of Tables

Chapter 1

The atmosphere of the Earth

1.1 Introduction

The Earth is the third planet from the Sun, after Mercury and Venus, and the fifth largest in the solar system. It is the only planet in the solar system covered by liquid water, thanks to its favorable temperatures. The great oceans cover nearly 70% of the Earth's surface and contain 97% of the planet's water, allowing life to emerge on Earth about 3.8 billion years ago. Today, it remains the only planet in the solar system where life, as we know it, is possible.

Our planet is enveloped by an atmosphere, a mixture of gases that protects ecosystems and enables life. Earth's atmosphere is mainly composed of nitrogen and oxygen, along with other gases, playing distinct and important roles in maintaining the planet's energy balance, regulating temperature, and filtering the energetic ultraviolet (UV) radiation. This protective layer shields Earth's surface not only from harmful radiation but also from meteoroids, and influences both short-term local weather and long-term global climate.

1.2 The vertical structure of the Earth's atmosphere

In the Earth's atmosphere, pressure and density decrease, almost exponentially, with altitude due to gravity. The atmosphere is said to be stably stratified or divided into different layers based on temperature variations: the troposphere, the stratosphere, the mesosphere and the thermosphere (Andrews, 2010; Jacob, 1999). These layers are separated by boundaries, called "pauses", defined by changes in the temperature profile (red curve in Figure 1.1). The **troposphere** is the lowest atmospheric layer, extending from the surface to 7 – 17 km altitude, depending on latitude and season. The upper boundary of the troposphere is called **tropopause**. At the poles, the tropopause height is at its lowest (7 – 8 km) due to the cold air masses, whereas in the tropics, the troposphere is thickest (16 – 17 km), because of the maximum sunlight received in this region, producing significant air convection processes. The troposphere is characterised by a decrease of temperature (a negative temperature gradient) caused by several factors. As altitude increases, density and pressure decrease, leading to fewer collisions between the air molecules as well as to the expansion of air, which cools down. Additionally, higher air particles undergo less heating from Earth's infrared (IR) radiation and from greenhouse gases near the surface (especially water vapour). In the troposphere, convective instability and turbulences occur, generating weather phenomena (Brasseur and Solomon, 2005; Shepherd, 2003). The **stratosphere** spans from the tropopause to about 50 km, where the **stratopause** lies. This layer is characterised by an increase in temperature with altitude (a positive temperature gra-

dient) due to the absorption of UV solar radiation by the ozone layer (see Section 1.3.3). The temperature reaches a maximum at about 50 km. Consequently, the stratospheric air is more stable than tropospheric air, impeding vertical air movement (Brasseur and Solomon, 2005). Above the stratopause, the **mesosphere** exhibits decreasing temperatures with altitude. A minimum temperature occurs between 85 and 100 km, indicating the upper boundary of this layer, the **mesopause**. Most meteors burn up completely crossing the mesosphere. These three layers together are known as the **homosphere** because the primary components are N_2 and O_2, and the mean molecular weight of air remains relatively constant within this region (Brasseur and Solomon, 2005). The portion of total atmospheric weight above an altitude z is equal to P(z)/P(0), where P(0) is the pressure at sea level (P(0) = 1000 hPa). As it is shown in Figure 1.1, atmospheric pressure decreases to 0.01 hPa around 80 km altitude, involving that 99.999% of the atmosphere lies below this altitude (Jacob, 1999).

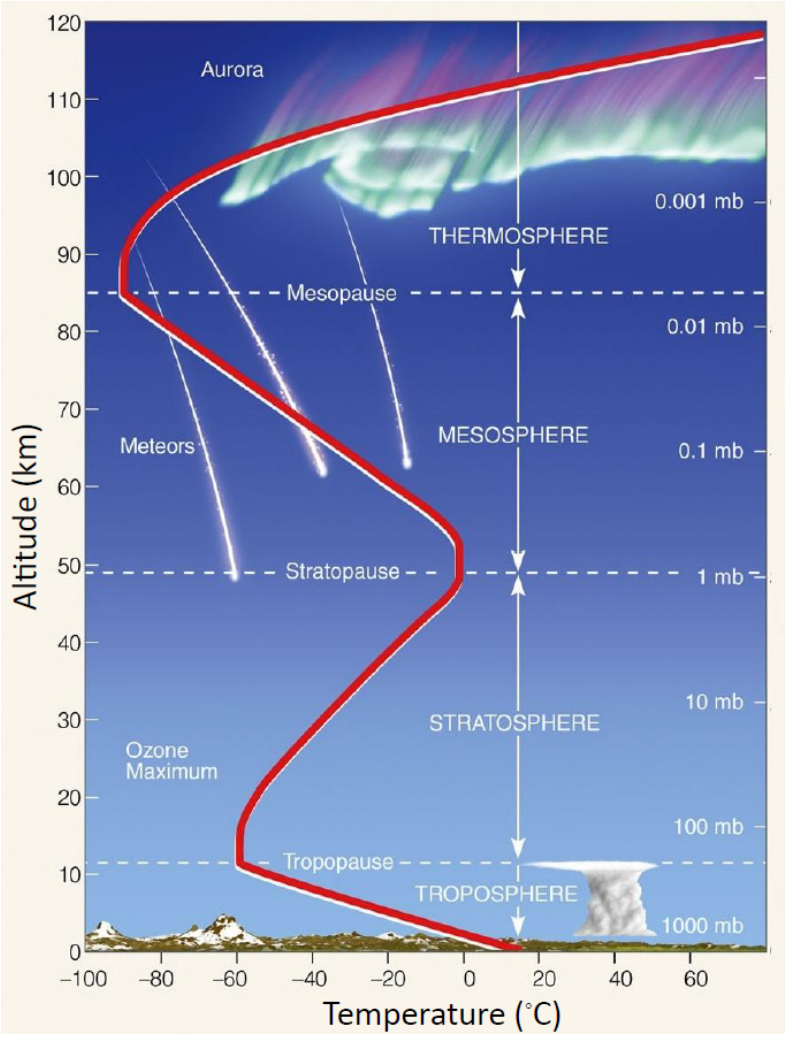

Figure 1.1. Vertical structure of the atmosphere. The red curve represents the temperature profile. The left vertical axis indicates the altitude in kilometers, while the right vertical axis indicates the atmospheric pressure in milibars (1 mbar = 1 hPa). The horizontal axis indicates the temperature in °C. Adapted from Ahrens (2001).

The **thermosphere** extends above the mesopause and is characterised by very high temperatures caused by the absorption of energetic UV solar radiation. Auroras occur in this layer, and the International Space Station (ISS) orbits within it at an altitude of around 400 km. Above

approximately 130 km, the relative concentration of atomic oxygen increases with altitude, eventually exceeding the O_2 and N_2 abundances, which decrease because of photodissociation. In the upper thermosphere, atomic hydrogen (H) becomes the major constituent. Since the molecular weight of air changes with altitude, this region is also known as the **heterosphere**. Above the **thermopause**, lies the **exosphere**, the most external layer of the atmosphere, which gradually merges with outer space. The boundary between the thermosphere and the exosphere is not well outlined, lying somewhere between 500 and 1000 km (Brasseur and Solomon, 2005; UCAR, 2024).

1.3 The composition of the Earth's atmosphere

The Earth's atmosphere is mainly composed of nitrogen (about 78%) and oxygen (21%). The remaining 1% includes other gases such as argon, water vapour, carbon dioxide, ozone, methane, nitrous oxide and other trace gases such as the chlorofluorocarbons (CFCs) (Andrews, 2010; WMO, 2022). Many of these gases absorb and re-emit infrared radiation, influencing Earth's temperature. They are collectively known as greenhouse gases. In this section, we will explain the importance of these gases, as well as the role of stratospheric ozone in protecting Earth's ecosystems from harmful solar radiation.

1.3.1 The Earth's surface temperature

To understand the observed surface temperature in simple terms, this section explains some key concepts related to the energy balance between solar radiation[1] and Earth's radiation[2]. First, we consider a model of the atmosphere without greenhouse gases and discuss why the observed temperature does not align with this model. Then, we incorporate greenhouse gases to analyse their effect on surface temperature. In both models, the presence of clouds is ignored.

1.3.1.1 An atmosphere without greenhouse gases

The solar constant is defined as the solar power per unit area at the top of the Earth's atmosphere at a mean distance from the Sun. This value is $S_0 = 1361.1 \pm 0.5$ Wm^{-2} (Gueymard, 2018). Since solar beams are considered parallel due to the large distance between the Sun and the Earth, the energy received by the Earth's surface is confined to a disk with a cross section of πR^2. Consequently, the total solar energy received per unit time (power) is $S_0 \pi R^2$. The Earth's albedo (α) represents the portion of solar energy reflected directly back to the space. Therefore, the incoming solar power reflected by the Earth is $S_0 \pi R^2 \alpha$. Assuming the Earth as a black body that emits uniformly at a temperature T, according to the Stefan-Boltzmann law, the power emitted per unit area by the planet is σT^4, where σ is the Stefan-Boltzmann constant ($\sigma = 5.67 \cdot 10^{-8}$ $Wm^{-2}K^{-4}$). The total power emitted by the Earth is $4\pi R^2 \sigma T^4$ (in all directions) (Andrews, 2010).

[1] Solar (or short-wave) radiation corresponds to UV, visible and near IR wavelenghts (between ≈ 0.1 and 4 μm).

[2] Thermal (or long-wave) radiation is emitted by the surface and atmosphere of the Earth and corresponds to thermal IR and far IR wavelenghts (between ≈ 4 and 100 μm).

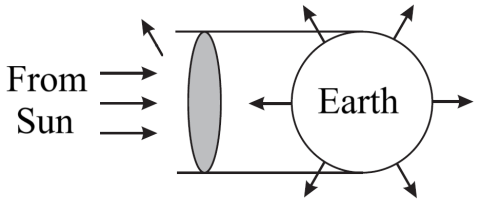

Figure 1.2. Simplified sketch where the incident solar radiation is represented by the parallel horizontal arrows, the reflected solar radiation by the left-diagonal arrow, and the outgoing thermal radiation of the Earth by the radial arrows. Adapted from Fig. 1.1 from Andrews (2010).

Assuming that all this power is transmitted into space and not absorbed by the atmosphere (i.e., no clouds or greenhouse gases), and considering that the Earth is in thermal equilibrium, the incoming and outgoing powers are balanced:

Solar intercepted power – Solar reflected power = Power emitted by the Earth

$$S_0 \pi R^2 - S_0 \pi R^2 \alpha = 4\pi R^2 \sigma T^4 \tag{1.1}$$

And then, the temperature of the Earth is:

$$T = \left(\frac{S_0(1-\alpha)}{4\sigma} \right)^{1/4} \tag{1.2}$$

The temperature T is referred to as the **effective temperature of the Earth** and is estimated to be around 255 K (-18 °C), considering a planetary albedo of 0.3. However, this value is lower than the observed average surface temperature, $T_{obs} \approx 288$ K (15 °C) (Andrews, 2010). To account for this discrepancy, we must consider a model with an absorbing atmosphere.

1.3.1.2 An atmosphere with greenhouse gases

We consider an atmosphere with a uniform temperature T_a. We consider that the atmosphere absorbs a fraction of the incoming solar radiation (shortwave) and a fraction of the emitted thermal infrared radiation (longwave). These fractions are called absorptances[3] and are represented by ε_{sw} for solar radiation, and ε_{lw} for IR radiation. The remaining energy is transmitted through the atmosphere (Andrews, 2010).

The incoming solar irradiance (power per unit area) which is not reflected by the planet is equal to:

$$F_{TOA} = \frac{S_0(1-\alpha)}{4} \tag{1.3}$$

at the top of the atmosphere (TOA). A fraction of the incident energy is absorbed by the atmosphere, $\varepsilon_{sw} F_{TOA}$, while the rest is absorbed by the surface, $(1-\varepsilon_{sw}) F_{TOA}$.

[3] In thermal equilibrium conditions, the emittance of a body is equal to its absorptance, according to the Kirchoff law.

The Earth's surface emits longwave radiation as a black body:

$$F_g = \sigma T_g^4 \tag{1.4}$$

where T_g is the ground temperature.

A fraction of the emitted energy is absorbed by the atmosphere, $\varepsilon_{lw} F_g$, while the rest escapes directly to space, $(1 - \varepsilon_{lw})F_g$. Assuming the atmosphere acts as a grey body with emittance ε_{lw}, it emits longwave radiation, $F_a = \varepsilon_{lw}\sigma T_a^4$, in all directions. Here, we consider only upwards and downwards to simplify the diagram.

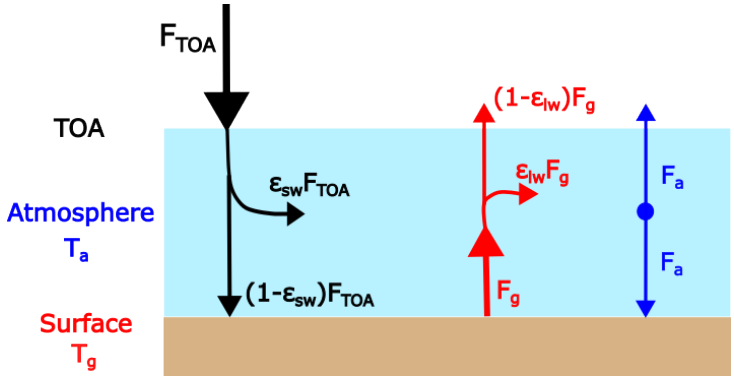

Figure 1.3. Simplified model of the greenhouse effect. From top to bottom: the top of the atmosphere (TOA), a one-layer atmosphere (in blue) and the ground (in brown). The atmosphere is considered to be at a temperature T_a and the ground at T_g. Solar irradiances are represented by the black arrows, while the surface's and atmosphere's irradiances are shown in red and blue, respectively.

Neglecting non-radiative energy processes, the Earth-atmosphere system is considered to be in radiative equilibrium, meaning the irradiances are balanced in each atmospheric layer.

- At the top of the atmosphere: $F_{TOA} = (1 - \varepsilon_{lw})F_g + F_a$
- At the atmosphere: $2F_a = \varepsilon_{sw}F_{TOA} + \varepsilon_{lw}F_g$
- At the surface: $F_g = (1 - \varepsilon_{sw})F_{TOA} + F_a$

Combining the first and the third equations, we obtain:

$$F_g = F_{TOA}\frac{2 - \varepsilon_{sw}}{2 - \varepsilon_{lw}} \tag{1.5}$$

If $F_{TOA} = \dfrac{S_0(1-\alpha)}{4} = 238.2\ \mathrm{W\,m^{-2}}$, and if we consider absorptances/emittances values of $\varepsilon_{sw} = 0.1$ and $\varepsilon_{lw} = 0.8$, the irradiance at the Earth's surface will be $F_g = 377.2\ \mathrm{W\,m^{-2}}$ (Andrews, 2010). According to equation 1.4, the ground temperature will be $T_g \approx 286\ \mathrm{K} \approx 13\ ^\circ\mathrm{C}$, very close to the observed value of $288\ \mathrm{K} \approx 15\ ^\circ\mathrm{C}$ (Andrews, 2010). We can also estimate the temperature of the atmosphere from the energy balance equations above. The temperature of the atmosphere can also be estimated from these energy balance equations, giving $T_a \approx 245\ \mathrm{K}$ (Andrews, 2010).

In the case of a non-absorbing atmosphere, $\varepsilon_{sw} = \varepsilon_{lw} = 0$ and then $F_g = F_{TOA}$, and the surface temperature would be $T_g = 255\ \mathrm{K}$, as estimated in the earlier theoretical model.

These two simple models help to explain the difference between the 255 K estimated in the case of a non-absorbing atmosphere and the 288 K observed due to the presence of certain gases in the Earth's atmosphere. These gases absorb shortwave and longwave radiation and re-emit IR (longwave) radiation, producing an increase in surface and tropospheric temperatures. This is known as the **greenhouse effect**. As the absorptance/emittance coefficients indicate, the atmosphere easily transmits solar radiation while trapping most IR radiation. Gases that absorb and emit IR radiation but allow shortwave solar radiation to pass are known as **greenhouse gases**. However, this is a simplified model, as it ignores the longwave effects of clouds and non-radiative processes, which significantly contribute to the planetary energy balance (Andrews, 2010).

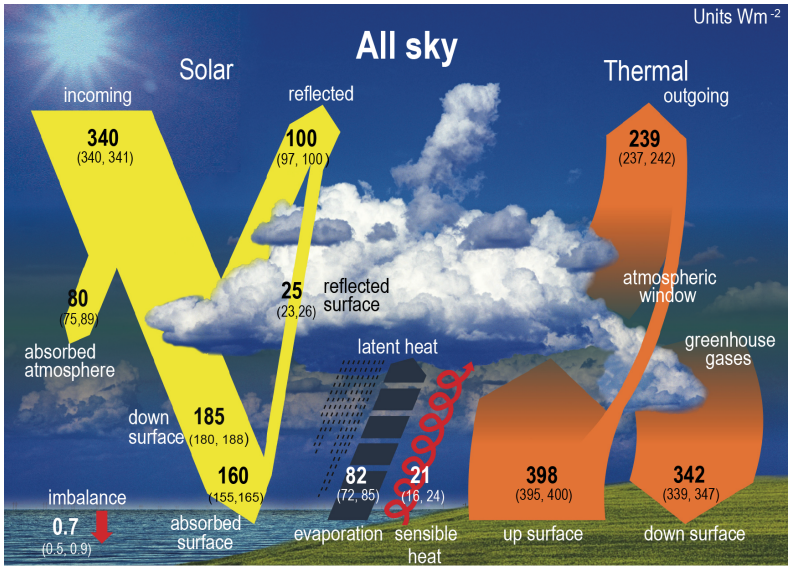

Figure 1.4. Representation of the global average Earth's energy budget at the beginning of the 21st century. The numbers show the best estimations of each of the components in $\mathrm{W\,m^{-2}}$ with the uncertainties within the parentheses. Adapted from Fig. 7.2 from IPCC (2021).

The left panel of Figure 1.5 shows the estimated global surface temperature change (grey line) over the last two millennia, and observed temperatures (black line) from 1850 to 2020. It can be observed that temperature fluctuated over time, reaching a maximum about 6500 years ago (shown by the grey vertical bar on the left side of the left panel - very likely range), during the Holocene (current interglacial period). This increase, shown by the grey vertical bar on the left, was caused by multi-millenial orbital variations, which cannot be compared to the rapid warming observed from 1900 to the present, as shown on the right panel. This current increase is explained by emissions produced by human activities, as shown by the brown line (Coupled Model Intercomparison Project Phase 6, CMIP6), in contrast to the green line, which shows the surface temperatures based only on natural factors (IPCC, 2021).

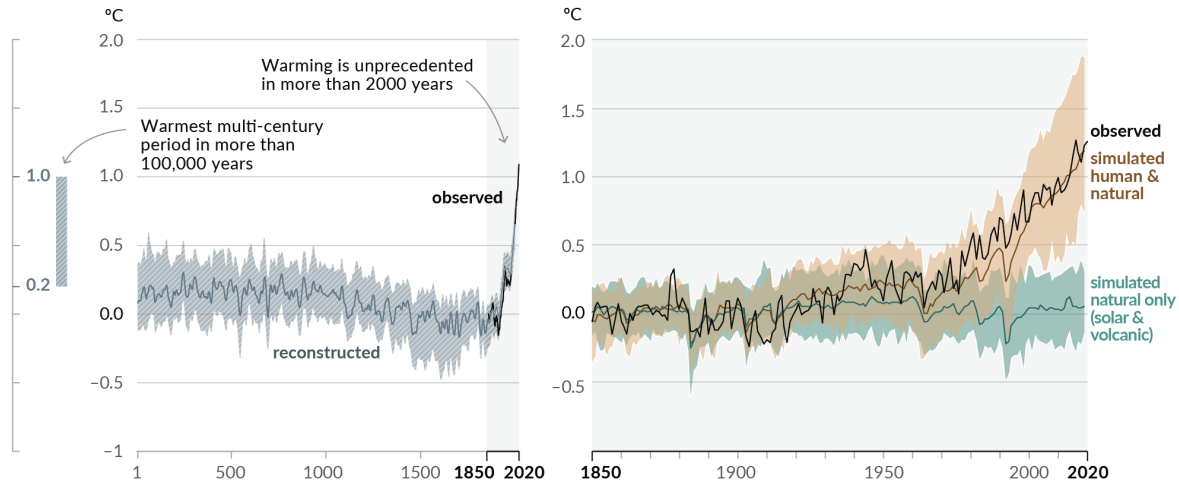

Figure 1.5. Changes in global surface temperature relative to 1850 – 1900. Left panel shows the surface temperature modeled from paleoclimate archives (grey line) and from observations between 1850 and 2020 (black line). The vertical grey line on the left side indicates the estimated temperature range for the warmest period in the last 100,000 years. Right panel shows annual temperature means observed between 1850 and 2020 (in black), as well as model simulations (CMIP6) temperature as a response to only natural (green line) and natural plus human (brown) contributions. In both panels, shadowed areas indicate the very likely ranges (90 – 100% likelihood) for the surface temperature modeling. Adapted from Fig. SPM.1 from WG1 IPCC (2021).

1.3.2 Greenhouse gases

As previously explained, greenhouse gases are responsible of the Earth's observed surface temperature. These gases are then essential for life on Earth as we know it. However, if the abundance of greenhouse gases increases, as has been the case since the Industrial Revolution, both atmospheric and surface temperatures rise, disrupting the biosphere and ecosystems.

The main anthropogenic greenhouse gases (GHGs) are carbon dioxide (CO_2), methane (CH_4), nitrous oxide (N_2O), the fluorinated gases, or F-gases (e.g. hydrofluorocarbons (HFCs), perfluorocarbons (PFCs), SF_6, and NF_3), halons, and chlorinated gases, such as CFCs, hydrochlorofluorocarbons (HCFCs), and CCl_4 (Table 1.1). However, the most abundant natural GHG is water vapour (H_2O). In 2019, CO_2 counted for 75% of the total anthropogenic GHG emissions, while F-gases represented only 2% (Figure 1.6). Nevertheless, the Global Warming Potentials (GWPs)[4] of F-gases are 10 to 150 times greater than those of the three most abundant anthropogenic GHGs (Table 1.1).

[4]The Global Warming Potential (GWP) determines the relative contribution of a species to climate warming. It is defined as "the ratio of the radiative forcing for a given mass emission of a substance relative to the same mass emission of CO_2 summed over a given time period (typically 20 or 100 years)" (WMO, 2022).

[5]The Ozone Depleting Potential (ODP) of a species determines its relative strength to destroy ozone. It is defined as "the ratio of the change in global ozone for a given mass emission of the substance to the change in global ozone for the same mass emission of CFC-11" (WMO, 2022).

Chemical or industrial name	Formula	Atmospheric abundance	Total lifetime (yr)*	Tropospheric lifetime (yr)	Stratospheric lifetime (yr)
Carbon dioxide	CO_2	417.9 ppm[a]			
Methane**	CH_4	1923 ppb[a]	11.8		
Nitrous oxide	N_2O	335.8 ppb[a]	109		
Chlorofluorocarbons					
CFC-12	CCl_2F_2	497.2 ppt[b]	102[c]	-	103
CFC-11	CCl_3F	224 ppt[b]	52[c]	-	55
CFC-113	CCl_2FCClF_2	68.9 ppt[b]	93[c]	-	94.5
CFC-114	$CClF_2CClF_2$	16.3 ppt[b]	189[c]	-	191
Hydrochlorofluorocarbons					
HCFC-22	$CHClF_2$	247.8 ppt[b]	11.6[c]	13	120
HCFC-141b	CH_3CCl_2F	24.5 ppt[b]	8.81[c]	10.7	49.4
HCFC-142b	CH_3CClF_2	21.7 ppt[b]	17.1[c]	19.3	148
Hydrofluorocarbons					
HFC-134a	CH_2FCF_3	113.0 ppt[b]	13.5[c]	14.1	313
HFC-23	CHF_3	33.7 ppt[b]	228[c]	243	3636
HFC-125	CHF_2CF_3	32.6 ppt[b]	30.7[c]	32.3	665
HFC-143a	CH_3CF_3	25.6 ppt[b]	51.8[c]	57.2	548
HFC-32	CH_2F_2	23.2 ppt[b]	5.27[c]	5.47	146
Chlorocarbons & Halons					
Carbon tetrachloride	CCl_4	77.6 ppt[b]	30[c]	-	44
Halon-1301	$CBrF_3$	3.32 ppt[b]	72[c]	2.10e+04	73.5
Fully fluorinated					
Nitrogen trifluoride[g]	NF_3	2.3 ppt[b]	569[c]	-	740
Sulfur hexafluoride[g]	SF_6	10.3 ppt[b]	850-1280[c]	-	-
PFC-14[g]	CF_4	86.4 ppt[b]	50,000[c]	-	50,000
PFC-116[g]	C_2F_6	4.94 ppt[b]	10,000[c]	-	10,000

ppm: parts-per-million (10^{-6}); ppb: parts-per-billion (10^{-9}), ppt: parts-per-trillion (10^{-12}).

* Atmospheric lifetime (or residence time) is the average time a substance remains in the atmosphere before being removed by natural processes such as chemical reactions, deposition, or transport to space.
Total lifetime (τ_{total}) is estimated from $\frac{1}{\tau_{\text{total}}} = \frac{1}{\tau_{\text{tropo}}} + \frac{1}{\tau_{\text{strato}}}$, where τ_{tropo} and τ_{strato} are the trospospheric and stratospheric lifetimes, respectively.

** Methane, non-fossil (fossil), is considered in the same row. Different values are indicated when necessary.

[a] Atmospheric abundances were taken from WMO GHG Bulletin for the year 2022.

[b] Atmospheric abundances were taken from Chapter 1 (for CFCs and HCFCs) and Chapter 2 (for HFCs) of WMO (2022) for the year 2020.

[c] Atmospheric lifetimes taken from the SPARC (2013) lifetime report.

[g] Not regulated by the Montreal Protocol but covered under the Kyoto Protocol (1997) and the Paris Agreement (2015).

Chemical or industrial name	Formula	ODP	GWP 20-yr	GWP 100-yr
Carbon dioxide	CO_2	0[d]	1	1
Methane**	CH_4	0[d]	79.7(82.5)	27(29.8)
Nitrous oxide	N_2O	0.017[e]	273	273
Chlorofluorocarbons				
CFC-12	CCl_2F_2	0.75[f]	12,700	12,500
CFC-11	CCl_3F	1[f]	8560	6410
CFC-113	CCl_2FCClF_2	0.82[f]	6870	6530
CFC-114	$CClF_2CClF_2$	0.53[f]	8280	9450
Hydrochlorofluorocarbons				
HCFC-22	$CHClF_2$	0.038[f]	5610	1910
HCFC-141b	CH_3CCl_2F	0.102[f]	2590	808
HCFC-142b	CH_3CClF_2	0.057[f]	5400	2190
Hydrofluorocarbons				
HFC-134a	CH_2FCF_3	0[d]	4060	1470
HFC-23	CHF_3	0[d]	12,400	14,700
HFC-125	CHF_2CF_3	0[d]	6790	3820
HFC-143a	CH_3CF_3	0[d]	7900	5900
HFC-32	CH_2F_2	0[d]	2620	749
Chlorocarbons & Halons				
Carbon tetrachloride	CCl_4	0.87[f]	3870	2150
Halon-1301	$CBrF_3$	17[f]	8580	7430
Fully fluorinated				
Nitrogen trifluoride[g]	NF_3	0[d]	13,600	17,700
Sulfur hexafluoride[g]	SF_6	0[d]	18,400	24,700
PFC-14[g]	CF_4	0[d]	5380	7490
PFC-116[g]	C_2F_6	0[d]	9040	12,600

** Methane, non-fossil (fossil), is considered in the same row. Different values are indicated when necessary.

[d] ODPs are considered negligible.

[e] ODP value was taken from Ravishankara et al. (2009).

[f] ODP values were taken from Chapter 7 of WMO (2022).

[g] Not regulated by the Montreal Protocol but covered under the Kyoto Protocol (1997) and the Paris Agreement (2015).

Table 1.1. Atmospheric abundances, lifetimes, Ozone Depleting Potentials (ODPs)[5], and Global Warming Potentials (GWPs) for 20- and 100-year time horizons of the three main anthropogenic greenhouse gases and the major CFCs, HCFCs, and HFCs. Some other important species are also included for comparison (Annex of WMO, 2022).

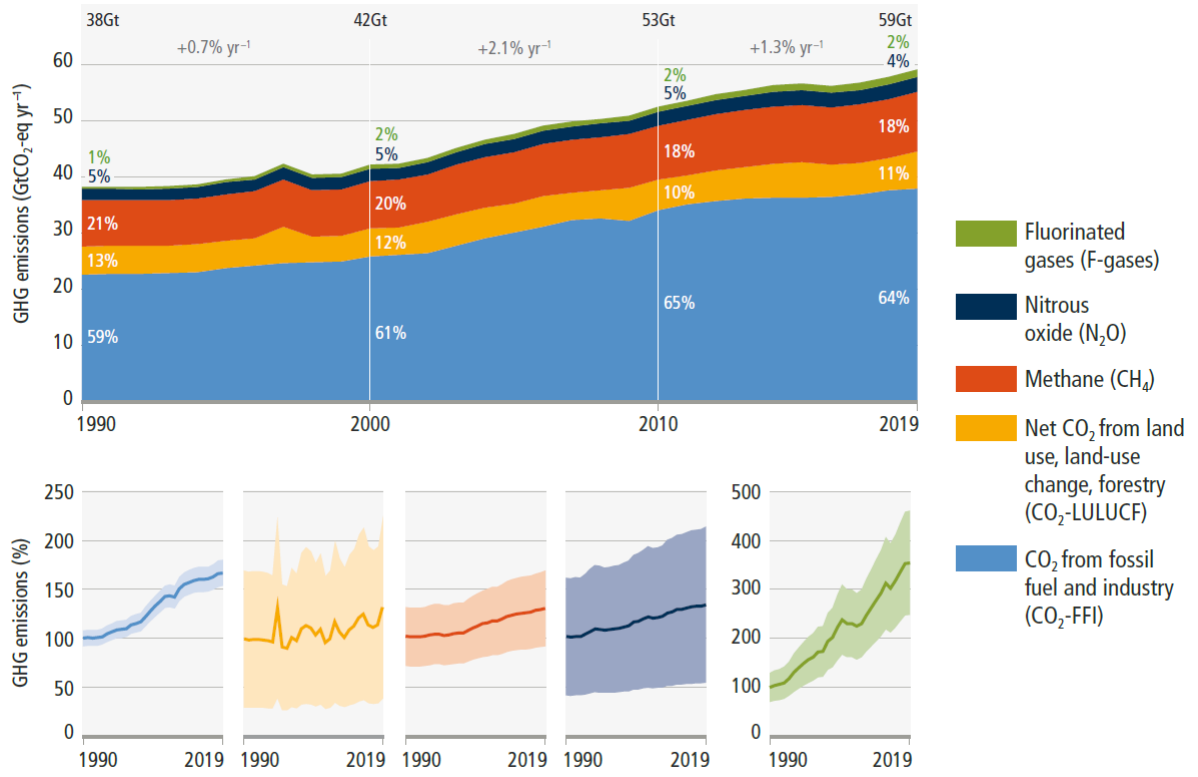

Figure 1.6. Global anthropogenic greenhouse gases emissions between 1990 and 2019 in gigatonnes of CO_2-equivalent per year ($Gt\,CO_2\text{-eq}\,yr^{-1}$) (top panel) and in % relative to 1990 (bottom panel). Colours show the contributions of the different greenhouse gases: in green, the fluorinated gases (HFCs, PFCs, SF_6, and NF_3); in navy blue, N_2O; in dark orange, CH_4; in dark yellow, CO_2 from land use, land-use changes, and forestry; and in blue, CO_2 from fossil fuel and industry. These emissions have been calculated based on GWPs with a 100-year time horizon. Percentages on the top panel show the fraction of global emissions for the different gases each decade. Growth rates between these periods are indicated above in $\%\,yr^{-1}$. Adapted from Fig. TS.2 from IPCC (2022).

Greenhouse gases are defined as atmospheric gases that absorb and emit infrared radiation while being transparent to solar radiation. But how do they interact with radiation?

When discussing atmospheric radiation, **dipoles** must be analysed. Dipoles consist of opposite charges separated by a small distance. Molecules with a permanent electric dipole, called **polar molecules**, such as H_2O, play an essential role in atmospheric radiation. Moreover, some non-polar molecules, such as CO_2, are also important in atmospheric radiation because electromagnetic radiation can excite the molecule and induce a temporary dipole moment. When electromagnetic radiation reaches gas molecules, it produces accelerated electric dipoles within the molecules, which will radiate in all directions. After this interaction, several processes can occur (Bohren and Clothiaux, 2006):

- Electromagnetic waves pass beyond the molecules, and the induced accelerated dipoles stop. Then the molecules' internal energy remains unchanged. This phenomenon is called **scattering**.

- Solar electromagnetic radiation can also change the internal energies of some molecules. If the molecule has more internal energy after the interaction with the electromagnetic

wave, we say that the molecule has **absorbed** this energy from the incident wave.

- On the contrary, if the molecule loses internal energy and transfers it to the incident electromagnetic wave, the process is called **induced emission**.
- Molecules with a permanent electric dipole can also emit energy without any external electromagnetic wave involvement, as their dipoles accelerate through spinning. This phenomenon is known as **spontaneous emission**.

1.3.2.1 Absorption and emission by atmospheric molecules

The internal energy of a molecule is quantised into rotational, vibrational, and electronic states, and it can be modified by the electromagnetic radiation absorbed and/or emitted by the molecule. This process happens at specific energy levels. To produce the transition from the ground state to an excited state, different transitions require different energy levels: **rotational transitions** require low energy (long wavelengths, such as far-infrared radiation, $\lambda > 15$ μm), while **electronic transitions** require high-energy wavelengths, such as UV radiation ($\lambda < 400$ nm). **Vibrational transitions** typically occur in the near-infrared range (0.7 μm $< \lambda < 1.4$ μm) (Bohren and Clothiaux, 2006).

When an electromagnetic wave interacts with a polar molecule, such as H_2O or O_3 (Figure 1.7), it can exert forces on the molecule and produce a torque on the molecule, altering its rotation speed. The incident wave can also cause asymmetric compressing, stretching, or twisting of the molecule's atoms, increasing or decreasing the vibrational energy of the molecule. Moreover, if the electromagnetic wave is energetic enough, it can lead electrons to higher or lower electronic states. Consequently, the process of **absorption** occurs if the internal energy of a molecule rises by the increase of the rotational energy of the molecule, via the torque produced on permanent dipoles by the incident wave, or the increase of its vibrational energy due to the differential forces exerted on the atoms, or if the electrons travel to higher excited electronic states. Conversely, when a molecule slows its rotation or vibration, or its electrons return to lower electronic states after interacting with an electromagnetic wave, the internal energy of the molecule decreases as it transfers some energy to the electromagnetic wave. This process is known as **induced emission**. Additionally, polar molecules that rotate or vibrate will naturally emit radiation, a process known as **spontaneous emission** (Bohren and Clothiaux, 2006).

Polar molecules, such as H_2O and O_3, have a net dipole moment produced by the addition of the two independent sub-dipoles[6] in the O-H and O-O bonds, respectively, as shown by the dark blue arrow in Figure 1.7. Non-polar molecules, such as CO_2 and CH_4, do not have permanent dipoles due to their symmetrical shapes (linear and tetrahedral geometries, respectively), but they can still vibrate or stretch asymmetrically and emit radiation when interacting with electromagnetic waves. For example, CO_2 which is symmetric and non-polar in its ground state, it can have a temporary dipole moment change when one oxygen moves in, while the other moves out due to an incident electromagnetic wave. The same effect is observed when oxygen atoms move in opposite directions perpendicular to the bond axis (Bohren and Clothiaux, 2006).

[6]The direction and the sense of the sub-dipoles (atom-atom bonds) are determined by the electronegativities of the different atoms that compose each molecule. Electronegativities (Pauling scale): $\chi_H = 2.20$; $\chi_C = 2.55$; $\chi_{Cl} = 3.16$; $\chi_O = 3.44$; $\chi_F = 3.98$

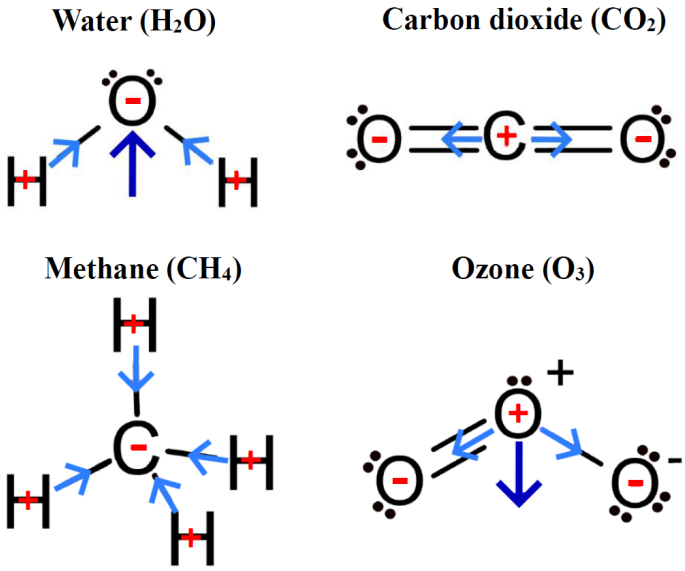

Figure 1.7. Schematic representation of the molecular structures of water, carbon dioxide, methane and ozone. Net positive (+) and negative (-) charges are illustrated in red for each molecule. The net electric dipoles created by these charges separations are represented by the dark blue arrows (in the case of polar molecules), and the sub-dipoles inside the molecules are shown by the light blue arrows.

For a gas to be considered a greenhouse gas, it must absorb and re-emit infrared radiation, based on dipole moment changes. This depends on how its dipole moment changes during vibrations. One might think that the name of "greenhouse gases" is somewhat misleading, as a greenhouse traps energy and blocks warm air from escaping, while these gases behave more like "radiators". Thus, it would be more accurate to refer to them as **infrared radiatively active gases**, since they emit more energy as temperatures rise (Bohren and Clothiaux, 2006). The recent increase of their atmospheric concentrations, driven by human activity, enhances the amount of IR radiation emitted by Earth's surface that is subsequently absorbed by these gases. As a result, their temperature increases, leading to increased emission of longwave radiation from the atmosphere back to the surface, warming both the atmosphere and the surface (Bohren and Clothiaux, 2006).

1.3.2.2 The case of CFC-11 and HFC-134a

The molecules studied in Chapters 3 and 4 are trichlorofluoromethane (CCl_3F), also known as CFC-11; and 1,1,1,2-tetrafluoroethane (CH_2FCF_3), also known as HFC-134a, respectively. As shown in Figure 1.8, these molecules have net dipole moments, so they are polar molecules.

CFC-11 consists of a central carbon atom, surrounded by one fluorine atom and three chlorine atoms, forming a tetrahedral structure. Due to the higher electronegativity of fluorine (3.98) compared to carbon (2.55), the C-F bond has a dipole moment pointing toward the fluorine atom. Similarly, because chlorine is more electronegative (3.16) than carbon, the C-Cl bonds have dipole moments pointing toward the chlorine atoms. The overall dipole moment of CFC-11 is dominated by the C-F bond, pointing toward the fluorine atom, as shown by the dark blue arrow in Figure 1.8 (left panel).

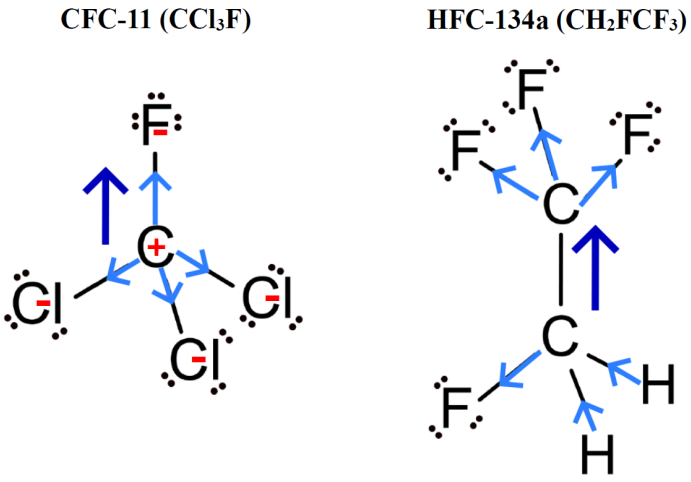

Figure 1.8. Schematic representation of the molecular structures of CFC-11 and HFC-134a. Net positive (+) and negative (-) charges are illustrated in red for CFC-11, but not for HFC-134a to avoid the overloading of the scheme. The net electric dipoles created by these charges separations are represented by the dark blue arrows, and the sub-dipoles inside the molecules are shown by the light blue arrows.

HFC-134a consists of two carbon atoms, each bonded to fluorine and/or hydrogen atoms. The first carbon atom (C_1) is bonded to three fluorine atoms, forming a symmetrical tetrahedral structure, while the second carbon atom (C_2) is bonded to two hydrogen atoms and one fluorine atom, also forming a tetrahedral structure. The two carbon atoms form a single bond and the whole molecule can be seen as a double tetrahedral structure (Figure 1.8, right panel). Because fluorine is more electronegative than carbon, the dipole moments of the C-F bonds point toward the fluorine atoms. The C-H bonds have smaller dipole moments pointing toward the carbon atom. The overall dipole moment of HFC-134a points from the region near the hydrogen atoms (C_2) toward the region near the fluorine atoms (C_1), as indicated by the dark blue arrow in Figure 1.8. The net charges of HFC-134a are not shown in the Figure to avoid the overloading of the scheme, because C_2 will create different poles depending on the different bonds (negative in the C_2-H bonds and positive in the C_2-F bond).

Both CFC-11 and HFC-134a have **permanent electric dipoles** that interact with electromagnetic waves, leading to rotational-vibrational transitions and emission of IR radiation, as explained earlier. Consequently, they are also considered greenhouse gases as they absorb and emit longwave radiation.

1.3.2.3 Absorption spectra of atmospheric gases

The Sun emits radiation in a manner approximating that of a black body. Figure 1.9 illustrates the differences between the spectral irradiance of a black body at T = 6000 K, representative of the photosphere's temperature, the spectral irradiace measured at the top of the atmosphere, and at sea level. At the TOA, solar irradiance closely resembles that of a black body, whereas significant deviations are observed in the spectral irradiance measured at sea level. These deviations are due to atmospheric gases that absorb and scatter solar radiation at various wavelengths, such as O_3 in UV and visible ranges, and CO_2 and H_2O in the IR range (Andrews, 2010).

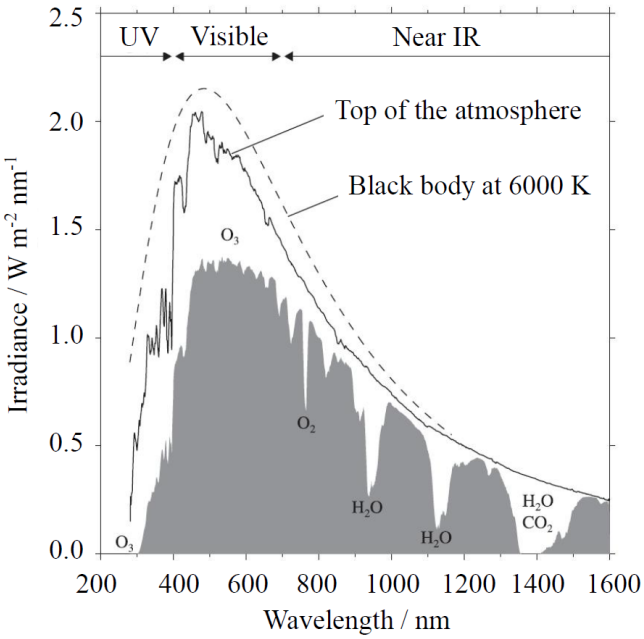

Figure 1.9. Irradiance spectra of solar radiation of a black body at 6000 K (dashed line), at the top of the atmosphere (solid line), and at sea level (shaded). Adapted from Fig. 3.13 from Andrews (2010).

Absorption cross sections quantify molecular absorption and vary between molecules due to differences in their internal structures. Absorption depends on the wavelength (or frequency) of the incident radiation and is measured in units of area. When the frequency of the incident electromagnetic wave matches the energy levels associated with a molecule's internal transitions (according to the equation $E = h\nu$)[7], significant absorption occurs, causing the cross section to increase. Conversely, when frequencies differ from the internal energy transitions, absorption is minimal and cross sections are close to zero. The **absorption spectrum** of a gas consists of lines representing the transitions between energy states of its molecules.

Absorption lines in rotational-vibrational spectra are not true "lines"; instead, they have a broader shape, as shown in Figure 1.10. Various factors, including velocity components and molecular interactions, contribute to **line broadening**. When molecules are sufficiently far apart and do not interact, they remain at the same excited energy level. However, the frequencies of electromagnetic radiation emitted by each molecule can vary slightly, resulting in a broadening of the absorption line. This type of broadening, known as natural broadening, is the least significant in the lower atmosphere. A more pronounced broadening effect, Doppler broadening, occurs because molecules in a gas move randomly with a velocity distribution that increases with temperature. Lastly, collisional broadening arises from intermolecular forces that alter molecular energy states. Frequent collisions in the troposphere perturb multiple molecules simultaneously, thus broadening the range of absorption and emission frequencies. As pressure and/or temperature increase, the collision rate rises, making collisional broadening more significant. This type of broadening has the greatest impact on the absorption and emission lines within Earth's troposphere (Bohren and Clothiaux, 2006).

The transmittance of a medium is defined as the fraction of electromagnetic radiation that

[7] h is Planck's constant ($h = 6.63 \times 10^{-34}$ J · s) and ν is the frequency of the electromagnetic wave.

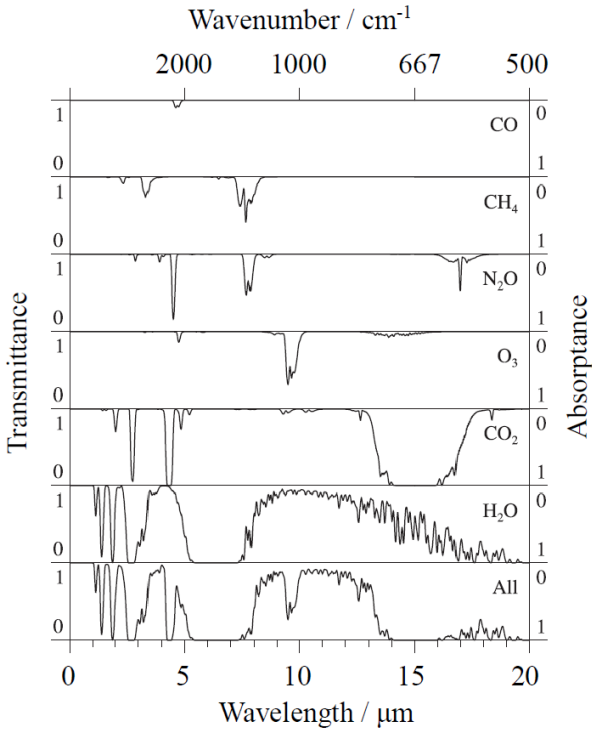

Figure 1.10. Infrared absorption spectra for carbon monoxide, methane, nitrous oxide, ozone, carbon dioxide, water vapour, and for the six gases combined, for a vertical beam crossing the atmosphere, in clear-sky conditions. Adapted from Fig. 3.14 from Andrews (2010).

is neither absorbed nor scattered and can therefore propagate through the medium at a specific wavelength. From 1 μm to 10 μm (10000 – 1000 cm^{-1}), drops in transmittance are due to absorption from vibrational-rotational transitions of the main greenhouse gases. In the 8 – 14 μm (1250 – 700 cm^{-1}) range, transmittance is very high because absorption by atmospheric gases is minimal in this region, a phenomenon known as the **atmospheric window**. Between 14 and 18 μm (700 – 555 cm^{-1}), transmittance decreases due to absorption by CO_2, and remains close to zero up to 1 mm because of absorption by H_2O (Figure 1.10; Bohren and Clothiaux, 2006).

1.3.3 Stratospheric ozone

In the Earth's atmosphere, ozone is found in two main layers: the troposphere and the stratosphere. Tropospheric ozone is produced when nitrogen oxides (NO_x)[8] and volatile organic compounds (VOCs)[9] react in the presence of sunlight. Emissions of NO_x and VOCs come from both natural and anthropogenic sources. Natural sources of NO_x include lightnings, volcanoes, and soil bacteria; while plants, trees, and wildfires emit VOCs. Anthropogenic emissions (NO_x and VOCs) come mainly from fuel combustion and industrial processes. Tropospheric ozone is a significant pollutant and greenhouse gas that contributes to smog formation and causes respiratory issues (UCAR, 2024).

[8] NO_x are a group of gases that include nitrogen monoxide (NO) and nitrogen dioxide (NO_2).
[9] VOCs are carbon-based chemicals that easily evaporate into the air.

Stratospheric ozone is produced naturally and is also known as the **ozone layer**. This is a crucial region of our atmosphere, as it protects human health and ecosystems from harmful UV radiation. The presence of the ozone layer was first explained by Chapman (1930), and his model is named the **Chapman mechanism**.

Ozone molecules are produced in two steps. First, oxygen (O_2) molecules in the stratosphere are photodissociated by solar ultraviolet radiation ($\lambda < 242.4$ nm), forming two independent oxygen atoms (Brasseur and Solomon, 2005; Andrews, 2010):

$$O_2 + h\nu \longrightarrow O + O \tag{1.6}$$

where h is Planck's constant ($h = 6.63 \times 10^{-34}$ J · s), and ν is the frequency of the electromagnetic wave.

Next, these two oxygen atoms can recombine with the help of a third body M[10]:

$$O + O + M \longrightarrow O_2 + M \tag{1.7}$$

Nevertheless, this process takes place mainly in the thermosphere, where atomic oxygen is very abundant.

Otherwise, the atomic oxygen can recombine with molecular oxygen and another molecule M, which absorbs the excess of energy and stabilises the molecule of ozone:

$$O_2 + O + M \longrightarrow O_3 + M \tag{1.8}$$

Stratospheric ozone molecules are exclusively formed via this reaction.

Finally, the **destruction of ozone** can occur by recombination with atomic oxygen (1.9) or by its photodissociation (1.10) to form oxygen molecules:

$$O_3 + O \longrightarrow 2O_2 \tag{1.9}$$

$$O_3 + h\nu \longrightarrow O_2 + O \tag{1.10}$$

To sum up, the net ozone creation from molecular oxygen via (1.6) and (1.8) is:

$$3O_2 \longrightarrow 2O_3 \tag{1.11}$$

while its net destruction is described by reactions (1.9) and (1.10):

$$2O_3 \longrightarrow 3O_2 \tag{1.12}$$

It is important to note that Chapman's cycle is only effective during daytime due to photodissociation reactions. Only recombination reactions, depleting atomic oxygen, are active during nighttime.

[10]The molecule M acts as a catalyst in the reaction and is usually N_2 or O_2 since these are the two major atmospheric constituents.

1.3.3.1 Catalytic cycles of stratospheric ozone destruction

The actual concentration of ozone in the lower stratosphere is smaller than what the Chapman mechanism predicts. In order to understand this difference, the effects of catalytic cycles should be considered (Andrews, 2010):

$$O_3 + X \longrightarrow O_2 + XO \tag{1.13}$$

$$XO + O \longrightarrow O_2 + X \tag{1.14}$$

where X is a catalyst molecule such as the hydroxyl radical (OH), nitric oxide (NO), chlorine (Cl), or bromine (Br), which contribute to ozone destruction through the HO_x, NO_x, ClO_x, and BrO_x catalytic cycles, respectively.

The net effect is:

$$O + O_3 \longrightarrow 2O_2 \tag{1.15}$$

Since the catalyst is not consumed in the reaction, a single molecule can break up many ozone molecules, leading to considerable effects. Ozone-depleting substances (ODSs) are responsible of the currently observed stratospheric ozone loss (see Sections 1.3.3.2 and 1.4).

1.3.3.2 Antarctic stratospheric ozone

Atmospheric ozone observations are conducted from various platforms, including satellites, sounding balloons, and aircrafts, or from the ground. Consequently, global ozone depletion, especially over Antarctica in spring, is well-documented, with high atmospheric concentrations of chlorine and bromine identified as primary drivers. The presence of ODSs in the atmosphere and their continuous increase until the mid-1990s led to a significant reduction in ozone, particularly in polar regions (WMO, 2022).

In response to the Montreal Protocol on Substances That Deplete the Ozone Layer (1987), the atmospheric concentrations of ODSs, and therefore organic and inorganic chlorine and bromine, have been declining since the 1990s, leading to improvements in ozone recovery in the upper stratosphere. Despite interannual variability, total column ozone (TCO) is gradually recovering over the Antarctic region, although this recovery is less consistent outside this region (from 90°N to 60°S). Models estimate that TCO will return to 1980 levels around 2040 outside polar regions (60°N – 60°S), by approximately 2045 over the Arctic, and around 2066 over the Antarctic (Figure 1.11; WMO, 2022).

However, these substances are not the only contributors to the variations of stratospheric ozone column. Model simulations suggest that increasing atmospheric CO_2 concentrations cool the stratosphere, leading to changes in stratospheric circulation and potentially increasing global ozone levels. Moreover, rising atmospheric CH_4 concentrations contribute to increases in total column ozone because CH_4 acts as a tropospheric ozone precursor and reacts with chlorine in the stratosphere, reducing ozone depletion. Another important species is N_2O. When it reaches the stratosphere, it undergoes photodissociation. Consequently, N_2O serves as a significant source of NO_x, contributing to stratospheric ozone loss, similarly to ODSs. Therefore,

while global stratospheric ozone is expected to increase as ODSs concentrations decline, future ozone levels will also depend on greenhouse gases concentrations (WMO, 2022).

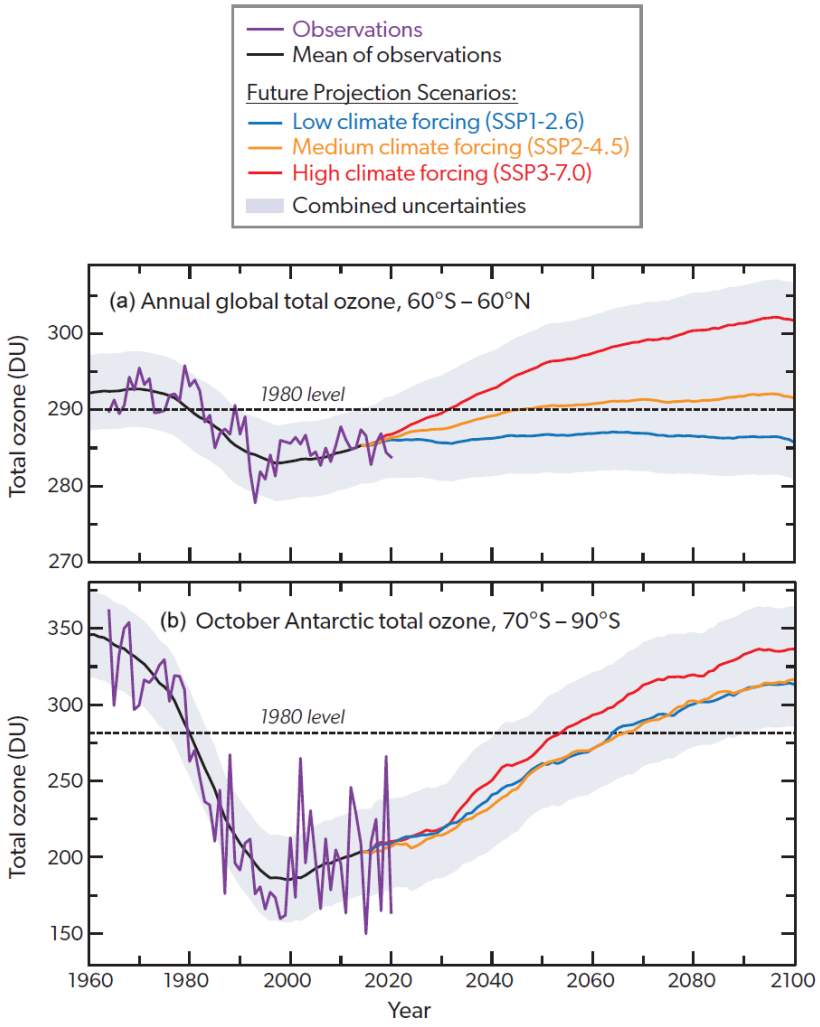

Figure 1.11. Annual average global total column ozone (TCO) at non-polar latitudes (Panel (a)), and October average Antarctic total ozone (Panel (b)). Observations are shown in purple. Chemistry-climate model projections assume fulfilment of the Montreal Protocol and a rise of greenhouse gases according to the different shared socioeconomic pathways (SSPs): in blue, a low climate forcing scenario (SSP1-2.6); in yellow, a medium climate forcing scenario (SSP2-4.5); and in red, a high climate forcing scenario (SSP3-7.0). Grey shading shows the combined uncertainty (1-sigma standard deviation) of the multi-model mean. TCO is expressed in Dobson Units (DU). One DU is equal to 2.6867×10^{20} molec. m^{-2} or 4.4615×10^{-4} mol m^{-2}. Adapted from Fig. ES-1 from WMO (2022).

Why does the main decline occur over the Antarctic?

During winter, stratospheric temperatures drop below approximately 190 K (≈ -80 °C), especially within the polar vortex. These conditions allow polar stratospheric clouds (PSC) to form. These clouds provide surfaces for chemical reactions that convert stable chlorine reservoirs in the stratosphere, such as hydrogen chloride (HCl) and chlorine nitrate ($ClONO_2$), into reactive chlorine. This chlorine activation leads to significant ozone depletion at high latitudes when sunlight returns at the end of winter and beginning of spring (around September and October in Antarctica; Figure 1.12). The stability of the polar vortex isolates polar air masses

from the surrounding atmosphere, resulting in substantial ozone depletion and the formation of the so-called "ozone hole"[11]. Similar reactions occur with active bromine.

While this process is not unique to Antarctica and can occur over the Arctic during extremely cold winters, the Arctic polar vortex is typically weaker, resulting in less severe ozone depletion than in Antarctica (Figure 1.12). Additionally, events like large volcanic eruptions (e.g., Mount Pinatubo in 1991) can further trigger chlorine activation and ozone destruction by releasing sulfate aerosols into the stratosphere, which provide surfaces for these chemical reactions (Brasseur and Solomon, 2005).

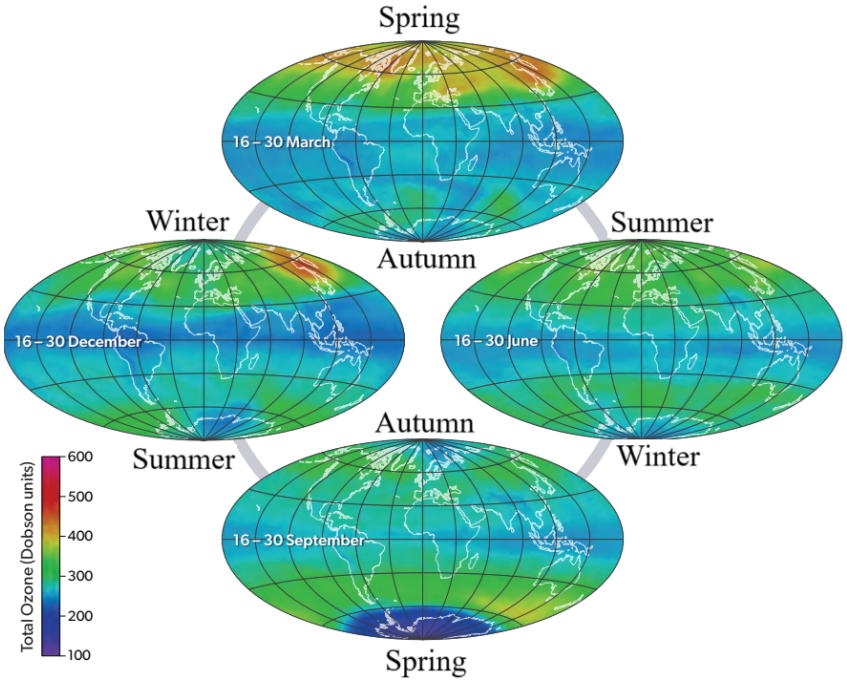

Figure 1.12. Global satellite maps of total ozone in 2021. Total ozone depends on location (latitude, longitude) and time (season). The largest values are found at high northern latitudes, while the lowest values are observed in tropical regions. A severe depletion can be observed in spring over the Antarctic, due to the intense polar vortex, the formation of polar stratospheric clouds, and the resulting release of reactive chlorine and bromine atoms. The colour bar on the left indicates the total ozone concentrations in Dobson Units. Adapted from Fig. Q3-1 from Salawitch et al. (2022).

1.4 Halogenated compounds in the Earth's atmosphere

In 1995, the Nobel Prize in Chemistry was jointly awarded to Paul Crutzen, Mario Molina, and Sherwood Rowland for their research on human impacts on the Earth's atmosphere, conducted during the 1970s. In 1970, P. Crutzen demonstrated that nitrogen oxides (NO_x) accelerate ozone depletion (Crutzen, 1970). In 1974, M. Molina and S. Rowland identified CFCs as a significant threat to the stratospheric ozone (Molina and Rowland, 1974). These studies allowed the understanding of the unexpected discovery of the ozone hole over Antarctica in

[11]The term "ozone hole" should be used cautiously, as it does not refer to an actual hole with no ozone, but rather to a significant thinning of the ozone layer, when the TCO drops below 220 DU.

1985 by Joseph C. Farman, Brian G. Gardiner, and Jonathan D. Shanklin (Farman et al., 1985). Precisely, the scientific community concluded that this depletion was caused by reactions of ozone with chlorine and bromine from industrially produced gases. These ground-breaking discoveries drove to the development of the Montreal Protocol on Substances That Deplete the Ozone Layer in 1987, an international treaty designed to protect the ozone layer by reducing the use and production of industrial chemicals responsible for stratospheric ozone depletion.

1.4.1 The role of halogens in ozone depletion

Halogens (fluorine, chlorine, bromine, and iodine) are present in the atmosphere due to both natural and anthropogenic processes. When halocarbons (organic compounds containing halogens) are released at the Earth's surface, they gradually ascend into the stratosphere, where they are photodissociated. This process liberates reactive halogen atoms. Since chlorine and bromine are the most reactive halogens, ozone-depleting substances are defined as gases bearing chlorine and/or bromine that are released into the atmosphere due to natural and anthropogenic emissions. These gases include CFCs, carbon tetrachloride (CCl_4), methyl chloroform (CH_3CCl_3), methyl bromide (CH_3Br), halons, and HCFCs, among others (see Table 1.1; WMO, 2022). Natural sources of halogens include volcanic eruptions, marine aerosols, and biomass burning (Figure 1.13). However, the primary contribution of halogens to ozone depletion comes from anthropogenic emissions such as refrigeration systems, solvents, fire extinguishers, insulation, etc. (Figure 1.14).

- **Fluorine** rapidly forms carbonyl fluoride (COF_2) and hydrofluoric acid (HF), which are very stable reservoirs. This process neutralises most of the fluorine released into the stratosphere. Another temporary fluorine and chlorine reservoir is carbonyl chlorofluoride (COClF), which is not highly reactive toward ozone. Consequently, the amount of atomic fluorine (F) and fluorine oxide (FO) available for ozone depletion is minimal and fluorine has an insignificant impact on ozone destruction (Brasseur and Solomon, 2005). However, fluorinated halocarbons, along with other gases like PFCs, nitrogen trifluoride (NF_3), and sulfur hexafluoride (SF_6), are highly potent greenhouse gases (see Table 1.1).

- **Chlorine** atoms are released into the stratosphere through the photolysis of anthropogenic ozone-depleting substances. Inorganic chlorine reservoirs, such as hydrogen chloride (HCl) and chlorine nitrate ($ClONO_2$), form through reactions with other atmospheric species. These reservoirs temporarily sequester chlorine, preventing immediate ozone destruction. However, under certain conditions, these reservoirs can be broken down, releasing active chlorine species that contribute to stratospheric ozone depletion. Chlorine from natural sources, such as sea salt and volcanic emissions, is typically removed from the atmosphere via precipitation due to its high solubility. In contrast, many anthropogenic halogenated molecules, such as CFCs, are highly stable and insoluble in water, making removal through precipitation nearly impossible (Brasseur and Solomon, 2005). Moreover, due to their long atmospheric lifetimes (Table 1.1), these compounds are transported to the stratosphere, where they undergo photodissociation.

- **Bromine** is less tightly bound in atmospheric compounds than chlorine, making it more easily freed from bromocarbons. Atmospheric bromine reservoirs, such as hydrobromic

acid (HBr) and bromine nitrate ($BrONO_2$), are less stable than chlorine reservoirs and can be easily converted back into reactive bromine. Despite being present in much lower concentrations than chlorine (Figure 1.14), the bromine atom is much more effective (approximately 50 times) at destroying stratospheric ozone due to its lack of stable stratospheric reservoirs (Brasseur and Solomon, 2005). However, the atmospheric abundances of anthropogenic bromocarbons remain significantly lower than those of chlorocarbons, CFCs, and HCFCs (Figure 1.14; WMO, 2022).

- **Iodine** can also contribute to stratospheric ozone-depleting catalytic cycles, but the atmospheric concentrations of iodocarbons are negligible compared to bromine and chlorine compounds. Methyl iodide (CH_3I) is the primary organic iodine-containing source gas, with a mean atmospheric abundance is 0.8 ppt. It is considered a Very Short-Lived Substance (VSLS) due to its total atmospheric lifetime of less than 14 days. This compound primarily originates from natural sources, such as oceanic environments, and there is currently no observed trend indicating significant changes in its concentration. Unlike chlorine and bromine, iodine does not significantly contribute to stratospheric ozone depletion because it is rapidly removed before reaching the ozone layer (WMO, 2022).

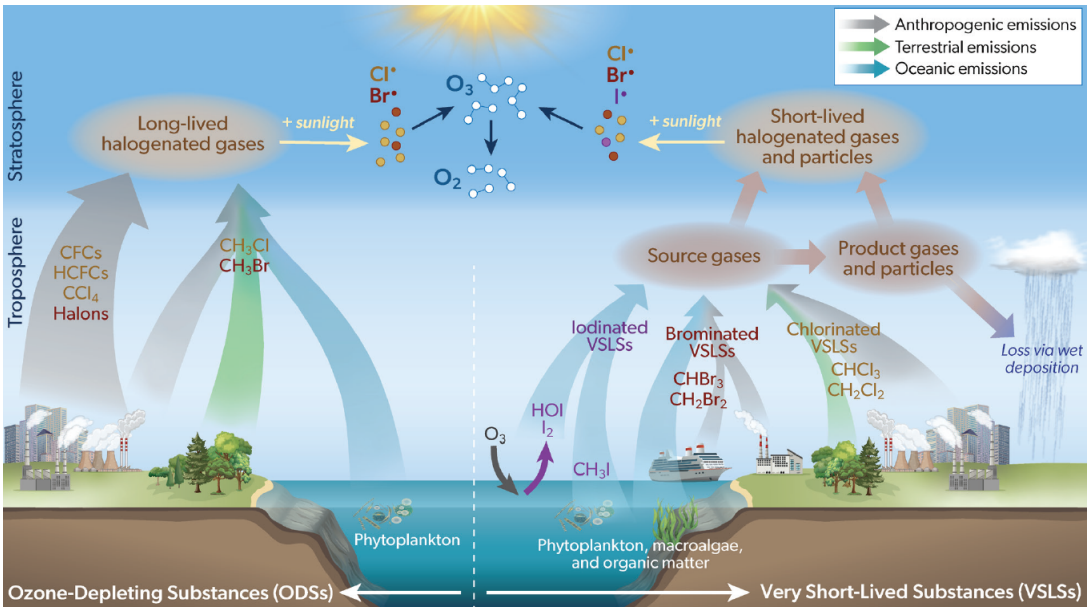

Figure 1.13. Anthropogenic (grey arrows), terrestrial (green arrows), and oceanic (blue arrows) emissions of long-lived halogenated gases and short-lived halogenated substances. Even if bromine is more effective in stratospheric ozone destruction than chlorine, atmospheric abundances of bromine-containing compounds are much smaller than chlorine-containing compounds. Fig. 1 (Box 1-3) from WMO (2022).

Ozone depletion is therefore primarily driven by anthropogenic emissions of ODSs, which travel upward to the stratosphere and release reactive halogens, specifically chlorine and bromine. In addition to long-lived ODSs, such as CFCs, another group of halogen-containing substances, known as Very Short-Lived Substances, exist. These compounds have atmospheric lifetimes shorter than six months and are mostly destroyed in the troposphere. Since only small fractions of these VSLSs reach the stratosphere, they are not important contributors to ozone loss and are not regulated by the Montreal Protocol.

Thanks to the regulations of the Montreal Protocol, the amount of chlorine getting into the stratosphere from ozone-depleting substances decreased by 11.5% between its maximum in 1993 and 2020. Similarly, bromine input to the stratosphere declined by 14.5% between their peak in 1999 and 2020 (Figure 1.14).

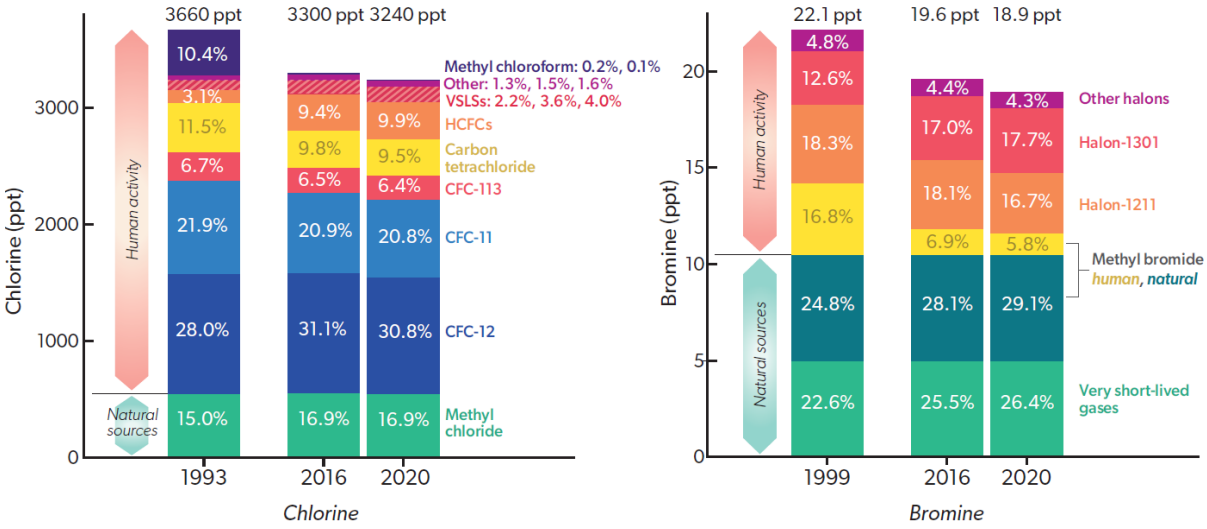

Figure 1.14. Total chlorine (left) and bromine (right) entering the stratosphere for a reference year, corresponding to the maximum of the tropospheric loadings (1993 for chlorine and 1999 for bromine). Mole fractions were estimated from surface measurements (NOAA and AGAGE), as well as model simulations when observations were not available. Fig. 1-15 from WMO (2022).

1.4.2 CFCs, HCFCs, and HFCs

In response to the Montreal Protocol and its subsequent amendments, CFCs, methyl chloroform (CH_3CCl_3), CCl_4, and the halons have been gradually phased out and progressively replaced by HCFCs and HFCs. Consequently, atmospheric concentrations of CFCs are decreasing, while concentrations of HCFCs are plateauing, and concentrations of HFCs are rising rapidly, as shown in Figures 1.15 and 1.16, respectively (WMO, 2022).

CFCs, HCFCs, and HFCs are synthetic compounds produced by industry, primarily for use as refrigerants, propellants, and solvents. While natural chlorine in the stratosphere comes from the photolysis of chloromethane (CH_3Cl)[12], anthropogenic chlorine arises from the photodissociation of chlorocarbons, such as CFCs. CFCs are highly stable molecules capable of reaching the stratosphere, where they are photodissociated and liberate chlorine atoms that ultimately destroy ozone. For instance, CFC-11 (CCl_3F) undergoes a series of reactions that release three chlorine atoms, which are then subject to react with ozone (Brasseur and Solomon, 2005), as described in Section 1.3.3.1:

$$CCl_3F + h\nu \longrightarrow CCl_2F + Cl \quad (\lambda < 226\,nm) \tag{1.16}$$

[12]The majority of CH_3Cl is broken down in the troposphere by the OH radical. However, a small fraction that survives this process can reach the stratosphere, where it undergoes photolysis, releasing chlorine atoms that contribute to ozone depletion.

$$CCl_2F + O_2 + M \longrightarrow CCl_2FO_2 + M \tag{1.17}$$

$$CCl_2FO_2 + NO \longrightarrow CCl_2FO + NO_2 \tag{1.18}$$

$$CCl_2FO + M \longrightarrow CClFO + Cl + M \tag{1.19}$$

$$CClFO + h\nu \longrightarrow FCO + Cl \tag{1.20}$$

At the beginning of the 1990s, total global CFC emissions were approximately 1000 Gg yr^{-1} (WMO, 2022). By the mid-1990s, around 75 – 85% of chlorine in the stratosphere was of anthropogenic origin (Zander et al., 1996). Most developed countries completely stopped production and use of CFCs by 1996. Developing countries were given more time but fully phased out CFCs by 2010. Consequently, atmospheric levels are decreasing (Figure 1.15, left column). In 2020, stratospheric chlorine was reduced by 11.5% relative to 1993 levels (left panel of Figure 1.14) and global CFCs emissions are estimated to be approximately 85 Gg yr^{-1}, that is 730 teragrams of CO_2-equivalent per year (Tg CO_2-eq yr^{-1}) (WMO, 2022). However, these gases persist in old equipment, and new unreported emissions (e. g., of CFC-11) have been detected (Montzka et al., 2018; Chipperfield et al., 2021).

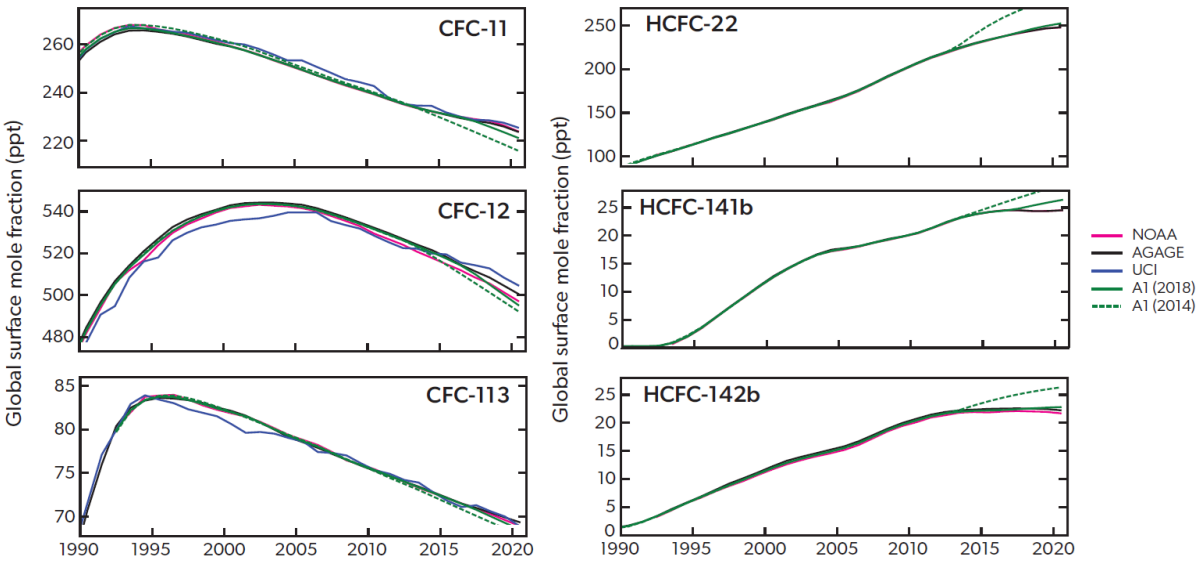

Figure 1.15. Global annual mean mole fractions between 1990 and 2020 of the most abundant CFCs (left column) and HCFCs (right column) from ground-based measurement networks (NOAA, AGAGE, and UCI) and from simulations (A1 scenarios; Harris et al., 2014; WMO, 2018). Adapted from Fig. 1-1 from WMO (2022).

HCFCs were introduced as a temporary replacement for CFCs, leading to a rapid increase in their global concentrations (Figure 1.15, right column). While HCFCs also contain chlorine and can contribute to stratospheric ozone depletion, they have carbon-hydrogen bonds that allow them to be destroyed by the hydroxyl radical in the troposphere. This oxidation in the lower atmosphere allows the oxidation products to recombine with other chemicals and form compounds that can be dissolved and removed by precipitation, shortening their atmospheric lifetimes relative to CFCs. Consequently, a significant fraction of HCFCs does not enter in the stratosphere. However, another part can reach the stratosphere and be photodissociated, liberating chlorine atoms. HCFCs release proportionally fewer chlorine atoms than CFCs and therefore contribute less to ozone depletion (see Table 1.1; Brasseur and Solomon, 2005). In 2020,

global HCFCs emissions were estimated to be approximately 420 Gg yr^{-1}, that is 750 Tg CO_2-eq yr^{-1} (WMO, 2022). Their production has been banned since 2020 in developed countries, with a phased ban in developing countries by 2030.

HFCs were introduced to replace CFCs and HCFCs, leading to a rapid increase in their global concentrations over time (Figure 1.16). As HFCs do not contain chlorine, they are not ozone-depleting substances. The primary atmospheric sink of HFCs is oxidation by the OH radical, which results in relatively short atmospheric lifetimes compared to CFCs. Although HFCs do not deplete ozone, they are effective absorbers of IR radiation and, like CFCs and HCFCs, contribute significantly to global warming. As a result, HFC production is regulated by both the Kyoto Protocol and the Montreal Protocol (GML-NOAA, 2024). In 2020, global HFCs emissions were estimated to be approximately 530 Gg yr^{-1}, that is 1200 Tg CO_2-eq yr^{-1} (WMO, 2022).

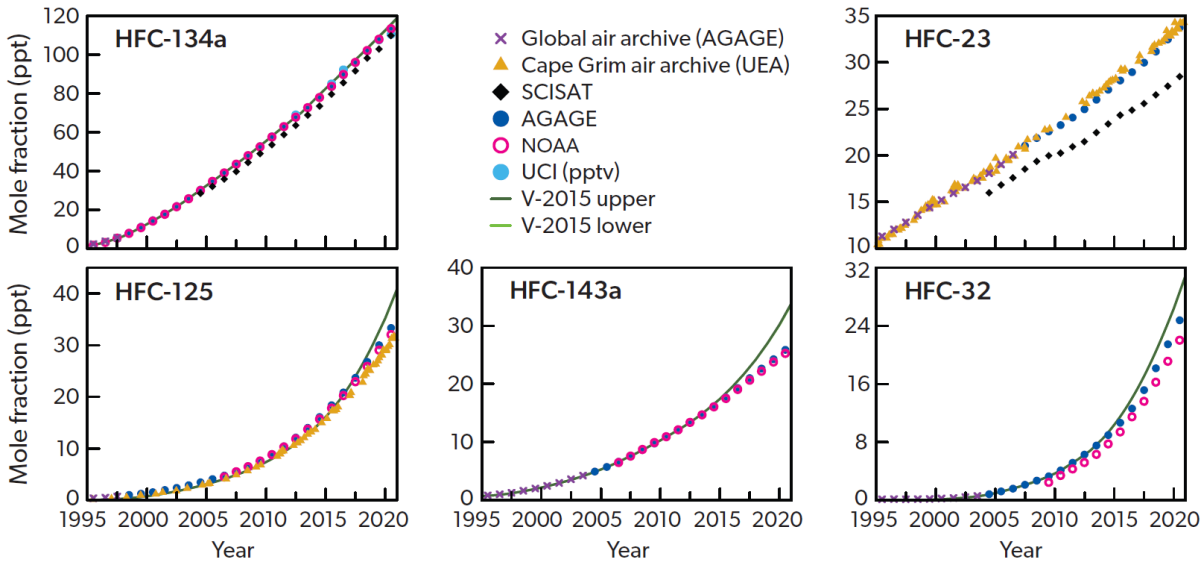

Figure 1.16. Global annual mean mole fractions from ground-based measurement networks (NOAA, AGAGE, and UCI) and projections from Velders et al. (2015) between 1995 and 2020 of the most abundant HFCs. Archive data from AGAGE and the University of East Anglia (UEA) are also shown. Adapted from Fig. 2-1 from WMO (2022).

1.4.3 The Montreal Protocol and its amendments

In 1985, the Vienna Convention for the Protection of the Ozone Layer was negotiated and adopted in response to scientific advancements highlighting ozone depletion and its detrimental effects on human health and the environment. However, the Parties did not mandate specific measures to protect the stratospheric ozone. It was the Montreal Protocol on Substances That Deplete the Ozone Layer, concluded in 1987, that introduced concrete steps toward addressing the issue. The Montreal Protocol is the result of international negotiations aimed at protecting the stratospheric ozone layer by gradually phasing out the use and production of ozone-depleting substances. Initially signed by 46 Parties, the Montreal Protocol came into force in 1989. Today, the Protocol remains relevant and has been ratified by all United Nations Member and Non-member States. The 198 Parties to the Protocol meet annually to review

scientific findings and adapt the treaty as necessary to address new environmental challenges. As a result, the Montreal Protocol has been amended five times since its adoption (see Table 1.2). One of the key achievements of the Protocol is that, due to its implementation, the tropospheric concentration of chlorine from anthropogenic sources reached an absolute maximum in the early 1990s, while the maximum stratospheric chlorine content was observed around the mid-1990s (Figure 1.17), due to the time needed for vertical atmospheric transport and mixing (see Section 1.5).

	Year	Meeting	Modifications
London Amendment	1990	2nd	Complete phase-out of CFCs, halons, and CCl_4 by 2000 (2010) in developed (developing) countries
Copenhagen Amendment	1992	4th	Added HCFCs and CH_3Br to the list, shorter phase-out schedules for CFCs and other ODSs, fund to assist developing countries
Montreal Amendment	1997	9th	Phase-out of HCFCs in developing countries, and phase-out of CH_3Br by 2005 (2015) in developed (developing) countries
Beijing Amendment	1999	11th	Added CH_2BrCl to the list (phase-out by 2004), and harder control on HCFCs production and consumption
Kigali Amendment	2016	28th	Added HFCs to the list (climate change mitigation in addition to ozone protection)

Table 1.2. Amendments to the Montreal Protocol (UNEP, 2020; EPA, 2024).

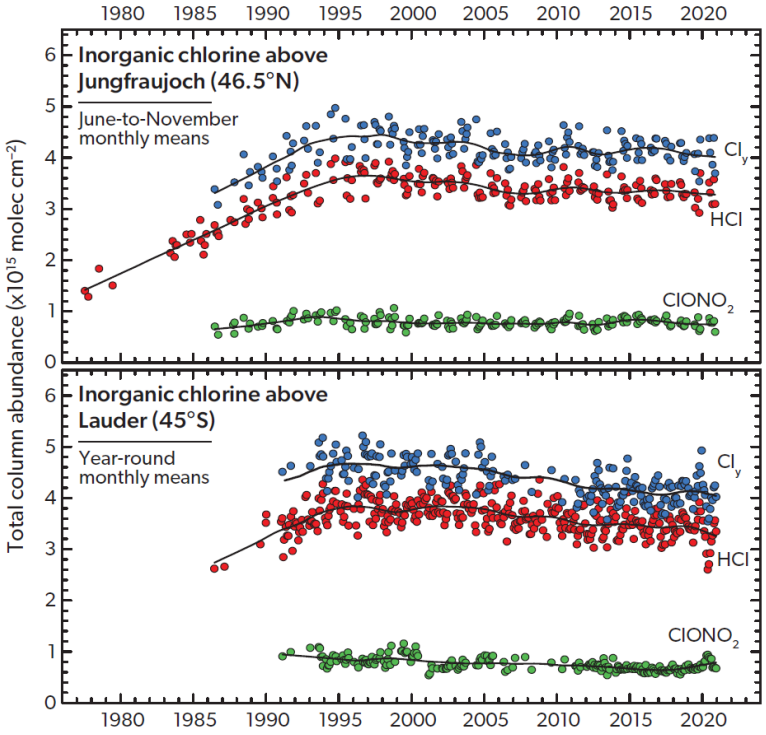

Figure 1.17. Time series of monthly mean total column abundances of HCl (in red) and $ClONO_2$ (in green), the two major stratospheric chlorine reservoirs, measured at two mid-latitude NDACC stations (Jungfraujoch and Lauder). The blue dots represent total inorganic chlorine (Cl_y), obtained as the sum of the HCl and $ClONO_2$ abundances. Fig. 1-12 from WMO (2022).

The most recent amendment to the Protocol, known as the Kigali Amendment, focuses on phasing down HFCs, expanding the Protocol's scope from protecting the ozone layer to also mitigating climate change. It was signed in 2016 and entered into force in 2019. This Amendment is particularly noteworthy as it marked the first time the Montreal Protocol targeted gases that, while not ozone-depleting, contribute to global warming (UNEP, 2020). Projections of HFC emissions without the Kigali Amendment estimate an increase to approximately 10 Gt CO_2-eq yr^{-1} by 2100. In contrast, with the Amendment, emissions would peak at 1.5 Gt CO_2-eq yr^{-1} around 2035 and decrease up to about 0.5 Gt CO_2-eq yr^{-1} in 2100. Consequently, the measures under this Amendment are estimated to prevent 0.3 to 0.5 °C of global warming by 2100 (WMO, 2022).

Figure 1.18 shows the projected long-term changes in equivalent effective stratospheric chlorine (EESC)[13] at mid-latitudes in response to the Montreal Protocol regulations and some of its amendments. The dark purple line represents the estimated trajectory if no protocol had been established, while the other lines illustrate the decrease in EESC resulting from different amendments and adjustements to the Protocol. Finally, the dashed line represents the scenario in which emissions stop in 2023.

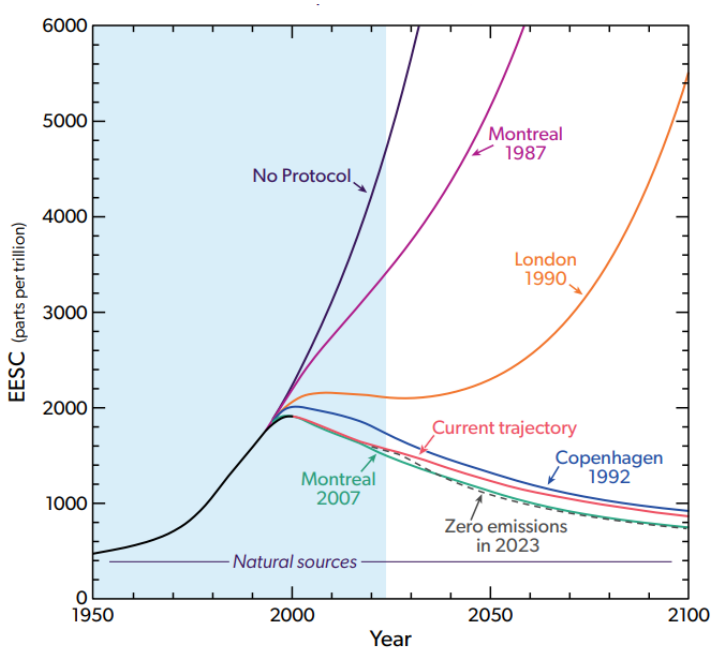

Figure 1.18. Effect of the Montreal Protocol on long-term changes in equivalent effective stratospheric chlorine (EESC). The different lines show the projections of EESC for the midlatitude lower stratosphere. In dark purple, the evolution with no Protocol measurements; in dark fuchsia, the provisions of the original Monteal Protocol; in orange, the London Amendment; in dark blue, the Copenhagen Amendment; in green, the adjustments agreed in 2007; and in red, the current trajectory for EESC. The black dashed curve shows the evolution of EESC assuming zero emissions of ODSs beginning in 2023. Adapted from Fig. Q14-1 from Salawitch et al. (2022).

[13] EESC represents the quantity of halogen compounds available for stratospheric ozone depletion, and it is expressed in parts per trillion (ppt, 10^{-12}).

1.5 Atmospheric circulation and transport

The location and distribution of chemical species in the atmosphere is influenced by both dynamical and chemical processes. Geophysical fluid dynamics help explain how **vertical transport** of chemical constituents is limited by density stratification, due to gravitational forces, while **horizontal movements** are constrained by solar heating, pressure differences, and the Earth's rotation, due to Coriolis force (Brasseur and Solomon, 2005). We can then differentiate the **meridional circulation** (N-S and S-N), along a meridian, and the **zonal circulation**, along a latitude band (E-W and W-E). Large-scale motion primarily occurs horizontally because the atmosphere extends far more in the horizontal than in the vertical direction (Delmas et al., 2005). Consequently, long-lived trace gases are driven by global atmospheric circulation.

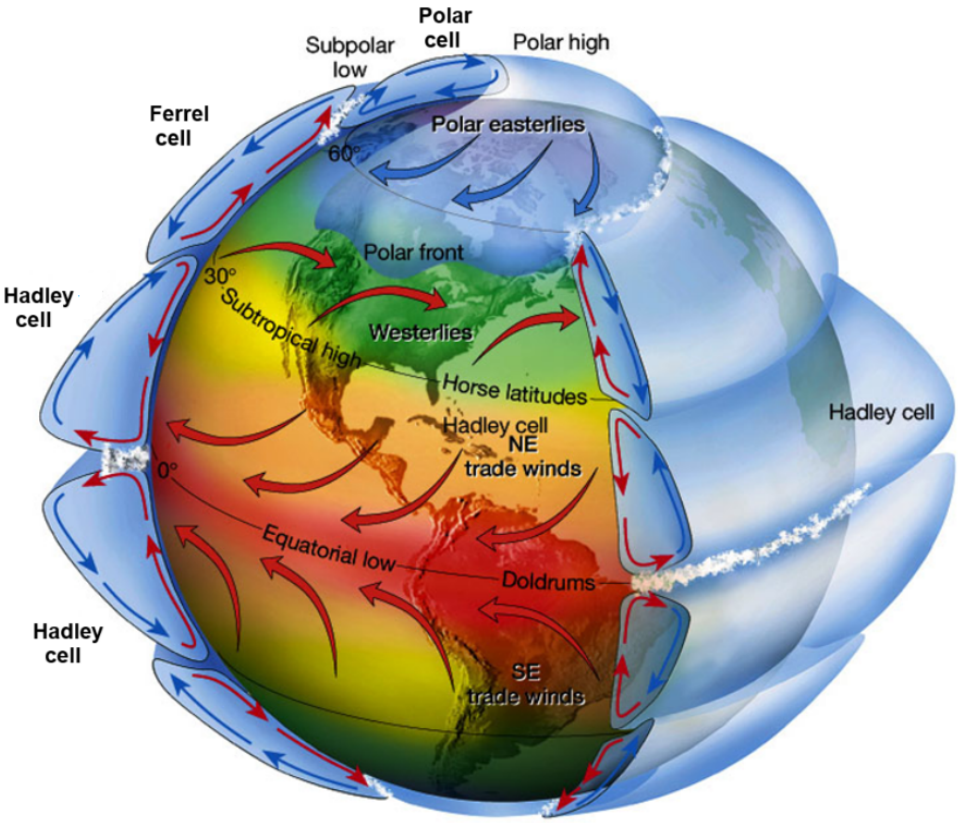

Figure 1.19. Three-cell model of the troposphere. From the equator to the poles, the Hadley, Ferrel, and polar cells are indicated, as well as the low and high pressure regions and the sense of the winds in each area. Adapted from Fig. 7.5 from Lutgens and Tarbuck (2001).

In 1735, George Hadley was the first to describe general atmospheric circulation, taking into account the rotation of the Earth and the warming of tropical regions. He identified the so-called **Hadley cells** in the intertropical region, where warm air rises at the equator, creating low-pressure zones. Then this air flows towards the poles at high altitudes, cools down and sinks at around 30° latitude, forming high-pressure regions that result in arid desert-like conditions. Finally, to close the Hadley cells, the air travels from the high-pressure areas back to the low-pressure equatorial region, generating the **trade winds** (in surface), which blow from the north-east in the Northern Hemisphere (NH), and from the south-east in the Southern Hemisphere

(SH), as shown in Figure 1.19. Thus, the Hadley cells describe a close trajectory, where air flowing poleward at high altitudes and equatorward near the surface. The trade winds, flowing from east to west, are produced by the Coriolis effect, i.e. the rotation of the Earth (from west to east), and differential solar heating. They converge at the Earth's equator, forming the **InterTropical Convergence Zone (ITCZ)**, a region of intense convection, cloud formation, and heavy precipitation. Moreover, the three-cell model includes the Ferrel and polar cells (Figure 1.19). In mid-latitude regions (between 30° and 60° latitude), the air masses of the **Ferrel cells** flow poleward near the surface and equatorward at higher altitudes. Winds in the Ferrel cells are weaker compared to the Hadley cells. At the Ferrel cells, around 12 km high and 30° latitude in both hemispheres, fast-moving air masses flow from west to east. These are known as the **subtropical jet streams**. They are formed by the important pressure gradient produced when warm air masses from the tropics meet cooler air from higher latitudes. The **polar cells** (located between 60° latitude and the poles) circulate in the opposite direction to the Ferrel cells. Consequently, low-pressure areas and storm systems are created between these two cells. **Polar jet streams**, found at around 60° latitude, form where polar cold air masses merge with warmer air from mid-latitudes. The position of jet streams varies with the seasons because of the temperature gradients. In winter, the temperature differences between the warm equator and the cooler subtropical regions, or between the warm equator and the very cold poles, are very sharp, what creates strong pressure gradients in the atmosphere, intensifying the jet streams. Consequently, jet streams travel to the equator in winter, and to the poles in summer, as they weaken due to smaller temperature differences (Delmas et al., 2005).

Regarding the time scales for horizontal transport in the troposphere, air masses circumnavigate the whole globe in only two weeks within a same latitude band (i.e. longitudinal direction) driven by the geostrophic flow[14]. Meridional transport is slower than horizontal transport. Air masses from midlatitude regions take about 1 – 2 months to exchange with tropical or polar regions. Finally, interhemispheric transport takes from 1 to 2 years (Jacob, 1999; Schuck et al., 2024).

The stratospheric meridional transport is governed by the **Brewer-Dobson Circulation (BDC)**, which explains the distribution of chemical tracers like ozone and water vapour. Dobson et al. (1929) measured the total amount of ozone in a vertical column of the atmosphere and observed that ozone concentrations were higher in the polar regions than in the tropics, and that these levels varied seasonally, peaking in spring and reaching a minimum in autumn (Figure 1.12). This study helped the understanding of stratospheric ozone distribution. This led to the definition of the Dobson Unit, which represents the concentration of a trace gas, such as ozone, in a column of air in the atmosphere of the Earth (one DU is equal to 2.6867×10^{20} molec. m^{-2} or 4.4615×10^{-4} mol m^{-2}). The global average of the ozone column is about 300 DU (WMO, 2022). The studies of Brewer (1949) and Dobson (1956) proposed an explanation to the high ozone concentrations above the Arctic in spring, describing the mechanisms that transport gases in the stratosphere. In the case of tracer transport studies, the BDC is considered as composed by two cells, one per hemisphere (Prignon, 2021). As shown in Figure 1.20, this atmospheric circulation represents the upward movement into the tropical stratosphere, followed by the hor-

[14]The **geostrophic flow** is a steady flow (no acceleration) and refers to the motion of a fluid caused by the balance of the pressure-gradient force and the Coriolis force. **Pressure-gradient force** produces the movement of an air parcel from high to low pressure. **Coriolis force** is a deflection due to Earth's rotation. It will bend the parcel trajectory to the right in the NH and to the left in the SH (Jacob, 1999).

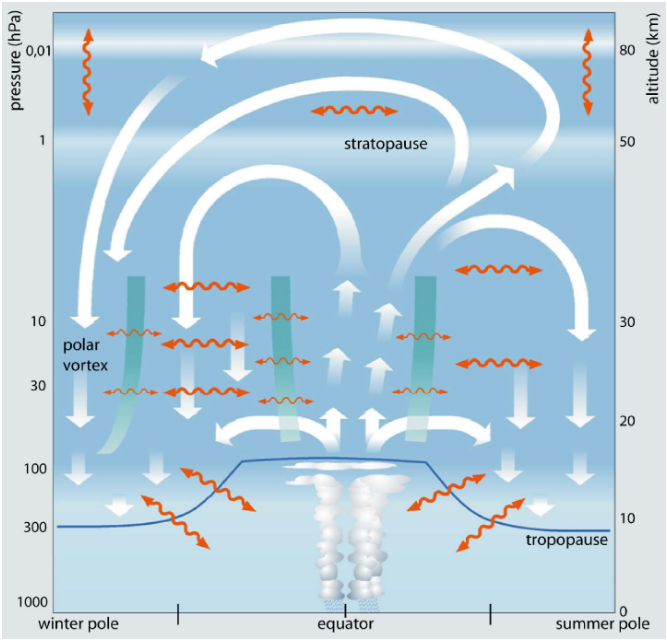

Figure 1.20. Diagram of the Brewer-Dobson Circulation (BDC). The white arrows show the stratospheric residual circulation (net mass transport), wavy orange arrows represent the two-way mixing, and the thick green lines indicate the stratospheric transport and mixing barriers. The mesospheric air masses flow from the summer to the winter pole. Fig. 1 from Bönisch et al. (2011).

izontal drift to high latitude and polar regions, where they descend back into the troposphere, in the winter hemisphere. In the lower stratosphere, there is transport from the tropics to the midlatitudes during the whole year. In the mesosphere, a transport of air from the summer pole to the winter pole, where they go down, is also observed. As well as these vertical exchanges, a two-way mixing is also present (orange arrows in Figure 1.20). This two-way mixing allows transport of chemical tracers but not of mass. Since this mixing needs high potential vorticity gradients, it is limited to the surroundings of the polar vortex and the tropics, creating transport barriers (green lines in Figure 1.20; Butchart, 2014). The BDC is forced by atmospheric waves, called Rossby waves (Butchart, 2014), and has been shown to change in recent decades due to increased greenhouse gases and ozone-depleting substances (e.g. Polvani et al., 2018; Abalos et al., 2019; Prignon et al., 2021).

Typical time scales for vertical transport depend on the sense of movement and the atmospheric layer where they happen. It takes around 1 – 2 days for air to mix within the Planetary Boundary Layer (PBL, first 2 km above the surface), and around one month within the troposphere (from the surface to the tropopause). As a result, species with lifetimes shorter than one month show a vertical gradient, while longer-lived atmospheric species, like CFC-11 and HFC-134a, are well mixed in the troposphere. Troposphere-to-stratosphere exchange is slower due to the temperature inversion in the stratosphere, taking 5 – 10 years for tropospheric air to ascend into the stratosphere, while it takes about 1 – 2 years for the return flow from the stratosphere to the trosposphere (Jacob, 1999). Stratospheric age of air refers to the average time an air parcel needs to be transported from the entry location in the stratosphere to another point within the stratosphere and it varies with altitude (Waugh and Hall, 2002). Similarly, tropospheric age of air can be defined as the mean time needed for a parcel of air to move within the troposphere since it leaved the surface of the Earth (Patra et al., 2009).

Chapter 2

Instruments and methods

The monitoring of the Earth's atmospheric composition has been one of the main focuses of the scientific community since the late 1940s. By analysing its composition, we can understand the physical and chemical processes taking place and evaluate changes to infer its evolution. However, direct atmospheric measurements are not always practicable, so remote sensing techniques, such as Fourier Transform Infrared (FTIR) spectrometers, are often used to record infrared solar absorption spectra. In such cases, inverse methods are required to deduce atmospheric parameters such as the composition.

In addition to FTIR spectrometers, other direct and indirect techniques are employed to monitor atmospheric gases, such as *in situ* measurements and satellite observations. In this study, these methods were used, alongside model simulations, in order to interpret the inversion method and gas abundance retrievals. In this chapter, all these techniques are described, as well as the statistical methods applied for determining the uncertainties affecting the inferred trends.

2.1 FTIR observations

The variation in the Earth's atmospheric composition has been an important research focus, especially since the discovery of the severe stratospheric ozone depletion above Antarctica (Farman et al., 1985). However, atmospheric observations, including the detection of gases such as CH_4 and CO, were conducted several decades earlier by Professor Marcel Migeotte (1948, 1949) from the Institute of Astrophysics of the University of Liège, Belgium. The first atmospheric studies using infrared solar absorption lines to analyse trace gases were performed with grating spectrometers, as related by Zander et al. (2008). Subsequently, solar atmospheric absorption spectra were recorded using ground-based Fourier Transform Spectrometers (FTS), starting recurrently at Kitt Peak National Observatory (USA; 1976), and later at the Jungfraujoch Observatory (Switzerland; 1984).

This section describes the FTIR technique, and the global Network for the Detection of Atmospheric Composition Change (NDACC) of which the Jungfraujoch station, managed by the atmospheric physics laboratory of the University of Liège, is one of the pioneering sites.

2.1.1 FTIR technique

The Fourier Transform Infrared technique enables the estimation of atmospheric gases abundances from infrared solar absoption spectra. This method is employed at every site within the

NDACC-IRWG[1]. FTIR spectrometers operate based on the Michelson interferometer principle. The incident light from the source, sunlight in this case, is collected by a sun tracker and directed to a beam-splitter. At this point, half of the solar beam is reflected at a 90° angle toward a fixed mirror, while the other half is transmitted through the beam-splitter toward a moving mirror. Both beams (reflected and transmitted) are then reflected back to the beam-splitter, where they recombine. The recombined beam is subsequently directed through a collimating lens and to the detector (Figure 2.1). The interference between the two beams produces an interferogram, which is then translated into a spectrum via a Fourier transform, as is standard in FTIR spectroscopy. Figure 2.2 shows an image of the interior of a Bruker IFS-125HR, located at the Izaña Observatory in Tenerife.

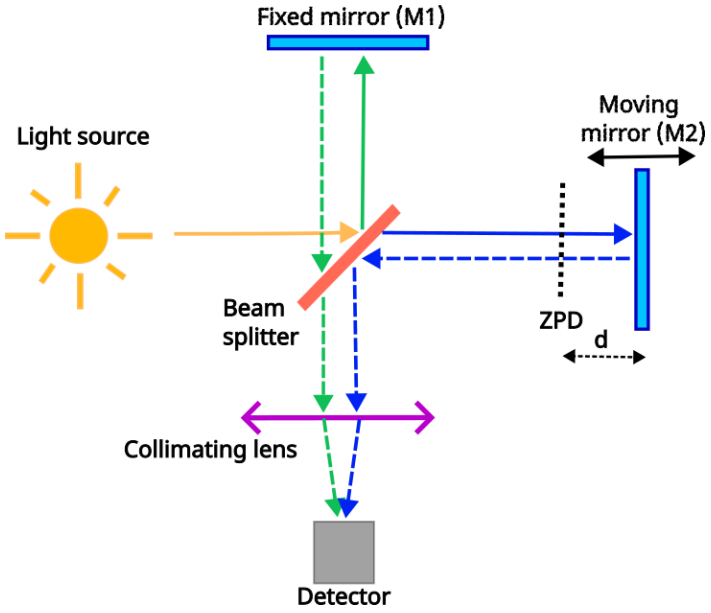

Figure 2.1. Scheme of a Michelson interferometer. The Sun acts as the IR light source. In light blue, the fixed and moving mirrors. Continuous arrows represent the reflected beam (green) and the transmitted beam (blue) after crossing the beam-splitter (orange diagonal rectangle). Dashed arrows show the beams after reflexion in both mirrors before recombination and directed to the detector (grey square). The vertical black dotted line shows the Zero Path Difference (ZPD) position, and d shows the distance of the moving mirror to the ZPD.

The moving mirror can travel from the Zero Path Difference (ZPD) location[2] to its maximum distance, L. The **Optical Path Difference (OPD)** between the two beams travelling through the two arms of the interferometer (reflected and transmitted beams) corresponds to 2d, where d is the displacement of the moving mirror. For simplification, the OPD will be written as x in the theoretical development below. The maximum OPD (OPD_{max}) determines the spectral resolution of the measurement. High OPD_{max} indicate measurements with high spectral resolution, which means a better ability to distinguish closely spaced spectral lines.

[1]NDACC-IRWG: NDACC Infrared Working Group

[2]The distance from the ZPD position to the beam splitter is equal to the distance between the fixed mirror (M_1) and the beam splitter.

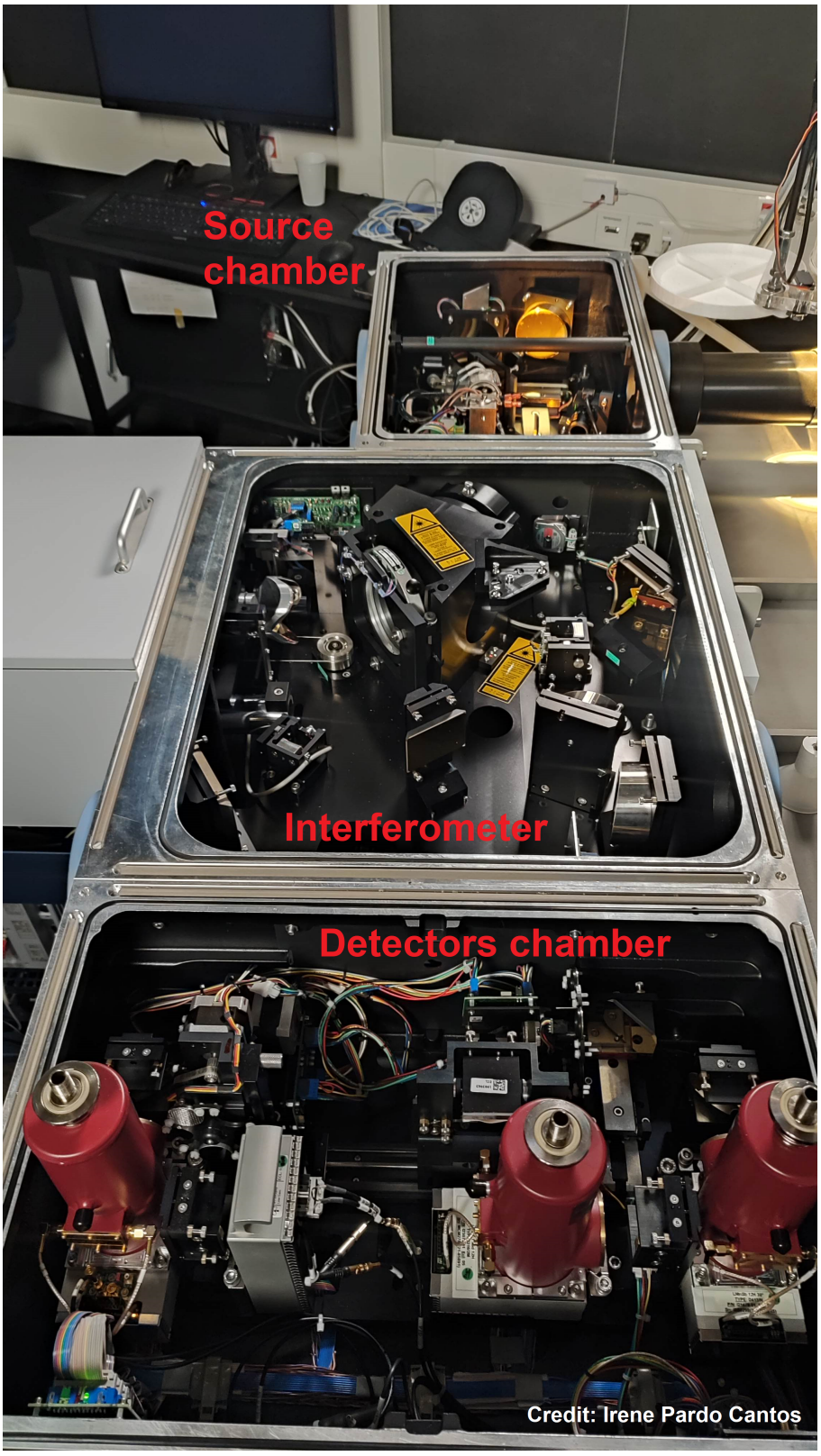

Figure 2.2. Inside of a Bruker IFS-125HR spectrometer, located at the Izaña Atmospheric Observatory in Tenerife, Canary Islands (Spain). From top to bottom: the source chamber, the interferometer chamber, and the detectors chamber.

Considering a monochromatic, infinitely narrow, and collimated incident beam of intensity I_0, the beam-splitter separates the incident beam into two beams of equal intensity, $I_0/2$: one reflected towards the fixed mirror (M_1) and the other transmitted to the moving mirror (M_2). The interferogram of an ideal interferometer is given by:

$$I(x) = I_{M1} + I_{M2} = \frac{I_0}{2}\underbrace{\cos(2\pi \cancelto{0}{d_1}\nu_0)}_{=1} + \frac{I_0}{2}\cos(2\pi \cancelto{x}{d_2}\nu_0) = \frac{I_0}{2}\left[1 + \cos\left(2\pi x \nu_0\right)\right] \tag{2.1}$$

where d_1 and d_2 are the displacements of the mirrors M_1 and M_2, respectively, $\nu_0 = 1/\lambda_0$ is the wavenumber, and λ_0 is the wavelength of the incident light.

Consequently, constructive interference ($I(x) = I_0$) occurs when the entire path (OPD = x) of the beam reflected at the moving mirror corresponds to an integer multiple n of λ ($x = n\lambda$). Note that if n = 0, the moving mirror is located at the ZPD position (x = 0).

At these positions, the intensity of the interfering electromagnetic wave travelling to the detector is at its maximum (Griffiths and Haseth, 2007).

On the other hand, destructive interference ($I(x) = 0$) occurs when the entire path, x, of the beam reflected at the the moving mirror corresponds to an odd multiple of $\lambda/2$ ($x = n\lambda/2$, where n is an odd integer). Hence, the amplitude of the interferogram depends not only on the intensity of the source, but also on the efficiency of the beam-splitter, as well as the characteristics of the detector and the amplifier (Griffiths and Haseth, 2007).

Eq. 2.1 represents the interferogram of a monochromatic light source. However, sunlight is a polychromatic source characterised by a spectral distribution $S(\nu)$. Consequently, the interferogram is given by the sum of each spectral component $d\nu$:

$$I(x) = \int_{-\infty}^{+\infty} S(\nu)\cos(2\pi x \nu)d\nu \tag{2.2}$$

Moreover, considering the instrumental characteristics (e.g. beamsplitter efficiency, detector response, amplifier characteristics), the signal I(x) from the amplifier[3] is modified and can be called $I'(x)$.

$I'(x)$ is expressed in volts (V) and represents the interferogram intensity. $I'(x)$ is defined as the Fourier cosine transform of $S(\nu)$. The **spectrum** is obtained by computing the Fourier cosine transform of $I'(x)$ and can be written as:

$$S(\nu) = \int_{-\infty}^{+\infty} I'(x)\cos(2\pi x \nu)dx \tag{2.3}$$

Since the cosine transform is an even function:

$$S(\nu) = 2\int_{0}^{+\infty} I'(x)\cos(2\pi x \nu)dx \tag{2.4}$$

This is the principle of the **Fourier transform spectrometry** (Griffiths and Haseth, 2007).

[3] An **amplifier** is an electronic device of the FTIR spectrometers that strengthens the weak electrical signals generated by the detector, without introducing significant noise.

Theoretically, the complete spectrum, from 0 to +∞, could be measured at infinitely high resolution if the moving mirror of the interferometer could be displaced to an infinitely far distance x. However, since this ideal case is not physically possible, the spectrum resolution is limited and finite (Griffiths and Haseth, 2007). Thus, the best resolution ($\Delta\nu$) of the spectrum depends on the maximum OPD of the interferometer, which is the length L of the rail on which the moving mirror is displaced, and is given by:

$$\Delta\nu = (x_{max})^{-1} = (OPD_{max})^{-1} = \frac{1}{2L} \tag{2.5}$$

This relationship shows that the spectral resolution improves with a larger displacement of the moving mirror.

To accurately represent the reality and the limitations of the mirror's displacement, we must account for $OPD_{max} = 2L$. Then, Eq. 2.3 becomes:

$$S_{obs}(\nu) = 2\int_0^L I'(x)\cos(2\pi x\nu)dx \tag{2.6}$$

This is equivalent to multiplying the complete interferogram, between $x = -\infty$ and $x = +\infty$, by a boxcar truncation function, B(x), which is defined as:

$$B(x) = \begin{cases} 1 & \text{if } -L \leq x \leq +L \\ 0 & \text{if } L > |L| \end{cases} \tag{2.7}$$

Thus, the observed spectrum is:

$$S_{obs}(\nu) = \int_{-\infty}^{+\infty} I'(x)B(x)\cos(2\pi x\nu)dx \tag{2.8}$$

The convolution theorem states that the Fourier transform of the product of two functions is expressed by the convolution of the Fourier transforms of each individual function. As shown above, the Fourier transform of $I'(x)$ is $\mathscr{F}\{I'(x)\} = S(\nu)$, while the Fourier transform of the boxcar function B(x) is:

$$\mathscr{F}\{B(x)\} = b(\nu) = 2L\frac{\sin(2\pi L\nu)}{2\pi L\nu} = 2L\,\mathrm{sinc}(2\pi L\nu) \tag{2.9}$$

Mathematically, the convolution of the two Fourier transforms, $S(\nu)$ and $b(\nu)$, is then:

$$C(\nu) = S(\nu) * b(\nu) = (S * b)(\nu) = \int_{-\infty}^{+\infty} S(\nu')b(\nu - \nu')d\nu' \tag{2.10}$$

The actual observed spectrum, accounting the instrumental features as well as the physical limitations of the OPD_{max}, is:

$$\boxed{S_{obs}(\nu) = S(\nu) * b(\nu) = S(\nu) * 2L\,\mathrm{sinc}(2\pi L\nu)}$$

where b(ν) is the **Instrumental Line Shape (ILS)** function, which defines the spectral resolution and accuracy of interferometers and spectrometers, showing the instrumental physical limitations. The observed spectrum through the FTIR spectroscopy is then the convolution between the spectrum obtained in an ideal (theoretical) situation and an instrumental sinc function. The sinc function presents a maximum at $\nu = 0$, and has successive local maxima and minima whose amplitudes decrease as $|\nu|$ increases. The observed spectrum is therefore altered by the ILS.

One method to reduce this effect is through the application of **apodization** functions, which diminish the magnitude of the secondary peaks (Griffiths and Haseth, 2007). These functions can be triangular, trapezoidal, or Norton-Beer, among others (Meier, 1997). Nevertheless, apodization functions increase the full width at half-maximum (FWHM) of spectral lines, therefore they decrease the spectral resolution of the measurement (Duchatelet, 2011).

2.1.2 Network for the Detection of Atmospheric Composition Change

To understand the physical and chemical state of the stratosphere and monitor its changes, the Network for the Detection of Stratospheric Change (NDSC) was established in 1986 and became operational in January 1991 (Kurylo, 1991). Its primary objective was to study ozone, primary ozone threats (e.g. Cl, NO_x, Br,...), and other parameters, such as temperature and aerosols that could influence stratospheric ozone. Initially, the NDSC comprised 18 sites, with operational instruments including ground-based Fourier Transform Spectrometers (FTS), lidars, microwave instruments, UV/Visible spectrographs, Dobson/Brewer spectrophotometers, and regular ozone sondes (Paton-Walsh, 2011). Over time, the network expanded its focus to include tropospheric composition changes. In 2005, the NDSC became the Network for the Detection of Atmospheric Composition Change (NDACC[4], De Mazière et al., 2018). Today, it includes 119 research stations worldwide (of which 78 are currently active) and is organised into eleven working groups (WGs). These WGs operate a variety of instruments, adding sondes (ozone, aerosols, water vapor, and backscatter) and UV spectroradiometers to previous NDSC instruments. Some WGs are also dedicated to satellite platforms, theory and analysis, as well as water vapor studies.

This research was conducted within the Infrared Working Group (IRWG), which is composed by 33 different sites (26 active stations in 2025) distributed globally from pole to pole (Figure 2.3; Table A.1). These sites operate high-resolution FTIR spectrometers. The mission of the IRWG[5] consists in recording atmospheric absorption spectra and retrieve concentrations of various atmospheric compounds, including O_3, HF, CO, N_2O, CH_4, and other trace gases. Due to the characteristics of this measurement method, the sampling frequency varies from one site to another, as clear-sky conditions are required to record the solar spectra.

[4] https://ndacc.larc.nasa.gov/

[5] https://www2.acom.ucar.edu/irwg

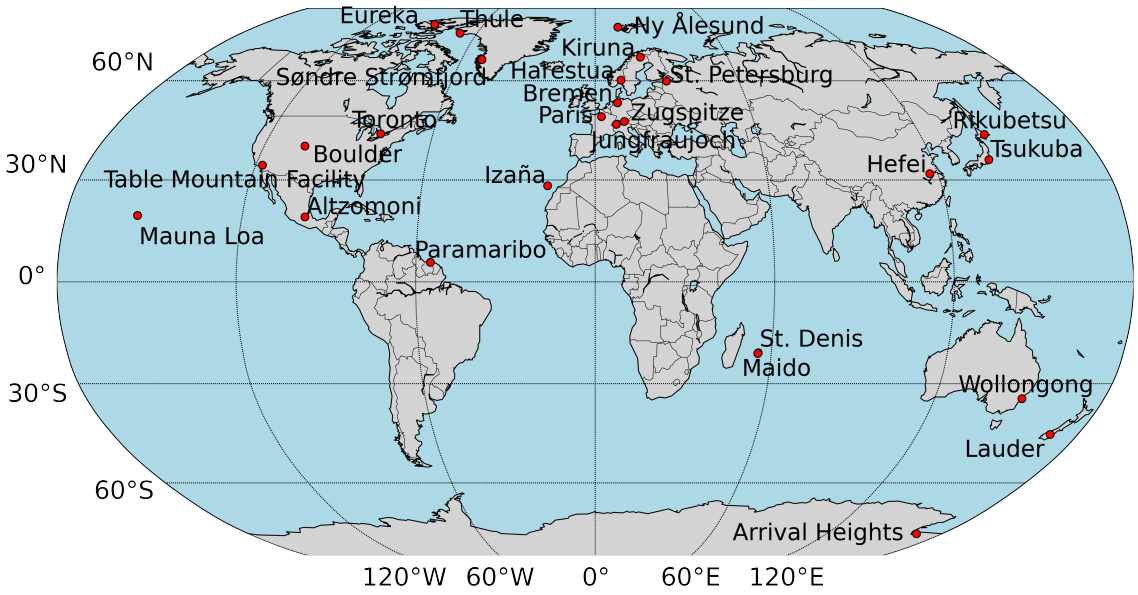

Figure 2.3. Location of the 26 active stations of the NDACC Infrared Working Group (IRWG). Further information about each station can be found in Table A.1.

2.1.3 The Jungfraujoch station

The high-altitude research station Jungfraujoch[6] (Figure 2.4), founded in 1937, is located at the Sphinx Observatory, in the Swiss Alps (46.55°N, 7.98°E), at 3580 m above mean sea level, and nestled between the Mönch (4107 m) and Jungfrau (4158 m) peaks. The Jungfraujoch station was among the first members of the NDSC/NDACC, joining at the start of the network's operation in 1991. In the late 1940s, Professor Marcel Migeotte discovered the presence of CH_4 and CO in the atmosphere (Migeotte, 1948, 1949) during a research visit to Ohio State University in Columbus, Ohio, USA. However, these observations were hampered by significant H_2O and CO_2 interferences due to the site's low altitude and humidity, as well as the limited spectral resolution of his first grating spectrometer. Atmospheric measurements at the Jungfraujoch station began in January 1950 when Professor Migeotte installed a grating spectrometer to study the atmospheric absorption of trace gases and to confirm the presence of CH_4 in an unpolluted atmosphere. The high-altitude conditions of this site significantly reduced interferences, enabling more precise observations (Mahieu et al., 2019). These original spectra, recorded on paper, have been digitised, calibrated, and analysed by the Institute of Environmental Physics team at the University of Bremen, Germany (Makkor et al., 2025).

Molina and Rowland (1974) and Stolarski and Cicerone (1974) published groundbreaking studies on the potential role of the CFCs in stratospheric ozone depletion. As a result, between the mid-1970s and late 1980s, the University of Liège team focused on recording specific spectral regions critical for observing ozone-depleting substances such as HCl, HF, N_2O, as well as O_3 itself. In the early 1980s, the team built its first Fourier transform spectrometer, which measured alongside the existing grating spectrometer until 1989. In the late 1980s, a commercial Bruker IFS-120HR spectrometer, modified by the University of Liège team, was installed at Jungfraujoch and operated, since 1990, simultaneously with the previous FTS until

[6] https://www.hfsjg.ch/en/home/

Figure 2.4. The high-altitude Jungfraujoch research station, located in the Sphinx Observatory (Swiss Alps).

2008 (Mahieu et al., 2019). The Bruker IFS-120HR continued recording high-resolution solar spectra until July 2024, after which it was replaced by a Bruker IFS-125HR spectrometer in September 2024 (Figure 2.5). To ensure a smooth transition and proper calibration between the two spectrometers, a compact medium-resolution Bruker Vertex V80 spectrometer, loaned by the University of Bremen team, was installed in May 2024. This instrument has recorded observations in parallel with the 120HR and 125HR spectrometers, sharing the same solar beam (see Table 2.1).

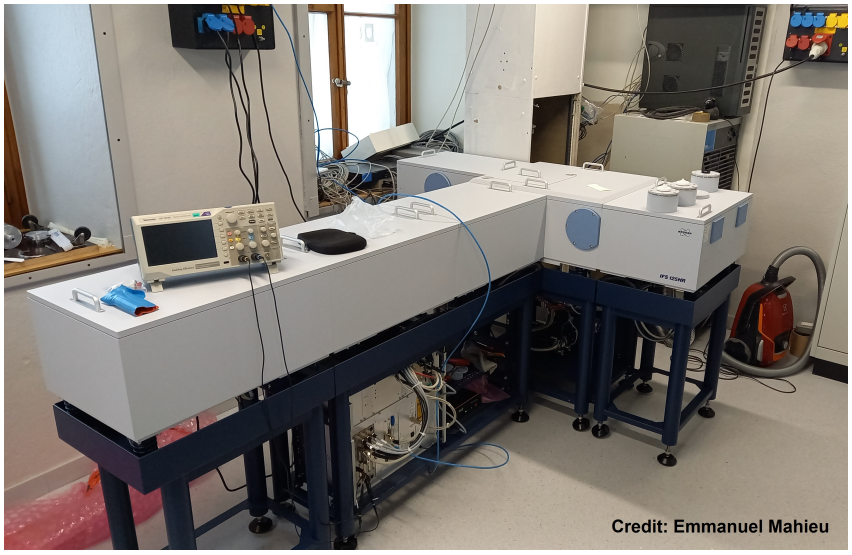

Figure 2.5. Bruker IFS-125HR spectrometer at the Jungfraujoch station (September 2024).

Instrument	Period	Comments
Grating spectrometers	1950 – 1989	Several instruments and versions
Fourier transform spectrometer	1984 – 2008	Homemade by the team of the University of Liège
Bruker IFS-120HR	1990 – July 2024	Modified by the team of the University of Liège
Bruker IFS-125HR	Since Sept. 2024	Using a Bruker Vertex V80 spectrometer simultaneously for intercalibration between the 120HR and the 125HR

Table 2.1. Spectrometers at the Jungfraujoch station from 1950 to 2025. The dates indicated correspond to the periods during which each instrument was in regular operation.

The high altitude and relatively dry atmosphere at Jungfraujoch favour the record of high-quality high-resolution spectra under clear-sky conditions. As well as the homemade spectrometer, the Bruker IFS-120HR spectrometer included two detectors. The Mercury-Cadmium-Telluride (MCT) detector monitors the spectral ranges where CFCs, for example, can be observed, while the Indium-Antimonide (InSb) detector is used for CH_4 and C_2H_6 absorptions. These regions were covered by five distinct optical filters: 350 – 1600, 1600 – 2250, 2200 – 3300, 2800 – 3800, and 3850 – 4400 cm^{-1} (top panel of Figure 2.6; Mahieu et al., 2017). The new Bruker IFS-125HR has an extra filter (1850 – 2850 cm^{-1}), as illustrated in the bottom panel of Figure 2.6. Table 2.2 presents a summary of the specific parameters used in this study.

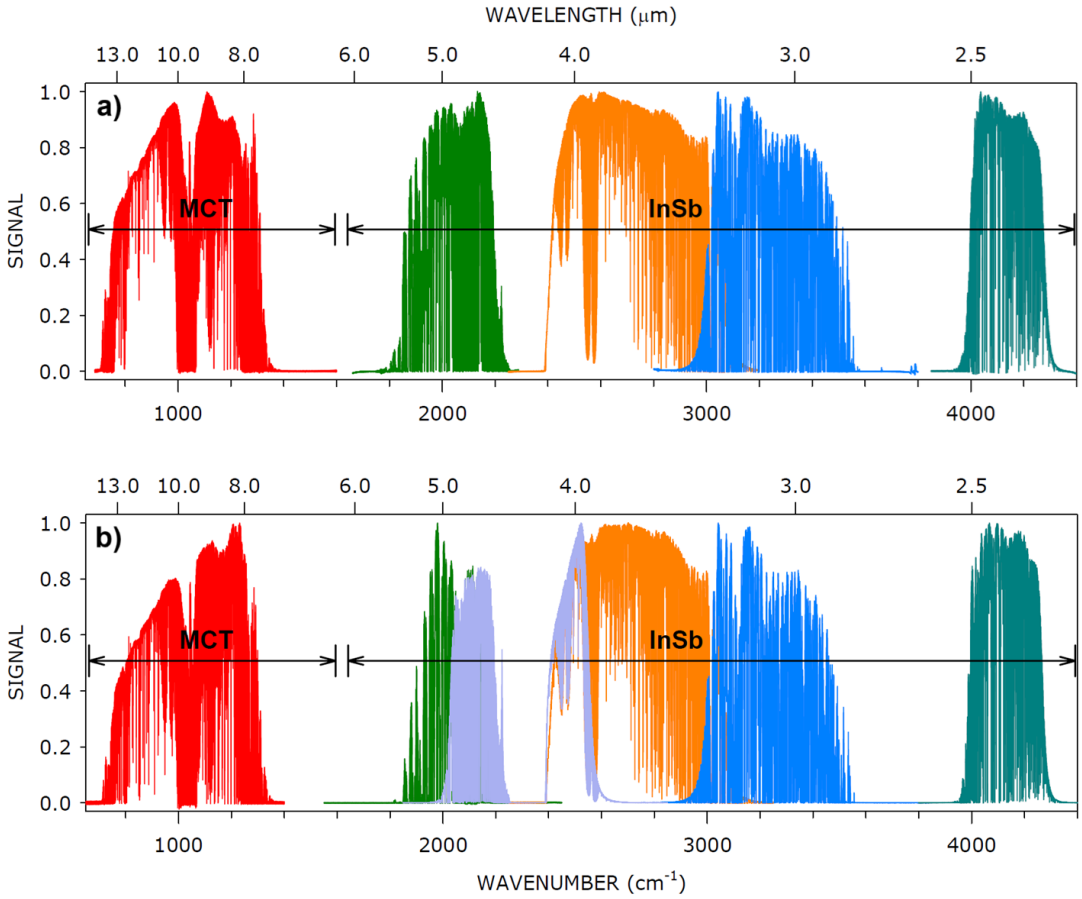

Figure 2.6. The spectral ranges observed at the Jungfraujoch station by the two successive Bruker spectrometers (IFS-120HR (a) and IFS-125HR (b)) using five and six different optical filters, respectively, and indicated by the colours. The two detectors (MCT and InSb) are highlighted by the two horizontal arrows. The represented spectra were recorded on 26th Mars 2012 (Bruker IFS-120HR), and on 6th September and 30th December 2024 (Bruker IFS-125HR). Note that spectra have been normalised. Modified from Mahieu et al. (2017).

The University of Liège team has monitored and progressively developed retrieval strategies for more than 30 atmospheric compounds (Table 2.3). These studies support international agreements such as the Kyoto Protocol, the Paris Agreement, the Montreal Protocol, and operational programmes like the Copernicus Atmosphere Monitoring Service (CAMS[7]).

[7] `http://atmosphere.copernicus.eu`

Instrument	Bruker IFS-120HR
Detector	MCT
Filter	350 – 1600 cm^{-1}
Spectral range	700 – 1400 cm^{-1}
Spectral resolution	0.0061 cm^{-1}
OPD max	82 cm
Apparent SZA	60° – 85°
FOV	5.98 mrad
Aperture	2.5 mm

Table 2.2. Summary of the FTIR parameters used in this study.

Greenhouse gases and support to the Paris Agreement	H_2O, CO_2, CH_4, N_2O, CF_4,SF_6
Related to stratospheric ozone and support to the Montreal Protocol	O_3, NO, NO_2, HNO_3, $ClONO_2$, HCl, HF, COF_2, CFC-11, CFC-12, HCFC-22, HCFC-142b, CCl_4, CH_3Cl, HFC-134a, HFC-23
Air quality and support to the EU-Copernicus programme	CO, CH_3OH, C_2H_6, C_2H_2, C_2H_4, HCN, HCHO, HCOOH, NH_3, PAN
Other	OCS, N_2, isotopic derivatives

Table 2.3. Atmospheric gases monitored at the Jungfraujoch station. Updated from Mahieu et al. (2019).

2.2 Inverse methods

Remote measurements are used accross various fields, from astrophysics to medical tomography, passing by seismic and atmospheric observations. They offer the possibility of collecting information about the Earth's atmospheric composition from a distance, without direct contact. However, the main characteristic of this technique is not the remoteness of the measurement but its indirect nature, which introduces complex interpretation challenges known as **inverse problems**. The inversion of complicated functions is necessary to deduce the most accurate representation of the causes underlying the measurements (Rodgers, 2000).

To evaluate the quality of the retrieved parameters and of the inversion method, the description of the information content of the retrievals is essential, as well as the coherence between the estimated and the true states of the system. This process involves performing a complete error analysis, the optimisation of the measuring devices, and the final validation of the results (Rodgers, 2000).

With the FTIR technique, the inverse problem involves deriving the vertical distribution and abundance of atmospheric gases from IR solar absorption spectra. Information about the vertical distribution may be inferred from line broadening (Section 1.3.2.3). The line center provides information about the highest altitudes, while the wings of the line reflect conditions at the lower altitudes of the vertical distribution. Atmospheric abundances are determined from the area within a spectral absoption line of the studied gases. These abundances are expressed as total vertical columns or, where possible, partial columns. They are defined as the sum of all molecules of a target gas contained in a squared section column spanning over the entire vertical column of the atmosphere, i.e. from the measurement station altitude to the top of the atmosphere, per unit area (units: molec. cm^{-2}) (Duchatelet, 2011).

Remote observations inherently provide limited information on the vertical distribution due to factors such as the measurement noise. As a result, only a limited amount of information can be retrieved from the inversion process. That means that the inverse problem is mathematically ill-posed, or underconstrained, as there are more unknowns than equations, leading to a non-unique solution (Rodgers, 2000). To address this, constraints, for example the vertical resolution of the inverted profile, are added to help inversion algorithms to converge and estimate the abundance of atmospheric gases. The retrieved profiles should not be considered as measurements of the state of the atmosphere, but rather as estimations derived from the measurements, an *a priori* state of the atmosphere, and their associated uncertainties (Duchatelet, 2011).

The inversion method applied in this study is the Optimal Estimation Method (OEM), based on Bayes' Theorem, of Rodgers (2000) and implemented in the SFIT4 retrieval algorithm (Hannigan et al., 2024). This formalism facilitates error analysis and the characterisation of retrievals, enabling an understanding of the relationship of a retrieval with the true state of the system. Such analysis is critical for optimising the retrieval characteristics.

In this section, the basic concepts of the Rodgers (2000) formalism are introduced.

2.2.1 Statement of the problem

Let $\mathbf{y}$ be the measurement vector, which is a function $\mathbf{f}$ of the unknown state vector $\mathbf{x}$ and other parameters $\mathbf{b}$ not necessarily known previously:

$$\mathbf{y} = \mathbf{f}(\mathbf{x}, \mathbf{b}) + \mathbf{e} \tag{2.11}$$

where $\mathbf{e}$ is the measurement noise vector, which represents the random or experimental error from different sources (e.g. detector's noise). The function $\mathbf{f}$ is referred to as the **forward function**. The state vector $\mathbf{x}$ describes the state of the atmosphere and represents the quantities to be retrieved (e.g. vertical profile). The set of parameters $\mathbf{b}$ are called the **forward function parameters**, and they represent quantities that influence the measurement but are not retrieved (e.g. spectral line intensities, OPD of the instrument). This model describes the physics of the measurement, including details about the instrument and the radiative transfer model, which connects the observed signal to the state of the atmosphere.

2.2.2 Inversions: the retrieval method

The goal of this method is to iterate calculations to find the best estimate of the true state of the atmosphere that caused the observed parameters. To perform this inversion, a **retrieval method R** is needed:

$$\hat{\mathbf{x}} = \mathbf{R}(\mathbf{y}, \hat{\mathbf{b}}, \mathbf{x}_\mathrm{a}, \mathbf{c}) \tag{2.12}$$

where $\hat{\mathbf{x}}$ represents the estimated state vector, rather than the true state, i.e. the estimated state of the target quantity to retrieve. Similarly, $\hat{\mathbf{b}}$ is the best estimate of the forward function parameters. Since prior information about the system is necessary, the vector $\mathbf{x}_\mathrm{a}$ represents the

a priori estimate of the state vector $\mathbf{x}$. Finally, $\mathbf{c}$ refers to the **retrieval method parameters**, which include other parameters specific to the retrieval method (e.g. convergence criteria). The vectors $\mathbf{x}_a$ and $\mathbf{c}$ represent parameters that are not included in the forward function $\mathbf{f}$.

Substituting Eq. 2.11 into Eq. 2.12:

$$\hat{\mathbf{x}} = \mathbf{R}\left[\mathbf{f}(\mathbf{x},\mathbf{b}) + \mathbf{e}, \hat{\mathbf{b}}, \mathbf{x}_a, \mathbf{c}\right] \tag{2.13}$$

This transfer function includes both the instrument and the retrieval method, describing the operation of the entire system. The transfer function helps characterise the observing system and understand how sensitive the retrieval is to the true state. Furthermore, error analysis is also needed to study the sensitivity of the retrieval to each source of error, such as measurement noise, errors in the forward model, transfer function, non-retrieved parameters, and retrieval method parameters.

In the case of the FTIR technique, the forward function can be too complex because of the complexity of the actual physical system. To simplify it, a **Forward Model F** can be developed to approximate the forward function and ignore certain forward function parameters **b'**:

$$\mathbf{F}(\mathbf{x},\mathbf{b}) \approx \mathbf{f}(\mathbf{x},\mathbf{b},\mathbf{b'}) \tag{2.14}$$

Since the transfer function is non-linear, it must be linearised[8] with respect to the independent parameters in order to approximate it around a specific point.

We substitute the forward function $\mathbf{f}$ with the forward model $\mathbf{F}$ in Eq. 2.13:

$$\hat{\mathbf{x}} = \mathbf{R}\left[\mathbf{F}(\mathbf{x},\mathbf{b}) + \mathbf{e}, \hat{\mathbf{b}}, \mathbf{x}_a, \mathbf{c}\right] \tag{2.15}$$

The linearisation is done in two steps:

1. First, the forward model may be linearised about $\mathbf{x} = \mathbf{x}_a$, $\mathbf{b} = \hat{\mathbf{b}}$:

$$\hat{\mathbf{x}} = \mathbf{R}\left[\mathbf{F}(\mathbf{x}_a,\hat{\mathbf{b}}) + \underbrace{\frac{\partial \mathbf{F}}{\partial \mathbf{x}}}_{=\mathbf{K}_x}(\mathbf{x}-\mathbf{x}_a) + \underbrace{\frac{\partial \mathbf{F}}{\partial \mathbf{b}}}_{=\mathbf{K}_b}(\mathbf{b}-\hat{\mathbf{b}}) + \mathbf{e}, \hat{\mathbf{b}}, \mathbf{x}_a, \mathbf{c}\right] \tag{2.16}$$

where $\mathbf{K}_x$ and $\mathbf{K}_b$ are the Jacobian matrices, exhibiting the sensitivity of the forward model to the state and to the forward model parameters, respectively.

2. Then the retrieval method $\mathbf{R}$ is linearised with respect to its first argument $\mathbf{y}$:

$$\hat{\mathbf{x}} = \mathbf{R}\left[\mathbf{F}(\mathbf{x}_a,\hat{\mathbf{b}}), \mathbf{x}_a, \mathbf{c}\right] + \mathbf{G}_y\left[\mathbf{K}_x(\mathbf{x}-\mathbf{x}_a) + \mathbf{K}_b(\mathbf{b}-\hat{\mathbf{b}}) + \mathbf{e}\right] \tag{2.17}$$

where $\mathbf{G}_y = \partial\mathbf{R}/\partial\mathbf{y}$ is the Jacobian representing the sensitivity of the retrieval to the measurements.

[8] Linearising aids in approximating the cost function in an iterative method, as in this case. We can linearise the function using the Taylor expansion, keeping only the first-order terms.
The **cost function** quantifies the error of a model. Minimising the cost function aims to find the parameters of the model to find the best estimate.

During the iterations, the forward model tries to simulate the measurements as accurately as possible, starting from the *a priori* state and minimising the residuals[9] through a least-squares procedure. The best estimate of the state of the system is then achieved.

Since the *a priori* represents the system before the measurements, if the retrieval method used is correct, the measurement should align with the state, and the first term of Eq. 2.17 should match the *a priori* state. If this is not the case, the retrieval method needs to be revised.

2.2.3 Information content

The characterisation of the retrievals is performed by analysing the information content, which involves studying the relationship between the retrieval and the true state of the atmosphere.

Based on the mathematical developments and assumptions above, Eq. 2.17 can be simplified as follows:

$$\hat{\mathbf{x}} = \mathbf{x}_a + \mathbf{A}(\mathbf{x} - \mathbf{x}_a) + \mathbf{G}_y\mathbf{e}_y = (\mathbf{I}_n - \mathbf{A})\mathbf{x}_a + \mathbf{A}\mathbf{x} + \mathbf{G}_y\mathbf{e}_y \tag{2.18}$$

where $\mathbf{e}_y$ is the total error in the measured signal relative to the forward model and is defined as:

$$\mathbf{e}_y = \mathbf{K}_b(\mathbf{b} - \hat{\mathbf{b}}) + \mathbf{e} \tag{2.19}$$

and $\mathbf{A} = \mathbf{G}_y\mathbf{K}_x = \partial\hat{\mathbf{x}}/\partial\mathbf{x}$ is called the **averaging kernel matrix**, which characterises the sensitivity of the retrieval to the true state. $\mathbf{I}_n$ is the identity matrix of dimension n. The term $(\mathbf{I}_n - \mathbf{A})\mathbf{x}_a$ represents the contribution of the *a priori* state $\mathbf{x}_a$ to the retrieved state $\hat{\mathbf{x}}$, while the term $\mathbf{A}\mathbf{x}$ represents the contribution of the true state $\mathbf{x}$ to the retrieved state.

In an ideal case, the averaging kernel matrix would be equal to the identity matrix. However, since the inverse method applied to FTIR observations is not ideal, $\mathbf{A}$ is different from the identity matrix. This implies that the rows of $\mathbf{A}$ are smoothing functions that peak at specific altitudes. Moreover, the full width at half-maximum of these functions indicates the vertical resolution of the system (Figure 2.7).

The term $\mathbf{G}_y\mathbf{e}_y$ represents the error in the retrieval, which arises from the total measurement error, rather than the retrieval method itself. It is called the **retrieval error**.

In summary, Eq. 2.18 demonstrates that the retrieval is influenced by the *a priori* state, the sensitivity of the retrieval to the true state (through $\mathbf{A}$), and the retrieval error.

The averaging kernel matrix also allows to determine another indicator of the information content of the retrievals. This is the **Degrees Of Freedom for Signal (DOFS)** and indicates the number of independent vertical pieces that can be obtained from the retrieved vertical profiles. This value is equal to the trace[10] of the averaging kernel matrix. More information can be obtained from the eigenvectors and eigenvalues of $\mathbf{A}$. The shape of the eigenvectors reveals the limits of each independent vertical part of the retrieved profile, while the eigenvalues indicate

[9] The **residuals** are the differences between the estimated/calculated state and the measurement.

[10] The **trace** of a square matrix is the sum of its diagonal elements. It is also the sum of the eigenvalues of the matrix.

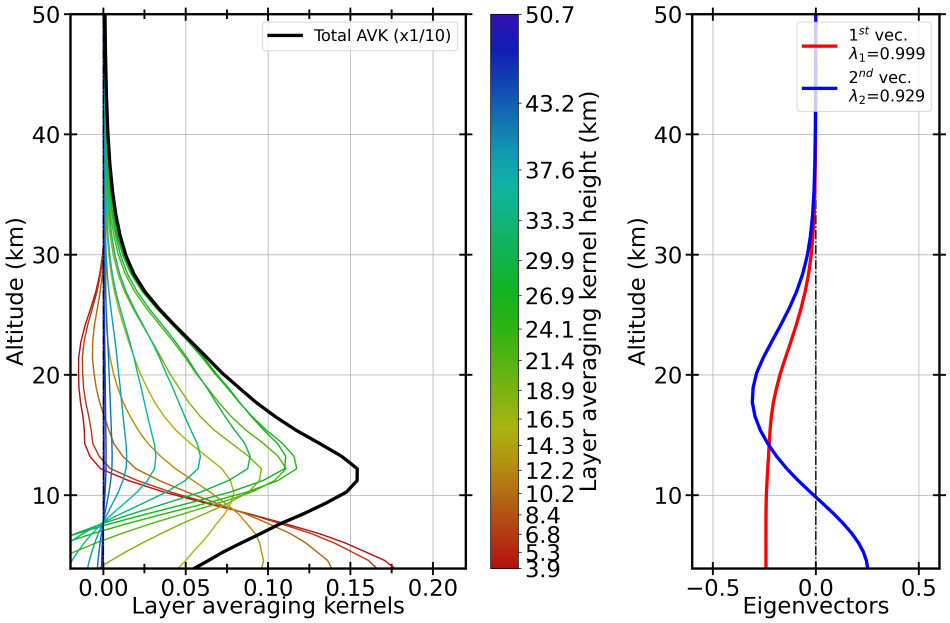

Figure 2.7. Example of mean layer averaging kernels (left), as well as the two first eigenvectors and eigenvalues (right) for spectra recorded at the Jungfraujoch station. The ticks on the colour bar are the individual layer averaging kernels represented in the plot. This figure corresponds to the retrievals of CFC-12.

the fraction of information coming from the retrieval, instead from the *a priori* profile, for the corresponding eigenvector. An example of the averaging kernels, eigenvectors, and eigenvalues is shown in Figure 2.7. The coloured lines in the averaging kernel plot represent the individual layer averaging kernels, while the black line depicts the total column averaging kernel (scaled by 0.1), spanning from the site altitude (Jungfraujoch, 3.58 km) up to 50 km. The DOFS is equal to 2, meaning that two independent pieces of information can be obtained from the retrievals. The full width at half-maximum of the total column averaging kernel indicates a total vertical resolution of approximately 20 km. The FWHM of the first lobe of the averaging kernels and the second eigenvector (intersection of the eigenvector with the vertical axis) suggest that the first partial column extends from the station location up to ≈10 km, while the second partial column extends from ≈10 km to 20 km. The first eigenvalue, equal to 0.999, indicates that approximately 100% of the information characterising the troposphere comes from the retrieval rather than the adopted *a priori* profile. The second eigenvalue, equal to 0.929, suggests that another partial column can be obtained above 10 km, with nearly 93% of the information coming from the retrieval.

2.2.4 Error analysis

As described in the Rodgers (2000) formalism, the error in the retrieved state can be separated into four components: the smoothing error, the forward model parameter error, the forward model error, and the retrieval noise. After some rearrangement of Eq. 2.18, Rodgers (2000) expresses these terms as follows:

$$\hat{\mathbf{x}} - \mathbf{x} = (\mathbf{A} - \mathbf{I}_n)(\mathbf{x} - \mathbf{x}_a) + \mathbf{G}_y\mathbf{K}_b(\mathbf{b} - \hat{\mathbf{b}}) + \mathbf{G}_y\Delta\mathbf{f}(\mathbf{x}, \mathbf{b}, \mathbf{b}') + \mathbf{G}_y\mathbf{e} \tag{2.20}$$

2.2.4.1 Smoothing error

The first term on the right side of Eq. 2.20 represents the smoothing error. Remote observing systems are characterised by limited vertical resolution, so the retrieved state can be interpreted as an estimate of a state that has been smoothed by the averaging kernels, or as the estimate of the true state with an error contribution caused by smoothing.

Since the true state $\mathbf{x}$ is not known, the actual smoothing error cannot be directly estimated. In this case, a statistical representation of the error is required, which can be obtained from the mean and covariance over an ensemble of states. The mean is $(\mathbf{A} - \mathbf{I}_n)(\overline{\mathbf{x}} - \mathbf{x}_a)$, and the covariance of the smoothing error about the mean state $\overline{\mathbf{x}}$ is given by:

$$\mathbf{S}_s = (\mathbf{A} - \mathbf{I}_n)\mathbf{S}_{es}(\mathbf{A} - \mathbf{I}_n)^T \tag{2.21}$$

where $\mathbf{S}_{es}$ is the covariance of an appropriate ensemble of states around the mean state $\overline{\mathbf{x}}$. This covariance matrix represents the natural variability of the state vector and can be generated using a climatology (see Section 2.2.5.1) from an independent dataset, or through an *ad hoc* matrix equal to the covariance matrix of the *a priori* when the climatology is unavailable. However, the latter approach is not ideal and it would be better not to attempt to estimate the smoothing error directly, and simply consider the retrieval as an estimate of a smoothed state, rather than as an estimate of the complete state.

2.2.4.2 Forward model parameter error

The forward model parameter error corresponds to the second term on the right side of Eq. 2.20. This error arises from inaccuracies in the forward model parameters. In this term, $\mathbf{G}_y$ represents the sensitivity of the retrieval to the measurement, and $\mathbf{K}_b$ denotes the sensitivity of the forward model to its parameters, while $(\mathbf{b} - \hat{\mathbf{b}})$ represents the bias in the estimated model parameters, as indicated above. If $\mathbf{K}_b$ is too large for a specific element of $\mathbf{b}$, three conditions must be analysed: (1) a more precise measurement of this element of $\mathbf{b}$ must be executed; (2) this element could come from the state vector rather than from the forward model parameters; (3) the observing system should be redesigned to reduce sensitivity to this element.

The error covariance matrix for the forward model parameter error is given by:

$$\mathbf{S}_f = \mathbf{G}_y\mathbf{K}_b\mathbf{S}_b\mathbf{K}_b^T\mathbf{G}_y^T \tag{2.22}$$

where $\mathbf{S}_b$ is the error covariance of $\mathbf{b}$. This error can include both random and systematic components (see Section 2.2.4.5).

2.2.4.3 Forward model error

The modelling error is given by the third term on the right side of Eq. 2.20 and indicates the error generated by the forward model itself, rather than by its parameters:

$$\mathbf{G}_y\Delta\mathbf{f} = \mathbf{G}_y\left[\mathbf{f}(\mathbf{x},\mathbf{b},\mathbf{b}') - \mathbf{F}(\mathbf{x},\mathbf{b})\right] \tag{2.23}$$

As observed, this error is evaluated at the true state $\mathbf{x}$, with the true value of the model parameters $\mathbf{b}$, rather than at the estimated values $\hat{\mathbf{x}}$ and $\hat{\mathbf{b}}$. This error can be difficult to estimate because a perfect model for $\mathbf{f}$, including the correct physics, is not always available. The forward model error is mainly systematic.

2.2.4.4 Retrieval noise

The last term in Eq. 2.20 represents the retrieval noise, which corresponds to the measurement noise. This component is the easiest to estimate and is typically random. Its covariariance matrix is well known:

$$\mathbf{S}_\mathrm{m} = \mathbf{G}_\mathrm{y}\mathbf{S}_\mathrm{e}\mathbf{G}_\mathrm{y}^\mathrm{T} \tag{2.24}$$

where $\mathbf{S}_\mathrm{e}$ is the measurement error covariance matrix.

2.2.4.5 Random and systematic errors

Random and systematic errors are two wide categories used to classify uncertainties based on their origin and effects in the results. On the one hand, **random errors** change unpredictably and are caused by unknown factors. They result in scatter around the true value and can be reduced by averaging numerous measurements. Measurement noise is typically an example of a random error. On the other hand, **systematic errors** are constant between measurements and are usually caused by the experimental setup or the methodology employed. They produce a constant bias in the results, meaning they can often be identified and reduced, or even corrected in some cases. An example of a systematic error is miscalibration of the measuring instrumentation or the systematic uncertainty on spectroscopic parameters.

2.2.5 The optimal solution

As introduced earlier, an interative process is necessary to reach the optimal solution in FTIR inversions. Since the forward model is non-linear, a non-linear least-squares iterative method is necessary. One example is the Gauss-Newton method, which involves linearising a non-linear model around a starting point (the first guess) and updating this value through iterations to minimise the residuals. The *a priori* state is the best estimate of the true state of the atmosphere before the measurement and is typically used as the first guess in the iterations:

$$\mathbf{x}_{\mathrm{i}+1} = \mathbf{x}_\mathrm{i} + \left(\mathbf{R}_\mathrm{m} + \mathbf{K}_\mathrm{i}^\mathrm{T}\mathbf{S}_\mathrm{e}^{-1}\mathbf{K}_\mathrm{i}\right)^{-1}\left[\mathbf{K}_\mathrm{i}^\mathrm{T}\mathbf{S}_\mathrm{e}^{-1}(\mathbf{y} - \mathbf{F}(\mathbf{x}_\mathrm{i})) - \mathbf{R}_\mathrm{m}(\mathbf{x}_\mathrm{i} - \mathbf{x}_\mathrm{a})\right] \tag{2.25}$$

where $\mathbf{K}_\mathrm{i} = \mathbf{K}(\mathbf{x}_\mathrm{i})$ is the Jacobian matrix of the forward model $\mathbf{F}$ with respect to $\mathbf{x}$; $\mathbf{S}_\mathrm{e}$ is the measurement error covariance matrix; and $\mathbf{R}_\mathrm{m}$ is the regularisation matrix. The subscript i indicates the iteration index. Through a series of iterations, the estimated state is fitted to the measurement via a non-linear least squares method by minimising the residuals. The optimal solution is obtained when the method converges.

In the square brackets of Eq. 2.25, the first term indicates the contribution of the measurement to the retrieved profile, i.e. the ability of the forward model to reproduce the measurement. The second term shows how the *a priori* state constraints the shape of the retrieved profile through the regularisation matrix $\mathbf{R}_\mathrm{m}$. If $\mathbf{R}_\mathrm{m} = \mathbf{I}$, the retrieved profile is simply obtained by multiplying the *a priori* profile by a scaling factor. However, there are two other main types of constraints in atmospheric inverse problems: climatological and smoothing constraints (Duchatelet, 2011).

2.2.5.1 Climatological regularisation

In addition to the "first guess" and "*a priori* state" defined earlier, another important term is "climatology", which refers to the mean and covariance of an ensemble of states. A climatology can sometimes provide a good *a priori* estimate. In this case, the *a priori* covariance matrix, $\mathbf{S}_\mathrm{a}$, contains a broad number of profiles from climatological datasets to account for the natural variability of the target gas. Satellite measurements can be an excellent source of information for constructing such datasets.

In the case of climatological constraints, the regularisation matrix, $\mathbf{R}_\mathrm{m}$, is a square matrix of dimension $\mathrm{n} \times \mathrm{n}$ and is equal to the inverse of the *a priori* covariance matrix, $\mathbf{S}_\mathrm{a}^{-1}$. In most cases, this method is referred to as the Optimal Estimation Method (OEM), although it is technically an abuse of terminology, as this is the name of the entire inverse method described in Rodgers (2000) (Duchatelet, 2011). However, it is very complicated to build a complete covariance matrix because of the lack of data for profiles at certain altitudes or times. Therefore, *ad hoc* matrices, which are diagonal, are often used. Additionally, extra-diagonal elements may be also defined to represent the inter-layer correlation between gas concentrations at different altitudes.

2.2.5.2 Smoothing regularisation

In the case of smoothing constraints, the regularisation matrix is given by $\mathbf{R}_\mathrm{m} = \alpha \mathbf{L}^\mathrm{T}\mathrm{L}$, where α is a parameter indicating the strength of the constraint and $\mathbf{L}$ is the constraint operator. The most popular smoothing constraint is the Tikhonov-Phillips (or simply Tikhonov) regularisation (Tikhonov et al., 1995). In the first-order Tikhonov regularisation, the constraint operator $\mathbf{L}$ is:

$$\mathbf{L} = \begin{pmatrix} -1 & 1 & 0 & \dots & 0 \\ 0 & -1 & 1 & \dots & 0 \\ \vdots & \vdots & \vdots & \ddots & \vdots \\ 0 & \dots & 0 & -1 & 1 \end{pmatrix} \tag{2.26}$$

The dimension of the $\mathbf{L}$ matrix is $(\mathrm{n}-1) \times \mathrm{n}$. This operator constrains the shape of the retrieved profile of the target gas, rather than its absolute values, which are determined from the measurement. This is the main difference between climatological and smoothing regularisations: climatological regularisation operators have information about the absolute values due to the natural variability included in $\mathbf{S}_\mathrm{a}$.

To determine the optimal strength parameter α, some tests need to be performed. These are mainly based on the analysis of the DOFS and the residuals, as they characterise the information

content of the retrievals and the accuracy of the forward model to find the best estimation. If the applied constraint is too strong, the retrieved profile will closely resemble the *a priori* profile (scaling retrieval) and the DOFS will be close to unity. Conversely, if the constraint is too weak, the DOFS will approach the number of vertical layers in the forward model, and the retrieved profile will not represent the true state (unconstrained oscillating profile retrieval). Therefore, an equilibrium must be found between these two extremes to achieve the best representation of the state of the atmosphere with reasonable DOFS and residuals (Duchatelet, 2011).

2.2.6 The SFIT4 algorithm

SFIT4 is a line-by-line, non-linear spectral fitting algorithm used in this study. It evolved from previous versions, SFIT and SFIT2, developped by NASA's Langley research center (USA)[11], the NIWA Lauder atmospheric research station (New Zealand)[12], and the University of Denver (USA). The current version is SFIT4 v1.0.21, though earlier versions, in particular v0.9.4.4 and v1.0.18, have been used for retrieving CFC-11 and HFC-134a profiles, respectively.

In SFIT4, both regularisation methods discussed earlier (OEM and Tikhonov) are implemented, allowing for the retrieval of atmospheric chemical profiles in both ways. The choice of method depends on the target species and the adopted retrieval strategy (Hannigan et al., 2024).

The spectroscopic data required for the forward model is obtained from the HITRAN[13] and ATM[14] databases. However, for some molecules for which line-by-line spectroscopy is unavailable, spectroscopic parameters are derived from cross-section laboratory measurements and made available as pseudo-linelists (for example, the one created by G. C. Toon[15]). The *a priori* state of the atmosphere, which includes profiles of pressure, temperature and volume mixing ratios for different chemical species, is calculated using a climatology from the Whole Atmosphere Community Climate Model (WACCM) over a long period (typically 40 years) (Hannigan et al., 2024). If climatology data is unavailable for certain species, *a priori* profiles can also be obtained from the ERA-Interim and ERA-5 meteorological reanalyses (e.g. water vapour), satellite-based vertical distributions averaged over a specific time period and latitude band (e.g. HFC-134a), or model outputs.

SFIT4 is the most widely used software within the NDACC-IRWG community, although some groups also use the PROFFIT algorithm (e.g. Hase et al., 2004; García et al., 2021). Further details about the specific retrieval strategies designed for this study are presented in Chapters 3 and 4.

[11] National Aeronautics and Space Administration at Langley: `https://www.nasa.gov/langley/`

[12] National Institute of Water and Atmospheric research at Lauder: `https://niwa.co.nz/atmosphere/lauder-atmospheric-research-station`

[13] `https://hitran.org/`

[14] `https://mark4sun.jpl.nasa.gov/specdata.html`

[15] `https://mark4sun.jpl.nasa.gov/pseudo.html`

2.3 Satellite observations

As mentioned in the previous section, corroborating the retrievals is a crucial step. Therefore, total columns obtained from FTIR observations have been compared with satellite data, specifically ACE-FTS satellite observations.

The Atmospheric Chemistry Experiment (ACE)[16] is a Canadian mission controlling the SCISAT-1 satellite that was launched in August 2003 by NASA. Initially, it was designed to take measurements of the Earth's atmosphere for two years, but after twenty years, it has orbited the Earth more than 110,000 times and is still taking daily measurements of atmospheric composition, without significant degradation of the measured quantities. Its long life allows the scientific community to analyse the evolution of the concentration of chlorine-containing molecules, among others, supporting the Montreal Protocol.

SCISAT orbits in a near-polar Low Earth Orbit (LEO), inclined of approximately 74 degrees, at an altitude of 650 km above the Earth's surface. Its orbital period is 97.7 minutes. ACE measures by limb viewing (solar occultation) and records infrared spectra to retrieve the abundances of 46 atmospheric compounds[17] as well as isotopologues and line-of-sight winds. ACE spectra are analysed at the ACE Science Operations Centre (SOC, Chemistry Department, University of Waterloo, Canada), and the final data products are distributed to scientific users around the world.

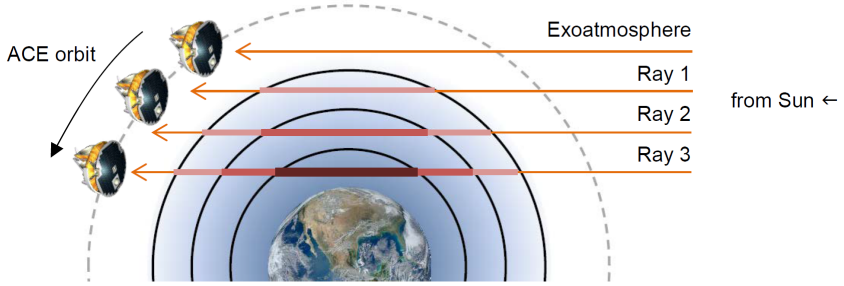

Figure 2.8. Simplified scheme of SCISAT satellite limb viewing (solar occultation) from orbit around the Earth, here for a sunset event. Fig. 1 from Lachance et al. (2013).

Solar occultation measures solar radiance through the planet's atmosphere during sunrise and sunset of the satellite, above the tangent horizon (Figure 2.8). Observation altitudes range from 5 to 150 km. ACE measures solar radiation attenuated by the absorption of atmospheric chemical compounds. Positioned outside the atmosphere at an altitude of 650 km, this technique is particularly sensitive. In addition to atmospheric measurements, ACE records exoatmospheric spectra (above 150 km) as reference data to calibrate the instrument's accuracy and determine the global transmittance of the atmosphere (Lachance et al., 2013).

On board the satellite, there are two instruments: MAESTRO (Measurement of Aerosol Ex-

[16] `https://uwaterloo.ca/atmospheric-chemistry-experiment/`

[17] Atmospheric species retrieved from ACE observations include: C_2H_2, C_2H_6, C_3H_6O, CCl_4, CF_4, CFC-11, CFC-12, CFC-113, CH_3Cl, CH_3CN, CH_3OH, CH_4, ClO, $ClONO_2$, CO, CO_2, $COCl_2$, COClF, COF_2, H_2CO, H_2O, H_2O_2, HCFC-22, HCFC-141b, HCFC-142b, HCl, HCN, HCOOH, HF, HFC-23, HFC-32, HFC-134a, HNO_3, HO_2NO_2, HOCl, N_2, N_2O, N_2O_5, NO, NO_2, O_2, O_3, OCS, PAN, SF_6, SO_2.
From this list, CFC-11 and HFC-134a abundances have been used in this work.

tinction in the Stratosphere and Troposphere Retrieved by Occultation), and ACE-FTS (Fourier Transform Spectrometer), the primary instrument (Figure 2.9). A sun tracker is also on board for accurate pointing during occultations. The **MAESTRO** spectrophotometer covers the 285 – 1030 nm spectral range, with a spectral resolution of about 1 – 2 nm, in order to retrieve vertical profiles of temperature, pressure, ozone, nitrogen dioxide, and aerosols (UWaterloo, 2024). In this work, MAESTRO observations have not been used, unlike ACE-FTS measurements.

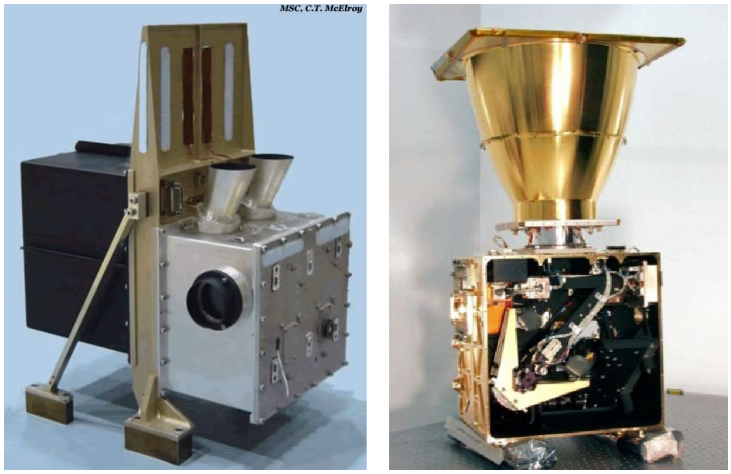

Figure 2.9. MAESTRO spectrophotometer (left) and ACE-FTS spectrometer (right) on board SCISAT (UWaterloo, 2024).

The main goal of the **ACE-FTS** spectrometer is to measure the vertical distribution of atmospheric trace gases. Pressure and temperature profiles are also derived from CO_2 absorption lines. The instrument is a Michelson interferometer and, by Fourier transform spectroscopy, IR solar spectra are obtained in a manner similar to ground-based FTIR spectrometers, but with a different geometry. ACE-FTS measurements are recorded every two seconds, corresponding to a spacing of 2 – 6 km, decreasing at lower altitudes because of refraction effects. The retrievals are interpolated onto a 1 km vertical grid (UWaterloo, 2024). The locations of the occultations are determined by the satellite's orbit and its relative position to the Sun (Harrison et al., 2021).

This instrument operates in the 750 – 4400 cm^{-1} (2300 – 13000 nm) range with a spectral resolution of 0.02 cm^{-1} (Fernando et al., 2019). Spectra are recorded in a limb-viewing geometry and are then inverted to produce vertical profiles of pressure, temperature, and volume mixing ratios (VMRs) of trace gases. The vertical resolution is approximately 3 km from the top of the clouds (or 5 km in clear-sky conditions) up to about 120 km. The field of view (FOV) of the instrument is 1.25 mrad, allowing only a small portion of the solar disk to be observed (Lachance et al., 2013). In this work, Level 2 v4.0 CFC-11 ACE-FTS retrievals (Chapter 3) and Level 2 v5.2 HFC-134a retrievals (Chapter 4) have been used.

2.4 *In situ* surface observations

Another independent dataset used to validate the gas retrievals in this study consists of *in situ* surface measurements conducted within the Advanced Global Atmospheric Gases Experiment (AGAGE) network[18]. This multinational global atmospheric measurement programme is focused on all the important constituents outlined in the Montreal Protocol, as well as the important non-carbon-dioxide species evaluated by the Intergovernmental Panel on Climate Change (IPCC) (Prinn et al., 2018). Today, it is composed of 16 active stations around the world (Figure 2.10; Table B.1). The goals of AGAGE, among others, are:

- To measure the temporal and spatial distributions of anthropogenic gases that contribute to ozone depletion and/or are strong IR absorbers, participating in global warming, such as CFCs and HFCs addressed in this work.
- To measure the global distributions and temporal behaviours to determine the sources and sinks of anthropogenic gases.
- To identify new long-lived atmospheric gases, such as SO_2F_2 and NF_3.
- To determine the global average concentrations and trends of tropospheric OH radicals.
- To estimate the magnitudes and distributions of surface sources (emissions) and sinks of all target compounds.
- To provide data on the global accumulation of these gases to be used by three-dimensional models.

The AGAGE programme was established in 1993 and is still operational. It was preceded by the Atmospheric Lifetime Experiment (ALE) from 1978 to 1981, and by the Global Atmospheric Gases Experiment (GAGE) from 1982 to 1992, ensuring global measurements of greenhouse gases and ozone-depleting substances since 1978. Table 2.4 shows the periods of the three different programmes, as well as the number of stations involved in each one, the instrumentation used, the sampling frequency per day, and the gases monitored in each programme.

Currently, Medusa sample analysis is mainly used in AGAGE primary stations. This system uses gas chromatography with mass spectrometry (GCMS) to measure atmospheric gas concentations, including HFC-134a. The analysis consists of three distinct phases. Firstly, the ambient air inlet on the station tower introduces the air into the instrument, where its water is removed and the analytes are concentrated on a trap by cold adsorption[19]. The sample volume is obtained by an integrating mass flow controller. Secondly, the less volatile analytes and CO_2 stay on the first trap, while CF_4, which is the most volatile analyte, and the other most abundant air gases (N_2, O_2, Ar, and Kr) are transported to another low-temperature trap. Here, they are

[18] `https://www-air.larc.nasa.gov/missions/agage/`

[19] **Adsorption** is the phenomenon where molecules, atoms, or ions from a gas, but also from a liquid or a dissolved solid adhere to a solid or liquid surface. It should not be confounded with "absorption", which implies the penetration into a material.

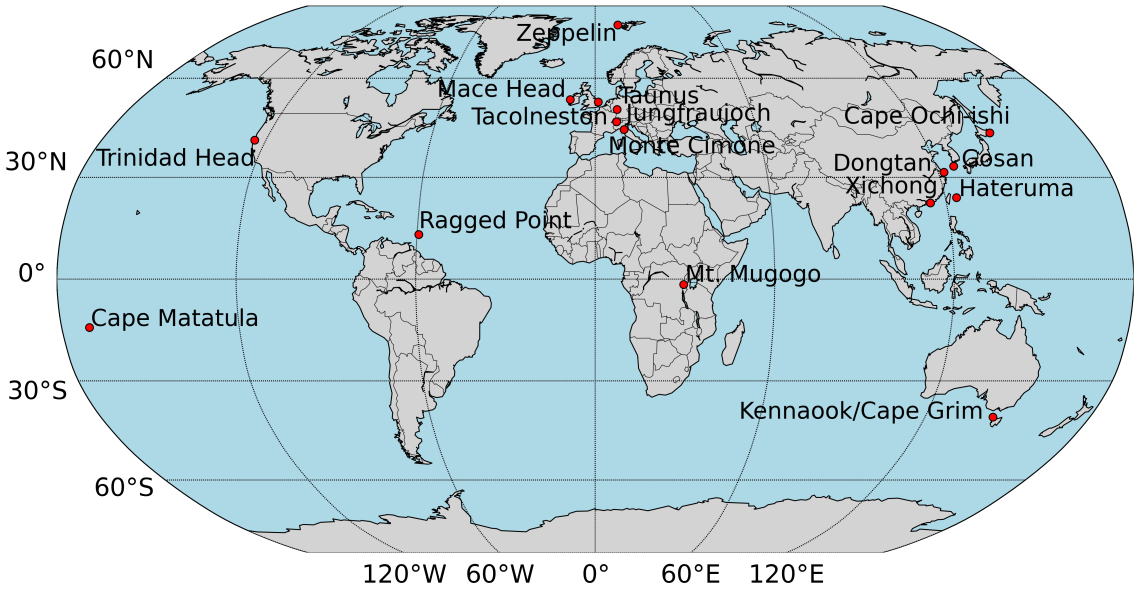

Figure 2.10. Location of the 16 active stations of the AGAGE network. Further information about each station can be found in Table B.1.

Programme	Period	N stations	Instruments	Sampling frequency (times/day)	Gases	Reference
ALE	1978 – 1981	4	GC-ECDs	4	CFC-11, CFC-12, CCl_4, N_2O, CH_3CCl_3	Prinn et al. (1983)
GAGE	1982 – 1992	5	GC-ECDs GC-FIDs	12	Added CFC-113, $CHCl_3$, and CH_4	Prinn et al. (2000)
AGAGE	1993 – now	16	GC-HgORDs GC-MSDs	36 20	Added H_2 and CO Added 50 trace gases	Prinn et al. (2018)

Table 2.4. Periods, number of stations, intrumentation used, sampling frequencies, and monitored atmospheric gases for the ALE, GAGE, and AGAGE programmes from 1978 to the present. The acronyms of the instrumentation correspond to: gas chromatographs with electron-capture detectors (GC-ECDs), gas chromatographs with flame-ionization detectors (GC-FIDs), gas chromatographs with mercuric oxide reduction detectors (GC-HgORDs), and gas chromatographs with mass spectrometric detectors (GC-MSDs).

separated by desorption[20] and transferred to the main column for mass spectrometry detection. In the final phase, the gases that remained on the first trap are desorbed into the main column, where they are separated and transported to mass spectrometry detection (Miller et al., 2008).

The AGAGE programme measures atmospheric gas trends globally and at high frequency, helping with emissions estimation. This programme, along with the NDACC network, plays a key role in monitoring the atmospheric concentrations of important species included in the Montreal Protocol and evaluated by the IPCC.

[20]**Desorption** is the reverse process of adsorption. Here, adsorbed molecules, atoms, or ions separate from the surface and return to the surrounding fluid phase.

2.5 Model simulations

Atmospheric transport and chemistry models are widely used by the scientific community to study and understand atmospheric composition. These models can be classified into two main groups:

- **General circulation models (GCMs):** they estimate winds and temperatures independently.
- **Chemical transport models (CTMs):** these are off-line models that rely on meteorological fields because they do not calculate their own winds and temperatures. The meteorological fields can be generated by a GCM or obtained from reanalysis data. Consequently, CTMs are computationally less demanding than GCMs and can use realistic meteorological conditions when the fields are derived from analyses, which is favourable for comparisons with observations (Chipperfield, 2006).

The TOMCAT/SLIMCAT three-dimensional off-line CTM was used in this study to interpret the retrievals of the molecules CFC-11 and HFC-134a. Initially, TOMCAT was developed to investigate the evolution of trace gases in the Arctic lower stratosphere (Chipperfield et al., 1993). However, the TOMCAT team soon realised that their model was not optimal for stratospheric studies. This led to the development of the SLIMCAT model, which was first presented in Chipperfield et al. (1996) and used to study the decrease of ClO and the evolution of other atmospheric species within the Antarctic polar vortex.

TOMCAT was later adapted to be primarily forced by meteorological (re)analyses from the European Centre for Medium-range Weather Forecasts (ECMWF). As a result, TOMCAT evolved into a tropospheric CTM, while SLIMCAT became a stratospheric CTM. Subsequently, both models were combined into a single model that allowed to study atmospheric chemistry, aerosols, and transport using an adaptable vertical coordinate system extending from the surface (Chipperfield, 2006).

The combined TOMCAT/SLIMCAT model employs a global Eulerian grid covering from pole to pole. The vertical extent of the model is defined by the limitations of the analyses or GCM calculations used to force it. While the longitudinal grid spacing is uniform, the latitudinal spacing can vary. The vertical coordinate system is adaptable, offering two modes: (1) the TOMCAT mode, which is based on terrain-following levels combined with pressure levels; and (2) the SLIMCAT mode, based on terrain-following levels combined with potential temperature levels (isentropic vertical coordinates).

Further details on the TOMCAT/SLIMCAT model can be found in Chipperfield (2006). The specific configurations used for each molecule in this study are described in Chapters 3 and 4.

2.6 Trend analysis

The analysis of long-term time series provides the understanding of the evolution of atmospheric constituents and, consequently, of the Earth's climate. Estimating trends and investigating potential changes are crucial for enhancing this insight. In Chapters 3 and 4, the trend estimations for both atmospheric species analysed in this study, CFC-11 and HFC-134a, are presented. The Auto-regressive Wild Bootstrap (AWB) method, described in Friedrich et al. (2020b), was employed for this purpose. This method, initially developed for econometrics research, was later used to analyse ethane time series (Friedrich et al., 2020a).

Atmospheric time series are often characterised by missing observations due to instrument issues or unfavourable observation conditions, as well as challenges like autocorrelation[21], heteroskedasticity[22], and seasonal variations. For FTIR measurements, these challenges are particularly prominent since observations require clear-sky conditions, leading to significant data gaps.

Given that this study focuses on the evolution of atmospheric gas concentrations, the aim is to determine whether these concentrations increase, decrease, or exhibit changes in their temporal trends, and whether they are statistically significant. The AWB method accounts for these challenges and provides reliable trend estimations (Friedrich et al., 2020b).

Figure 2.11 shows two different approaches: a **linear trend model** that allows for a break point, estimated by the model, and includes the determination of a reliable confidence interval; and a **smoothly varying trend model**, that captures gradual changes over time.

2.6.1 The broken trend model

In this model, we consider a linear trend that allows a change, or break, in its slope. The break ensures continuity, meaning no "jump" occurs between the two slopes (Friedrich et al., 2019).

We consider a classical linear regression, with an additional term to account for the change in slope:

$$y_t = g_t + \delta D_{t,T_1} + F_t + u_t; \quad \text{for } t = 1, ..., T \tag{2.27}$$

where y_t represents the studied time series; $g_t = \alpha + \beta t$ is the linear function with slope β and intercept α; u_t is an error term; $\delta D_{t,T_1}$ is a variable which causes a change in the slope coefficient from β to $(\beta + \delta)$ after the break point time, T_1:

$$D_{t,T_1} = \begin{cases} 0 & \text{if } t \leq T_1 \\ t - T_1 & \text{if } t > T_1 \end{cases} \tag{2.28}$$

[21] **Autocorrelation** refers to the correlation between the current values of a variable and its past values in a time series.

[22] **Heteroskedasticity** describes a condition in which the variability of residuals changes over time in a time series.

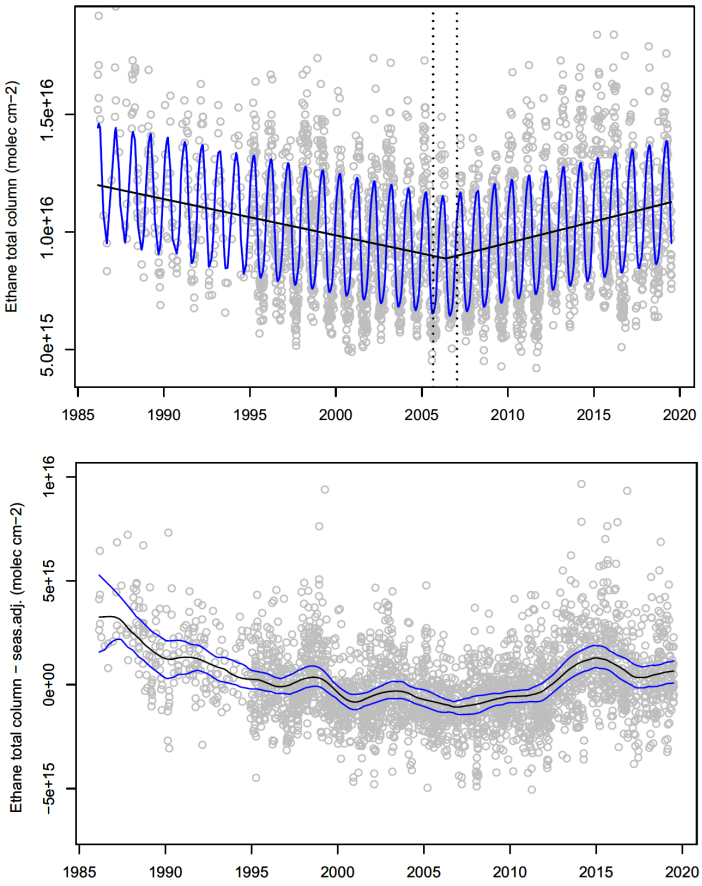

Figure 2.11. Example of a broken trend (top) and a nonparametric trend (bottom) functions. In grey, daily ethane columns above the Jungfraujoch station are displayed for the period between 1986 and 2019 (seasonally adjusted in the bottom panel). The estimated trends are shown in black. In the top panel, the fitted Fourier series is represented in blue, with the 95% confidence interval for the estimated break date (2006) indicated by the vertical dotted lines. In the bottom panel, the blue curves illustrate the 95% confidence interval. Adapted from Fig. 1 and Fig. 3 from Friedrich et al. (2020a).

Finally, F_t represents the intra-annual seasonality and is expressed in Fourier terms:

$$F_t = \sum_{i=1}^{N} a_i \cos(2i\pi t) + b_i \sin(2i\pi t) \tag{2.29}$$

The variability of the time series is typically well captured using three terms (N = 3) of the Fourier series (Gardiner et al., 2008). The problem then focuses on estimating the parameters α, β, and δ.

To address the issue of missing measurements, as described earlier, a binary variable is defined to represent the missing data pattern:

$$M_t = \begin{cases} 0 & \text{if } y_t \text{ is missing} \\ 1 & \text{if } y_t \text{ is observed} \end{cases} \quad \text{for } t = 1, ..., T \tag{2.30}$$

where y_t represents the different observations (Friedrich et al., 2019).

First, the break date must be estimated. Given a candidate break point T_c, the values of α, β, δ, and F_t are predicted using a least-squares regression, which allows to determine the parameters of the model that best fit the observed data:

$$\left(\hat{\alpha},\hat{\beta},\hat{\delta},\hat{F}_t\right)_{T_c} = \underset{\alpha,\beta,\delta,F_t}{\operatorname{argmin}} \sum_{t=1}^{T} M_t \left[y_t - \left(\alpha+\beta t+\delta D_{t,T_c}+F_t\right)\right]^2 \tag{2.31}$$

Let Λ be a subset of possible break dates. For each candidate break date T_c, a least-squares regression is performed, and the minimum value across all candidates provides the estimated break date $\hat{T}_1$ (Friedrich et al., 2019).

$$\hat{T}_1 = \underset{T_c\in\Lambda}{\operatorname{argmin}} \sum_{t=1}^{T} M_t \left[y_t - \left(\hat{\alpha}+\hat{\beta}t+\hat{\delta}D_{t,T_c}+\hat{F}_t\right)_{T_c}\right]^2 \tag{2.32}$$

where $\left(\hat{\alpha},\hat{\beta},\hat{\delta},\hat{F}_t\right)_{T_c}$ are obtained as described in Eq. 2.31. When the break date $\hat{T}_1$ is estimated, the subsequent parameters $\left(\hat{\alpha},\hat{\beta},\hat{\delta},\hat{F}_t\right)_{\hat{T}_1}$ can be calculated (Friedrich et al., 2019).

This method can determine whether a break point exists in the time series or if it follows a simple linear trend, thanks to the variable D_{t,T_1} defined in Eq. 2.28. The broken trend model was able to identify a break point in the CFC-11 time series above Jungfraujoch around 2011, as discussed in Chapter 3 (Pardo Cantos et al., 2022). The classical linear trend model was used to estimate the increase of HFC-134a, as shown in Chapter 4 (Pardo Cantos et al., 2024).

To evaluate the significance of the estimations, a measure of uncertainty must be provided. As described by Friedrich et al. (2019, 2020b), two main issues arise with this type of time series: (1) the correlation of residuals from the predicted model, and (2) the unequal spacing of observations over time.

To address these challenges, a bootstrap method, specifically the Autoregressive Wild Bootstrap, is proposed. Additionally, the AWB method is robust against heteroskedasticity. In contrast, the standard bootstrap method, as in Gardiner et al. (2008), operates randomly and does not account for serial dependence or time-varying heteroskedasticity. As a result, the bootstrap sample would not accurately replicate the original time series of residuals. The goal of the AWB method is to create uncertainties that reflect the same pattern of missing data, correlation, and variance changes as the true residuals (Friedrich et al., 2020b).

From the model described by Eq. 2.27, if we impose a break point at time $\hat{T}_1$:

$$\hat{u}_t = M_t \left[y_t - \left(\hat{\alpha}+\hat{\beta}t+\hat{\delta}D_{t,\hat{T}_1}+\hat{F}_t\right)\right];\ \text{for}\ t=1,...,T \tag{2.33}$$

Then, the bootstrap sample will be:

$$y_t^* = M_t \left(\hat{\alpha}+\hat{\beta}t+\hat{\delta}D_{t,\hat{T}_1}+\hat{F}_t+u_t^*\right) \tag{2.34}$$

where u_t^* are the bootstrap errors. The value $\hat{T}_1^*$ will be estimated from y_t^*, as explained in Eq. 2.32. A bootstrap distribution of $\hat{T}_1^*$ will be obtained by repeating the steps described

above (Friedrich et al., 2019).

2.6.2 The nonparametric trend model

The previous model imposed a linear trend, which may hide some of the underlying information in the actual form of the time series. For this reason, Friedrich et al. (2019, 2020b) proposed an alternative trend model based on smooth functions, where no specific form or mathematical function of the trend is predefined.

Let the following model describe a nonparametric trend:

$$y_t = g(t/T) + F_t + u_t; \quad \text{for } t = 1, ..., T \tag{2.35}$$

where F_t is the Fourier terms function to account for the seasonality of the time series (Eq. 2.29), and u_t is the error term, as in the previous model. The function $g(\cdot)$ determines the shape of the trend. This trend function is considered smooth because it is twice continuously differentiable with bounded derivatives.

The method is divided into two steps: (1) the seasonality of the time series is removed, and (2) the nonparametric trend function is estimated.

Although this model was used during the testing and analysis phase, it is not included in the results of this study; therefore, the mathematical details are not explained here. Further information on the estimation of this smooth trend model can be found in Friedrich et al. (2019, 2020b).

Chapter 3

Determination and analysis of time series of CFC-11 from ground-based FTIR solar absorption spectra

Numbered sections of this chapter follow:

Pardo Cantos, I., Mahieu, E., Chipperfield, M. P., Smale, D., Hannigan, J. W., Friedrich, M., Fraser, P., Krummel, P., Prignon, M., Makkor, J., Servais, C., and Robinson, J. (2022). Determination and analysis of time series of CFC-11 (CCl_3F) from FTIR solar spectra, *in situ* observations, and model data in the past 20 years above Jungfraujoch (46°N), Lauder (45°S), and Cape Grim (40°S) stations. *Environmental Science: Atmospheres*, 2(6), 1487-1501. https://doi.org/10.1039/d2ea00060a.

Abstract. The atmospheric concentration of CFC-11 (CCl_3F) has declined in response to the phase-out of its production by the Montreal Protocol. Nevertheless, this atmospheric concentration decline suffered a slowdown around 2012 due to emissions from non-reported production. Since CFC-11 is one of the most important ozone-depleting chlorofluorocarbons (CFCs), its continuous monitoring is essential. We present the CFC-11 total column time series (2000 – 2020) retrieved in a consistent way from ground-based high-resolution solar absorption Fourier Transform Infrared (FTIR) spectra. These observations were recorded at two remote stations of the Network for the Detection of Atmospheric Composition Change (NDACC): the Jungfraujoch station (Northern Hemisphere) and the Lauder station (Southern Hemisphere). These time series are new. They were produced using improved line parameters and merged considering the instrument changes and setup modifications. Afterwards, they were compared with Cape Grim station *in situ* surface observations conducted within the Advanced Global Atmospheric Gases Experiment (AGAGE) network and with total column datasets calculated by the TOMCAT/SLIMCAT 3-D chemical transport model. Trend analyses were performed, using an advanced statistical tool, in order to identify the timing and magnitude of the trend change in both hemispheres. The observations are consistent with the model results and confirm the slowdown in the CFC-11 atmospheric concentration decay, since $\approx$ 2011 in the Northern Hemisphere, and since $\approx$ 2014 in the Southern Hemisphere.

3.1 Introduction

Trichlorofluoromethane (CFC-11) is one of the most important chlorofluorocarbons (CFCs) emitted into the atmosphere. CFCs are chemicals exclusively produced by human activities and they were used as aerosol spray propellants, refrigerants, inflating and insulating agents in the production of foam materials, and solvents (Fleming et al., 2020). CFC-11 is transported into the stratosphere where it is photodissociated by ultraviolet (UV) radiation, releasing chlorine atoms that catalytically destroy stratospheric ozone (Molina and Rowland, 1974). Therefore, CFC-11 has substantially contributed to the buildup of organic and inorganic chlorine, and subsequently the stratospheric ozone depletion, which was first reported by Farman et al. (1985). Its mean atmospheric lifetime is 52 years (uncertainty range of 43 – 67 years) (Chipperfield et al., 2021), and residual banks will continue emitting CFC-11 for some decades before complete removal from the atmosphere can be expected (Lickley et al., 2020). Thus, this molecule is an important target to monitor at present even though its emissions have decreased noticeably in response to production phase-down measures introduced by the Montreal Protocol on Substances that Deplete the Ozone Layer (1987) and its subsequent amendments and adjustments (WMO, 2018).

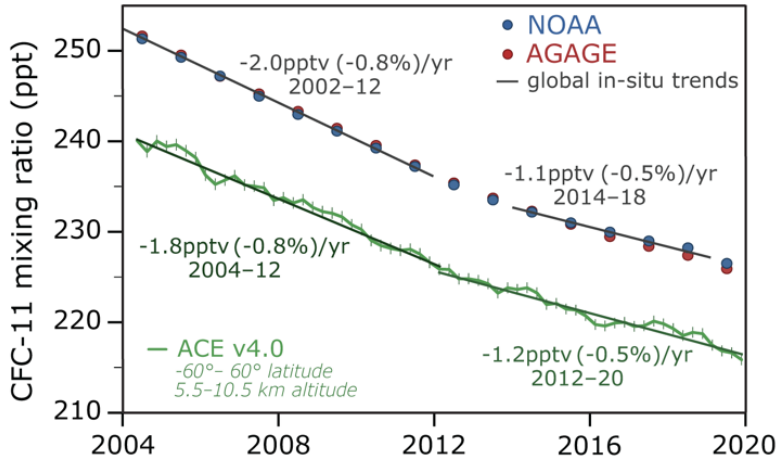

Figure 3.1. CFC-11 global mixing ratio and trends from the ACE-FTS instrument (60°N – 60°S) in green (4-months means) and from *in situ* measurements (annual means): NOAA in blue, and AGAGE in red. Figure 2.2(b) from the Report on the Unexpected Emissions of CFC-11, 2021 (Chipperfield et al., 2021).

Due to the Montreal Protocol, the tropospheric concentrations of CFC-11 reached a maximum around 1994 and decreased afterwards (WMO, 2018). Although it was decided to almost completely phase out CFC production by 2010, Montzka et al. (2018) reported that the decrease in atmospheric CFC-11 concentrations suffered a slowdown since 2012 in both hemispheres, due to an unexpected increase of its emissions, evaluated at (13 ± 5) Gg yr^{-1} since 2012. Emissions from this illegal CFC-11 production are mainly coming from eastern China, as reported by Rigby et al. (2019). The Atmospheric Chemistry Experiment (ACE) satellite measurements have shown that the tropospheric rate of decrease, between 60°S and 60°N, has changed from (-1.81 ± 0.05) ppt/year (2004 – 2012) to (-1.16 ± 0.04) ppt/year (2012 – 2020) (Bernath et al., 2020) (see green line in Figure 3.1). Consequently, this slowdown in the decrease of CFC-11 atmospheric concentrations is expected to produce a delay in ozone recovery (Dhomse et al.,

2019). Fortunately, Montzka et al. (2021) and Park et al. (2021) have reported a return to reduced emission rates levels, similar to that during 2008 – 2012 since 2018.

In this work, we analyse the CFC-11 abundances above the Jungfraujoch and Lauder stations along with ground level *in situ* concentrations from Cape Grim. Here, the Lauder total column CFC-11 decadal datasets were analysed for the first time and, in order to better characterise the CFC-11 decadal trend at Jungfraujoch, the time series was harmonised and updated, improving the datasets presented in previous assessments (WMO, 2018; Chipperfield et al., 2021). We focus on the period from January 2000 to December 2020 to analyse the influence in Europe, and Southern Hemisphere mid-latitudes, of the emissions related to the new, illegal production. In order to do so, we compare the FTIR total columns with TOMCAT/SLIMCAT chemical transport model data for three different simulations of differing CFC-11 emission rates. In Section 3.2, we describe the FTIR and the *in situ* observations, and the 3-D chemical transport model. In Sections 3.3 and 3.4, we present the FTIR CFC-11 retrieval strategy, then we show the results of the trend analyses, for the Jungfraujoch (Northern Hemisphere, NH) and the Lauder and Cape Grim (Southern Hemisphere, SH) stations, as well as the respective model trend analyses. Finally, we present the conclusions of our study in Section 3.5.

3.2 Measurement methods and datasets

In this study, we used data from three mid-latitude stations, Jungfraujoch at 46.55°N, Lauder at 45.04°S, and Cape Grim at 40.68°S. The Jungfraujoch and Lauder FTIR measurements are taken under the auspices of the Network for the Detection of Atmospheric Composition Change (NDACC) (De Mazière et al., 2018), and the Cape Grim *in situ* sampling are conducted within the framework of the Advanced Global Atmospheric Gases Experiment (AGAGE) global network (Prinn et al., 2018).

3.2.1 The Jungfraujoch station FTIR observations

The High Altitude Research Station Jungfraujoch (46.55°N, 7.98°E) is located on the Northern Swiss Alps, on a saddle between the Mönch and the Jungfrau summits, at 3580 m above mean sea level (a.m.s.l.), thus the station is most of the time in free troposphere conditions (Prignon et al., 2019).

The Institute of Astrophysics of the University of Liège has collected infrared (IR) solar spectra at that site since the early 1950s. Firstly, grating spectrometers were used and then two Fourier-Transform Infrared (FTIR) spectrometers have run since the mid-1980s, a homemade instrument (from 1984 to 2008), and a commercial Bruker IFS-120HR spectrometer (from the beginning of the 1990s to present). The optical filters and the HgCdTe (mercury cadmium telluride, MCT) or InSb (indium antimonide) cooled detectors allow to cover the mid-IR spectral range. See Zander et al. (2008) for more information about the instrumentation. The IR solar absorption spectra used in this study were recorded by the homemade and the Bruker instruments, with a HgCdTe detector, under clear-sky conditions. These spectra cover the 700 – 1400 cm^{-1} range with a spectral resolution of 0.0061 cm^{-1}, what corresponds to a maximum optical path difference (OPD) of 82 cm. The mean signal-to-noise ratio (SNR) of the studied

period (2000 – 2020) is 945.

3.2.2 The Lauder station FTIR observations

Like Jungfraujoch, the Lauder Atmospheric Research Station (45.04°S, 169.68°E, 370 m a.m.s.l.) was a founding site of NDACC. Mid-IR FTIR measurements started at Lauder in the early 1990s and continue to the present day. The spectral observations used in this study were recorded with a Bruker IFS-120HR (2000 – 2018) and a Bruker IFS-125HR (2018 – 2020). In both instruments, solar spectra (covering the region 700 – 4000 cm^{-1}) are taken on days with cloud-free line of sight to the Sun using solar trackers with active tracking (Robinson et al., 2020). Solar spectra used in the retrieval of CFC-11 were taken with a MCT detector through a mid-IR bandwidth filter 700 – 1400 cm^{-1}, at a spectral resolution of 0.0035 cm^{-1} using a KBr beamsplitter. Such spectra are also used in the analysis of other trace gases species, such as O_3 (Vigouroux et al., 2015), HNO_3 (Ronsmans et al., 2016), and $ClONO_2$ (Kohlhepp et al., 2012). Instrument line shape and alignment are monitored monthly using low pressure HBr and N_2O cells (Hase et al., 1999; Hase, 2012).

3.2.3 The Cape Grim station *in situ* observations

In situ observations of CFC-11 commenced at Cape Grim, Tasmania (40.7°S, 144.7°E), in 1976 and have continued uninterrupted until the present day (Fraser et al., 1983, 2018). The station, operated by the Australian Bureau of Meteorology, sits atop a 90 m cliff on Tasmania's west coast and the ambient air is sampled 36 times per day from a tower at 70 m above the station. The Cape Grim CFC-11 baseline monthly mean data (2001 – 2020) reported in this paper are obtained from CSIRO's participation in the global AGAGE programme (Prinn et al., 2018). The data were obtained from a gas chromatographic (GC) instrument incorporating an electron capture detector (ECD) and are calibrated in the Scripps Institution for Oceanography (SIO-05) scale. Baseline data are selected using a statistically-based algorithm, and are free of the influence of regional CFC-11 emissions and represent mid-latitude, background CFC-11 mixing ratios for the Southern Hemisphere (Prinn et al., 2018).

3.2.4 TOMCAT/SLIMCAT chemical transport model

TOMCAT/SLIMCAT (hereafter TOMCAT) is a global 3-D off-line chemical transport model (Chipperfield, 2006). It is used to study a range of chemistry-aerosol-transport issues in the troposphere and stratosphere. The model is usually forced by European Centre for Medium-range Weather Forecasts (ECMWF) meteorological (re)analyses, although General Circulation Model (GCM) output can also be used. When using ECMWF fields, as in the experiments described here, the model reads in the 6-hourly fields of temperature, humidity, vorticity, divergence and surface pressure. The resolved vertical motion is calculated online from the vorticity. For the simulations used in this study, the model was run at horizontal resolution of $2.8^\circ \times 2.8^\circ$ with 60 hybrid σ-pressure levels from the surface to ≈ 60 km. The model was run from 1980 to 2020 and forced by ECMWF ERA5 reanalyses (Hersbach et al., 2020). Convective mass fluxes were calculated online using the scheme of Tiedtke (1989) and mixing in the boundary layer

is based on the scheme of Holtslag and Boville (1993). The model simulations included three idealised CFC-11 tracers, as used in Montzka et al. (2021). The simulation parameterised the atmospheric loss of the CFC-11 tracers using calculated photolysis rates and a repeating year of archived monthly mean zonal mean O(^{1}D) distributions from a previous full chemistry simulation. Tracer A used the best estimate of historic CFC-11 emissions with realistic distribution at the surface (Montzka et al., 2021). Tracer B used the same total time-dependent emissions as Tracer A but they were distributed uniformly over the Earth's surface. Tracer C assumed zero CFC-11 emissions after 2000.

3.3 CFC-11 vertical column retrieval

3.3.1 Retrieval strategy

At both, Jungfraujoch (JFJ) and Lauder (LAU), column retrievals were performed with the SFIT4 v0.9.4.4. algorithm which implements the Optimal Estimation Method (OEM) of Rodgers (2000). For the Jungfraujoch station, the layer scheme contained 41 layers from 3.58 km to 120 km, whereas the Lauder station layering scheme spanned 47 layers from 0.37 km to 120 km. In both schemes, the thicknesses gradually increased from 0.65 km (JFJ) and 0.43 km (LAU) for the lowermost layer up to 14 km for the top one.

Since the CFC-11 has a very broad but relatively unstructured absorption in the infrared spectral range, the retrieval spectral window has to be relatively large to encompass the whole feature. Furthermore, it has to be carefully optimised in order to limit the interference by other molecules. The optimal spectral window for CFC-11 was first defined by Zander et al. (1983) as 825 – 860 cm^{-1}. For this study, it was adjusted to 830.0 – 859.3 cm^{-1} in order to avoid a H_2O absorption line at $\approx$ 859.5 cm^{-1}; and only the observations with an apparent solar zenith angle (SZA) between 60° and 85° (JFJ), and between 60° and 89° (LAU) were fitted such as to maximise the CFC-11 absorption depth and information content.

The interfering telluric species used in this retrieval strategy were H_2O, CO_2, O_3, OCS, HNO_3, $COCl_2$, and $H_2{}^{18}O$, and their spectroscopic parameters were taken from the HITRAN2008 and HITRAN2012 (Rothman et al., 2009, 2013) molecular spectroscopic databases, the ATM2019 molecular spectroscopic database (`https://mark4sun.jpl.nasa.gov/specdata.html`) or the empirical pseudo-linelist (PLL) created by G.C. Toon (`https://mark4sun.jpl.nasa.gov/pseudo.html`). PLLs are appropriate to model unresolved features, as those of CFC-11 and $COCl_2$. Solar lines were obtained from the empirical model proposed by Hase et al. (2006). At Lauder, spectral channeling of $\approx$ 0.1% amplitude (caused by filter etalon) was also fitted.

We adopted an OEM regularisation since it allowed to retrieve more information compared to a Tikhonov-type regularisation. The diagonal elements of the *a priori* covariance matrix, S_a, were set to 15% per km. For the off-diagonal terms, we took an interlayer correlation half-height half-width (of exponential-shape correlation) of 4 km. The signal-to-noise ratio for the inversions was established to 100 for JFJ and 180 for LAU.

At JFJ and LAU, *a priori* CFC-11 and all interfering species profiles were calculated from a climatology of the Whole Atmosphere Community Climate Model (WACCM, version 4,

Marsh et al., 2013) simulations for the 1980 – 2020 period, except for water vapour at JFJ. *A priori* water vapour profiles for JFJ were provided by the ERA-Interim (Berrisford et al., 2011) meteorological reanalyses extrapolated for the top of the atmosphere using WACCM monthly means (2000 – 2019). Since the ERA-Interim reanalysis is only available until August 2019, we used the reanalyses from the National Centers for Environmental Prediction (NCEP) (Kalnay et al., 1996) for the final period. Atmospheric pressure and temperature profiles were also supplied by NCEP.

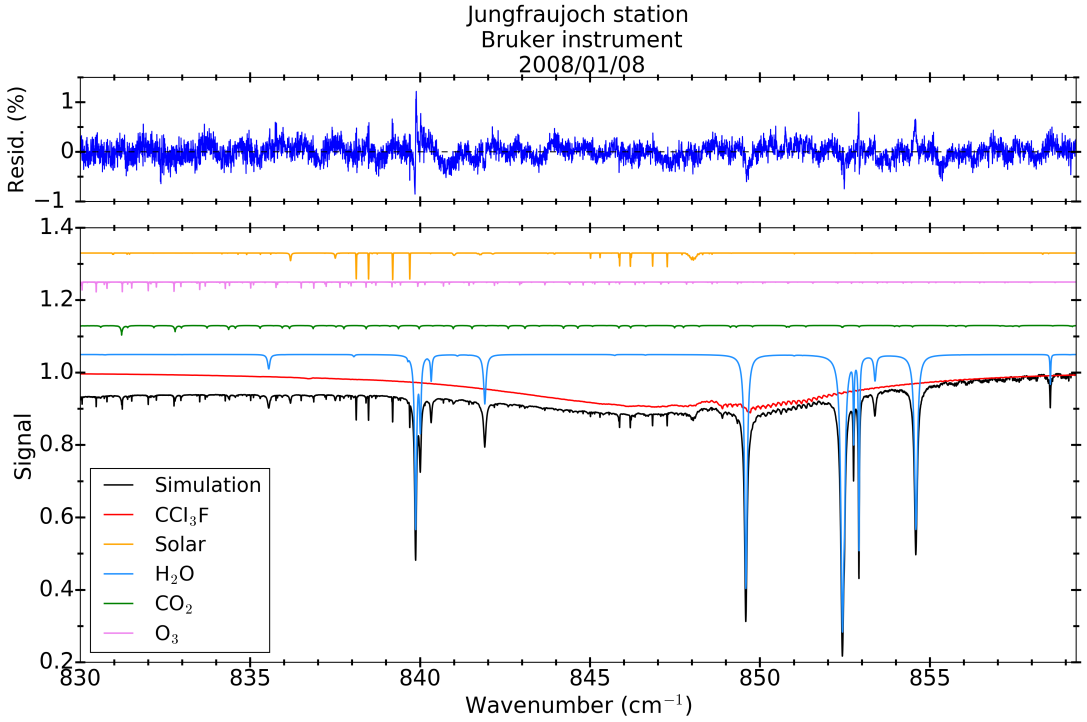

Figure 3.2. Simulations of the 830.0 – 859.3 cm^{-1} spectral window from spectra recorded by the Bruker IFS-120HR FTIR instrument at Jungfraujoch station with an apparent solar zenith angle of 80.3°, and a maximum optical path difference of 82 cm. The root-mean-square of the fitting residuals (RMS) is 0.20%. The main interfering species (H_2O, CO_2, and O_3) and the solar spectra are shifted vertically for clarity. Second-order absorbers are not shown. The top panel displays the observed-calculated residuals, in %, from the fit to the spectrum recorded on 8th January 2008.

Figure 3.2 shows the synthetic spectra produced by the SFIT4 algorithm for CFC-11 and the main interfering species at the selected spectral window for the Jungfraujoch station. The top panel displays residuals (%) from the fit to a spectrum recorded on 8th January 2008. The bottom panel shows the simulated spectrum (black line) and the per-species spectra for our target and the main absorbers in this range (H_2O, CO_2, and O_3) as well as the solar spectrum. Note that the interfering species and solar spectra are offset vertically for clarity. A good fit is obtained in this wide spectral range, with residuals close to the noise level, except near some of the strongest water vapour lines. It is worth noting that this good agreement is representative of the whole Jungfraujoch fitting residuals since the root mean square of the fitting residuals (RMS) for this example is 0.20%, the median RMS for the entire time series is 0.23%, and the mean RMS is (0.25 ± 0.07)%.

3.3.2 Error budget and information content of measurements

Table 3.1 shows the main sources of error (measurement, temperature, interfering species, etc.) affecting the retrieval of Jungfraujoch and Lauder CFC-11 total columns, calculated for one year (2008 and 2016, respectively) of observations. Every error includes both a systematic and a random component. As described in Eq. 8 of Zhou et al. (2016) the total error contains four different parts: the smoothing error, the forward model error, the measurement error, and the forward model parameter error.

To calculate the smoothing error (Eq. 3.16 of Rodgers, 2000), we produced the random component of the error covariance S_b matrix by calculating the relative standard deviation in version 4.0 Level 2 CFC-11 ACE-FTS (Boone et al., 2019) retrievals, for each level of the grid (14.5 – 22.5 km between 40 and 50°N), for the 02/2004 – 02/2020 period. The S_b matrix systematic part was created using the mean relative difference of CFC-11 retrievals between ACE-FTS and MIPAS Level 2 Version 8.22 (Dinelli et al., 2021) for each layer (from 05/2005 to 04/2012). The CFC-11 profile correlation width was set to 4 km. For the solar zenith angle at the JFJ station, the random uncertainty was assumed as $\pm 0.15^\circ$ and the systematic uncertainty as $\pm 0.1^\circ$. For the Lauder station, all SZA uncertainty was assumed random. According to the empirical PLL, the relative systematic uncertainties of CFC-11 spectroscopic parameters were set to 7%.

	Relative uncertainty (%)		
Error type and source	**JFJ**	**LAU**	**Notes**
Random components			
Measurement	0.9	0.7	
Temperature	2.7	2.0	
SZA	1.16	0.15	Assuming $\pm 0.15^\circ$ for solar pointing (JFJ) and 0.025° half diameter at max (LAU)
Zero-level offset (zshift)	1.1	0.01	
Interfering species	0.13	0.05	
Smoothing	0.4	0.4	
Retrieval parameters	0.02	0.01	
Total random	**3.3**	**2.2**	
Systematic components			
CFC-11 line intensity	7	7.1	Assuming 7% from pseudo-linelist
Temperature	2.11	0.34	
SZA	0.8	0.0	Assuming $\pm 0.10^\circ$ for solar pointing (JFJ); all SZA is assumed random (LAU)
Zero-level offset (zshift)	1.1	0.0	All zshift is assumed random (LAU)
Retrieved interfering species (i.e. H_2O) line intensity	0.02	0.01	
Total systematic	**7.5**	**7.2**	

Table 3.1. Mean relative errors (%) that concern the total column retrievals of CFC-11 for the Jungfraujoch (JFJ) and Lauder (LAU) stations.

The total random errors are 3.3% and 2.2%, for the Junfraujoch and Lauder stations respectively, and they are mostly influenced by the temperature profile uncertainties. The total systematic errors are 7.5% and 7.2%, for the Junfraujoch and Lauder stations respectively, and they are dominated by the uncertainty in the spectroscopic parameters on the intensities of

the pseudo-lines fitted to the cross-section laboratory spectra, and in the temperature profile uncertainty. Uncertainties agree with those obtained by Zhou et al. (2016) (Reunion Island) and Polyakov et al. (2021) (St. Petersburg). The other sources of uncertainty (random and systematic) only contribute to the total error at 1% (i.e. zshift) or less (i.e. interfering species).

In order to evaluate the information content of the retrieval processing, the mean averaging kernels were analysed. The averaging kernel matrix (A) described in the Rodgers (2000) formalism characterises the contribution of the *a priori* (x_a) and the true (x) vertical distributions to the retrieved vertical profile ($\hat{x}$). According to Eq. 3.12 of Rodgers (2000):

$$\hat{x} = x_a + A(x - x_a) + G_y e_y \tag{3.1}$$

where $G_y e_y$ is the error in the retrieval originated by the total measurement error (retrieval error).

Figure 3.3 shows the mean layer averaging kernels (left) and eigenvectors (right) derived from the retrievals of the 2004 – 2006 spectra in the case of Jungfraujoch (panels (a) and (b)) and the 2017 – 2020 spectra for Lauder (panels (c) and (d)). The coloured lines in the averaging kernel plots show the different individual layer averaging kernels, and the black line shows the total column averaging kernel (scaled by 0.1), from the site altitude (3.58 km for Jungfraujoch and 0.37 km for Lauder) up to 40 km.

The degrees of freedom for signal (DOFS) is a measure of independent information in the retrieved profile and is defined as the trace of the averaging kernel matrix (Tr(A)) or the sum of eigenvalues (Rodgers, 2000). For Jungfraujoch, mean DOFS is 1.36, meaning that one piece of information can be obtained from the retrievals. The first eigenvalue indicates that 99% of the information characterising the troposphere comes from the retrieval, and not from the adopted *a priori* profile. As to the second eigenvalue, it amounts on average to 0.35, preventing the determination of two independent pieces of information, or partial columns, above and below about 8 km. However, the second eigenvector still allows to improve height resolution. Concerning Lauder results, the DOFS is 1.57 and the first eigenvalue is 1.00, indicating that 100% of the information describing the troposphere is coming from the retrievals. The second eigenvalue, equal to 0.56, shows that two columns (tropospheric and lower-stratospheric) can be separated at 5.3 km with almost 60% of the information coming from the retrievals.

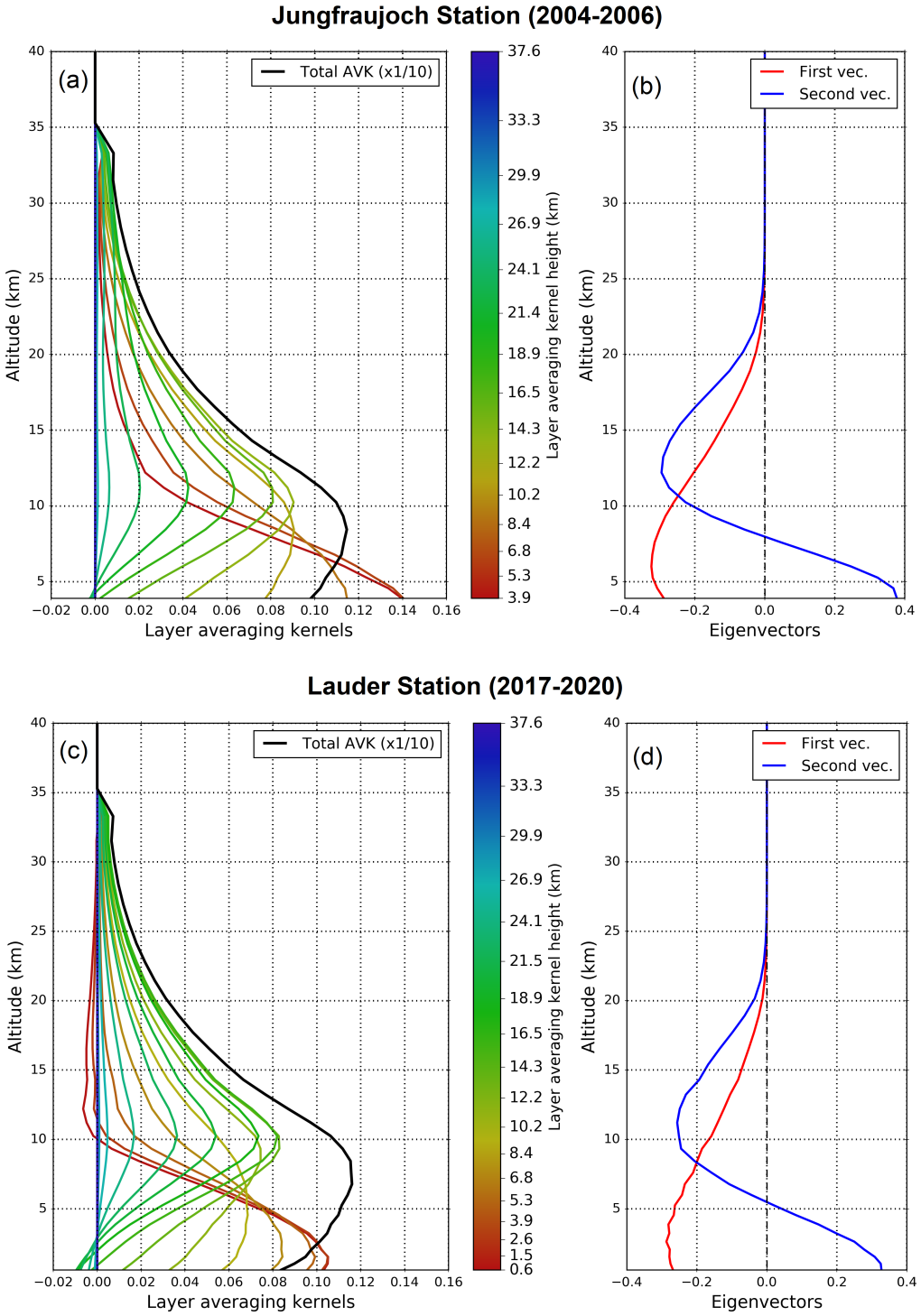

Figure 3.3. (a) Mean layer averaging kernels for mixing ratios computed for the spectra recorded (a) from January 2004 to December 2006 above Jungfraujoch and (c) from November 2017 to December 2020 above Lauder. The ticks on the colour bar are the individual layer averaging kernels represented in the plots. Eigenvectors are shown in (b) for Jungfraujoch and in (d) for Lauder. The two first eigenvalues are (b) 0.99 and 0.35, respectively, and (d) 1.00 and 0.56, respectively.

3.4 Results

In this section, we present the harmonised Jungfraujoch FTIR dataset, the merged Lauder FTIR dataset and the Cape Grim *in situ* measurements. We performed trend analyses on these datasets from both hemispheres as well as on model data, with the purpose of comparing them and drawing some conclusions.

3.4.1 FTIR Jungfraujoch time series analysis

The 6921 Jungfraujoch spectra used for our study were recorded over 2055 sunny days between 25th June 1986 and 10th December 2020. Specifically, we have analysed the trend between January 2000 and December 2020 using monthly means (1699 days and 244 months).

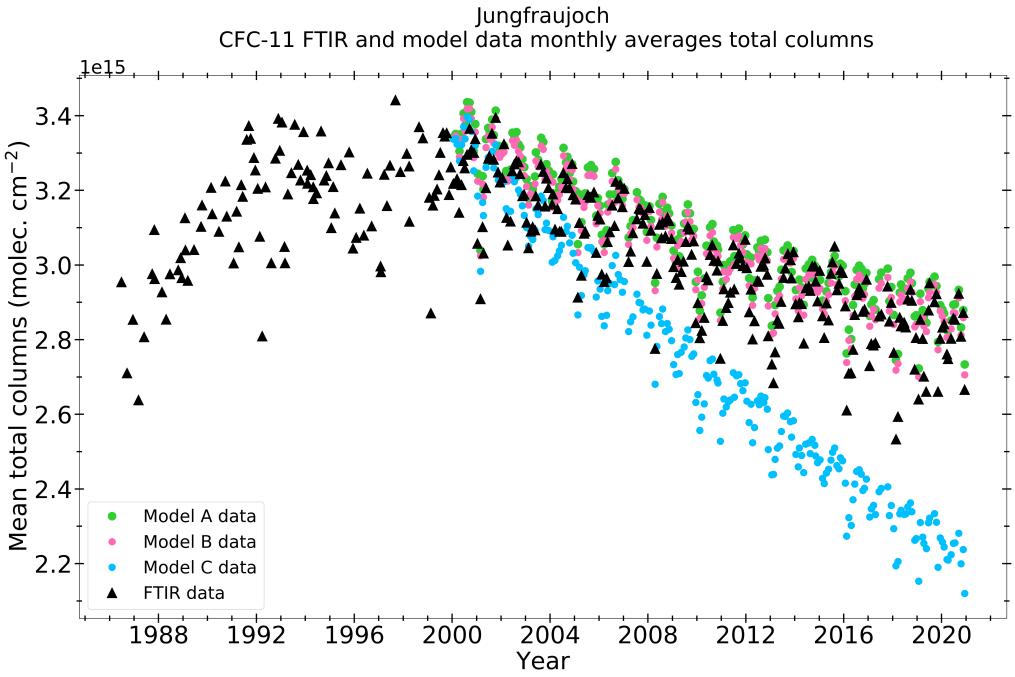

Figure 3.4. Jungfraujoch FTIR (from June 1986 to December 2020) and TOMCAT monthly mean total columns (from January 2000 to December 2020). In black, FTIR data; in green, TOMCAT model simulation A: best estimate of emissions and some realistic distribution (optimised with NOAA support); in pink, TOMCAT model simulation B: same total emissions as simulation A but equal emissions at all lat/lon; and in blue, TOMCAT model simulation C: zero emissions since 2000 (simple decay).

In order to obtain the whole time series shown in Figure 3.4, we had to harmonise the daily total columns since two different instruments were used. Furthermore, several changes were progressively implemented to the Bruker spectrometer, potentially affecting the instrumental response and thus also the CFC-11 retrieved columns. This is particularly true when a broad window is used, as is also the case for peroxyacetyl nitrate (PAN) (Mahieu et al., 2021). The first adjustment was to harmonise the two instruments (homemade and Bruker) time series by multiplying the Bruker time series by a factor of 0.9692 between 12/02/1999 and 09/10/2001. Afterwards, we multiplied the homemade instrument whole time series by a factor of 0.9467.

These correction factors were found by comparing the coincident data present in the two subsets (homemade and Bruker) for the same days. Nevertheless, there was still a non-scaled period from 16/10/2015 to 18/06/2019, found to be inconsistent because of the change of one spectrometer mirror in the Bruker instrument. Thus, they were scaled up (factor of 1.0181) so as to get the optimum alignment of this subset with respect to the earlier and following column data. These corrections allowed us to acquire the harmonised series from June 1986 to December 2020 shown in Figure 3.4.

3.4.2 FTIR Lauder time series analysis

At Lauder, 4907 FTIR spectra were recorded over 1685 sunny days (225 months), from 11th October 2001 to 27th December 2020. As we did with the JFJ time series, we have analysed the trend between October 2001 and December 2020 using monthly means.

The Lauder Bruker IFS-120HR spectrometer was replaced in 2018 by a Bruker IFS-125HR and, as observed in the Jungfraujoch time series, this kind of change can affect the instrumental response and the retrieved quantities. Therefore, we used the common days of observation between both instruments to estimate a correction factor in order to merge both datasets (Bruker IFS-120HR and Bruker IFS-125HR). We found a 1.4% difference, thus we multiplied the 125HR time series by this factor. The final dry air mole fraction (xCFC-11) time series is shown in Figure 3.6(a).

Within the Lauder time series, there were unexpectedly high CFC-11 total columns between 2007 and 2009.5. For the purpose of finding the main cause of this time series feature, several hypotheses were tested. Firstly, we analysed the xCFC-11 time series since the Lauder station is a relatively low-altitude site and it is strongly influenced by water vapour. The unexpectedly high points were also present in the xCFC-11 amounts. Secondly, we analysed the *in situ* mixing ratio CFC-11 time series (blue points in Figure 3.6(a)) at Cape Grim (Tasmania, Australia) from October 2001 to September 2020. The Cape Grim time series did not show a shape of that sort. Therefore, we continued investigating by analysing the FTIR CFC-12 (CCl_2F_2) and N_2O total columns above Lauder, since they are a co-emitted species and a dynamical tracer, respectively. These species did not show any anomalies.

A series of tests were performed to assess the robustness of the retrieval strategy. This involved investigating the effect of MCT detector non-linearity (saturation point fitting), instrument response function changes and fitting of the broad retrieval window continuum level. In all tests, the unexpectedly high abundances over 2007 – 2009.5 were still present, and the linear trend analysis results were not significantly altered (details in Section 3.4.3.2). Even though we presently cannot find fault with the measurements and retrieval strategy, the anomalous values cannot be reconciled with CFC-11 emission rates or transport/dynamic circulation changes, thus the cause for this feature still remains unresolved.

3.4.3 Trend analyses

The time series trends presented in this section were obtained using the auto-regressive wild bootstrap (AWB) method developed by Friedrich et al. (2020a,b). This method first tests for the presence of a break point in the trend function. If there is evidence of a break, it locates the

break point that best fits the data (where the fit is determined by the sum of squared deviations from the broken trend line). Then, it determines the uncertainty around the break location using the AWB method. It also estimates the pre- and post-break trends slopes using ordinary least squares (OLS) and judges the significance of the estimated trend slopes using the bootstrap method. We used a 95% confidence interval.

3.4.3.1 Northern Hemisphere

The FTIR Jungfraujoch monthly mean total columns from January 2000 until December 2020 are displayed in Figure 3.5(a) with the error bars showing the standard deviation around the monthly means. The mean relative standard deviation is 2%, i.e., lower than the random uncertainty reported in Table 3.1. We performed a linear trend analysis of all the data (2000 – 2020). We found that the CFC-11 atmospheric concentration decreased by $(2.34 \pm 0.14)10^{13}$ molecules·cm^{-2} per year, or a relative decrease of $(0.78 \pm 0.05)\%$ yr^{-1}. Since Montzka et al. (2018) reported a slowdown in the decrease of the atmospheric CFC-11 concentrations, we used the Friedrich et al. (2020b,a) approach in order to find the break location and estimate the trend change. We found a statistically significant break point around 2011. The blue vertical line in Figure 3.5(a) indicates the break point at 2010.96, and a large confidence interval varying within 2005.20 and 2020.90 is indicated by the two black vertical lines. The pre-break slope (i.e., from 2000 until $\approx$ 2011) is $(-2.87 \pm 0.39)10^{13}$ molecules·cm^{-2} yr^{-1}, representing a relative decrease of $(0.95 \pm 0.13)\%$ yr^{-1}; while the post-break (2011 – 2020) trend decrease is $(1.84 \pm 0.44)10^{13}$ molec. cm^{-2} per year, that is a relative trend of $(-0.61 \pm 0.15)\%$ per year. This trend change of around 36% is significant at the 2σ level of uncertainty. This trend change is in good agreement with the trend change estimated from the ACE-FTS mixing ratios trend values reported by Bernath et al. (2020), as well as from the NOAA and AGAGE data, as shown in Figure 3.1. The red dashed line shows the divergence between an unperturbed situation and the current rate of change of CFC-11 following the recent renewed emissions.

The FTIR time series is compared to TOMCAT model outputs for the Jungfraujoch station location. Three different scenarios were carried out for the January 2000 – December 2020 period. We chose the scenario with the best estimate of emissions and the most realistic distribution (run A). In Figure 3.5(b), we can see that the break location is found at 2010.75, with a confidence interval ranging from 2008.66 to 2012.66, which lies within the confidence interval obtained for the break point in the FTIR time series. The standard deviation around the monthly means is shown by the error bars and the mean relative standard deviation is 1.5%, which is lower than for the FTIR measurements. Model data are not affected by random noise as are the measurements. The pre-break trend is $(-3.18 \pm 0.25)10^{13}$ molecules·cm^{-2} per year, i.e., $(-1.03 \pm 0.08)\%$ yr^{-1}, whereas the slope is $(-1.69 \pm 0.29)10^{13}$ molecules·cm^{-2} per year ($(-0.55 \pm 0.09)\%$ yr^{-1}) for the post-break period.

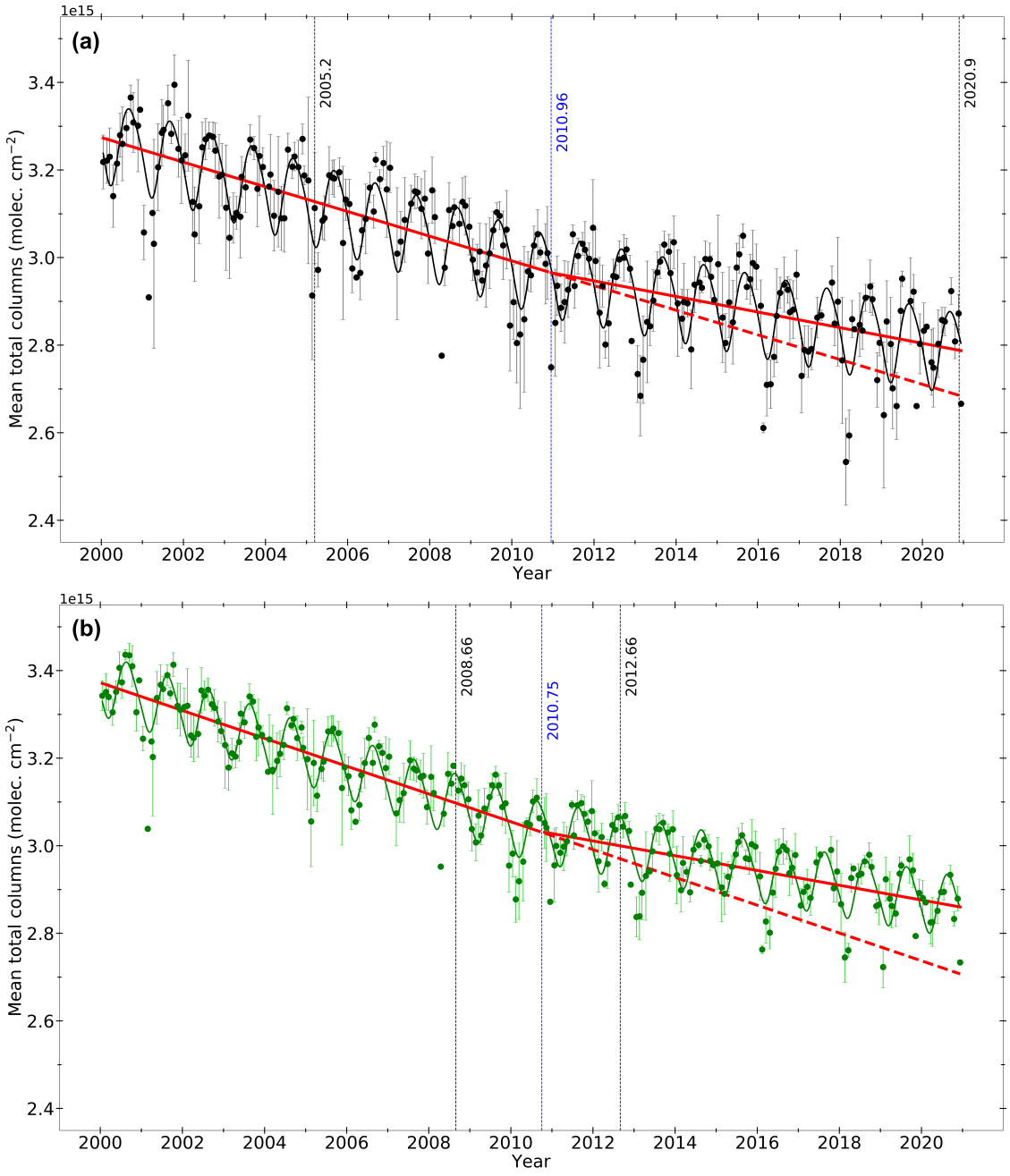

Figure 3.5. (a) FTIR and (b) TOMCAT monthly time series of CFC-11 total columns above Jungfraujoch. All vertical bars represent the standard deviations (1σ) around the monthly means. (a) Total columns have been derived from solar spectra recorded by the Bruker IFS-120HR spectrometer. (b) The "best estimation/realistic" simulation (tracer A) has been chosen.

	2000 – 2020	Break location	2000 – Break	Break – 2020	
xCFC-11 FTIR JFJ	-1.70 ± 0.08	2010.92	-2.01 ± 0.18	-1.35 ± 0.23	Dry air mole fraction trends (ppt yr^{-1})
	-0.79 ± 0.04		-0.90 ± 0.08	-0.66 ± 0.11	Relative trends (% yr^{-1})
CFC-11 FTIR JFJ	-2.34 ± 0.14	2010.96	-2.87 ± 0.39	-1.84 ± 0.44	Total columns trends (10^{13} molec. cm^{-2} yr^{-1})
	-0.78 ± 0.05		-0.95 ± 0.13	-0.61 ± 0.15	Relative trends (% yr^{-1})
xCFC-11 TOMCAT for JFJ (tracer A run)	-1.80 ± 0.05	2010.38	-2.29 ± 0.10	-1.34 ± 0.09	Dry air mole fraction trends (ppt yr^{-1})
	-0.82 ± 0.02		-1.04 ± 0.04	-0.61 ± 0.04	Relative trends (% yr^{-1})
TOMCAT for JFJ (tracer A run)	-2.47 ± 0.11	2010.75	-3.18 ± 0.25	-1.69 ± 0.29	Total columns trends (10^{13} molec. cm^{-2} yr^{-1})
	-0.80 ± 0.04		-1.03 ± 0.08	-0.55 ± 0.09	Relative trends (% yr^{-1})
xCFC-11 TOMCAT for JFJ (tracer C run)	-3.90 ± 0.06	–	–	–	Dry air mole fraction trends (ppt yr^{-1})
	-2.00 ± 0.03		–	–	Relative trends (% yr^{-1})
TOMCAT for JFJ (tracer C run)	-5.44 ± 0.11	–	–	–	Total columns trends (10^{13} molec. cm^{-2} yr^{-1})
	-1.99 ± 0.04		–	–	Relative trends (% yr^{-1})

Table 3.2. xCFC-11 (not shown in the plots) and CFC-11 total columns annual trends derived from the Jungfraujoch FTIR time series and TOMCAT model.

Since the Lauder and Cape Grim stations are relatively low-altitude sites, they are influenced by water vapour. In order to create comparable datasets in both hemispheres, we analysed the FTIR dry air mole fraction (xCFC-11) trends (for JFJ and LAU). The xCFC-11 is computed by dividing the CFC-11 total columns by the dry air pressure column (DPC) (Barthlott et al., 2015). The DPC is calculated by using the ground pressure of the station location to calculate column air concentrations, according to the Eq. 1 of Barthlott et al. (2015):

$$\mathrm{DPC} = \frac{\mathrm{P_s}}{\mathrm{M_{dryair}} \cdot \mathrm{g}(\varphi)} - \frac{\mathrm{M_{H_2O}}}{\mathrm{M_{dryair}}} \cdot \mathrm{H_2O_{col}} \tag{3.2}$$

where $\mathrm{P_s}$ is the surface pressure (in Pa), $\mathrm{g}(\varphi)$ is the latitude-dependent surface acceleration due to gravity (at the station location), $\mathrm{M_{dryair}}$ is the molecular mass of the dry air ($\approx 28.96 \cdot 10^{-3}$ $\mathrm{N_A}$ kg molec.$^{-1}$), $\mathrm{M_{H_2O}}$ is the molecular mass of the water vapour ($\approx 18 \cdot 10^{-3}$ $\mathrm{N_A}$ kg molec.$^{-1}$), $\mathrm{N_A}$ is the Avogadro's constant ($\approx 6.022 \cdot 10^{23}$ molecules mol^{-1}), and $\mathrm{H_2O_{col}}$ is the water vapour total column amount (in molecules m^{-2}).

The xCFC-11 FTIR trend for the whole Jungfraujoch time series is (-1.70 ± 0.08) ppt yr^{-1}, i.e., (-0.79 ± 0.04)% per year. The break point for the xCFC-11 time series was found at 2010.92 with a confidence interval extending from 2007.00 to 2016.25. Before the break, the trend decreases by (2.01 ± 0.18) ppt yr^{-1}, which is a relative trend of (-0.90 ± 0.08)% per year; while the post-break trend is (-1.35 ± 0.23) ppt yr^{-1}, i.e., (-0.66 ± 0.11)% per year. This leads to a trend change of around 30%. All the trend estimates in Table 3.2 show the excellent agreement between the FTIR and the model data above the Jungfraujoch station.

We have also analysed the 06/1986 – 12/1992 trend preceding the plateau (see Figure 3.4) in the FTIR Jungfraujoch data. This upward trend is $(7.27 \pm 1.67)10^{13}$ molecules·cm^{-2} per year, i.e., (2.35 ± 0.54)%/year. In this case, due to the small number of monthly data of this period, we carried out the trend analysis using the daily data. These results are in agreement with the trends calculated from the atmospheric histories for CFC-11 for this period (2.53%/yr) (Bullister, 2015). These historical values were determined from experimental observations made by the Atmospheric Lifetime Experiment / Global Atmospheric Gases Experiment / Advanced Global Atmospheric Gases Experiment (ALE / GAGE / AGAGE) network at the Northern Hemisphere.

3.4.3.2 Southern Hemisphere

The monthly xCFC-11 above Lauder, as well as the *in situ* monthly CFC-11 at Cape Grim and model data, are shown in Figure 3.6. Error bars indicate the standard deviation around the monthly means. The average relative standard deviation is 1.6% for the Lauder data, 0.08% for the Cape Grim data, and 1.4% for the model data.

The break location is found at 2014.13 for Lauder and at 2014.69 for Cape Grim time series (Figure 3.6(a)). The ranges for the confidence interval are shown by the dashed vertical lines: the black ones correspond to the Lauder data, while the blue ones show the Cape Grim confidence interval. Comparing these results to the model time series (Figure 3.6(b)), we can see that the break point found for the observations fits inside the confidence interval of the model data break location.

The trends before and after the break points, as well as the long-term trends (2001 – 2020) for the Cape Grim and Lauder stations, and for the model results for Lauder are listed in Table 3.3. Note that model trends are shown in total columns (molec. cm^{-2} yr^{-1}), while *in situ* Cape Grim trends and FTIR Lauder trends are displayed in ppt yr^{-1}. We computed the xCFC-11 trends (LAU) without the unexpectedly high points between 2007 and 2009.5 in order to verify if the trends values changed. The relative trend before the break point obtained is $(-1.34 \pm 0.08)\%\,yr^{-1}$, while the trend after the break point is $(-0.39 \pm 0.10)\%\,yr^{-1}$. The break location estimated without the 2007 – 2009.5 data is $2013.81 \pm^{0.71}_{1.14}$. As it can be observed, the trends values and the break location (with and without this period) did not change significantly. The results presented in Table 3.3 are those obtained for the whole dataset.

For the Cape Grim *in situ* observations, the pre-break trend decreases by $(0.82 \pm 0.01)\%\,yr^{-1}$, while the post-break trend decay is $(0.52 \pm 0.01)\%\,yr^{-1}$, which is a 37% change in the trend. For the model simulations for the Lauder location, the trend before the break is $(-0.86 \pm 0.05)\%\,yr^{-1}$, while the trend after the break is $(-0.61 \pm 0.07)\%\,yr^{-1}$, bringing about a 30% trend change.

A significant point to note is the agreement between the relative trends. As one can observe, the relative trend for the whole time series (2001 – 2020) is the same for Cape Grim and for the model and quite close for Lauder (36% difference), considering the unexplained feature of this time series. Regarding the pre-break and post-break relative trends, this behaviour is the same.

3.4.3.3 Inter-hemispheric analysis

In the case of the Jungfraujoch site, all the trends (long-term, pre-break, and post-break) are in a very good agreement (i.e. within uncertainty estimates). For the Lauder site, there were some differences because of the unexpectedly high data over 2007 – 2009.5. Through the comparison with the Cape Grim *in situ* observations, we can see that the relative trends between the observations and the model are also in good agreement. Regarding the long-term trends (2000 – 2020), they are quite similar in both hemispheres, both for the model and the observations. Before the break point, the trend decay in the NH was more important than in the SH (around 10%). The post-break trend decrease is 20% larger in the NH for the observations, while it is 10% smaller for the model results than in the SH. Nevertheless, if we take into account the errors of each trend, we can affirm that all of the trend values lie within the error limits (see Table 3.2 and Table 3.3).

The Report on the Unexpected Emissions of CFC-11, 2021 (Chipperfield et al., 2021) documents that the CFC-11 atmospheric global concentrations decayed by $0.8\%\,yr^{-1}$ from 2002 to 2012, and by $0.5\%\,yr^{-1}$ from 2014 to 2018. Fortunately, the atmospheric concentrations declined faster between 2018 and 2019 (by $0.7\%\,yr^{-1}$). If we compare these trends to our observations, we can affirm that they are in a very good agreement. For the pre-break period, we obtained a decay of $(0.95 \pm 0.13)\%\,yr^{-1}$ (2000 – 2011) in the NH, and a decay of $(0.82 \pm 0.01)\%\,yr^{-1}$ (2001 – 2014) in the SH (Cape Grim). For the post-break period, we obtained a decay of $(0.61 \pm 0.15)\%\,yr^{-1}$ (2011 – 2020) in the NH. In the SH, we got a decay of $(0.52 \pm 0.01)\%\,yr^{-1}$ for Cape Grim, and $(0.39 \pm 0.10)\%\,yr^{-1}$ for Lauder (2014 – 2020). Nevertheless, nowadays we cannot detect trend changes like the one after 2018 with FTIR observations, even for daily averages. We will need a longer time series after 2018 to be able to detect it.

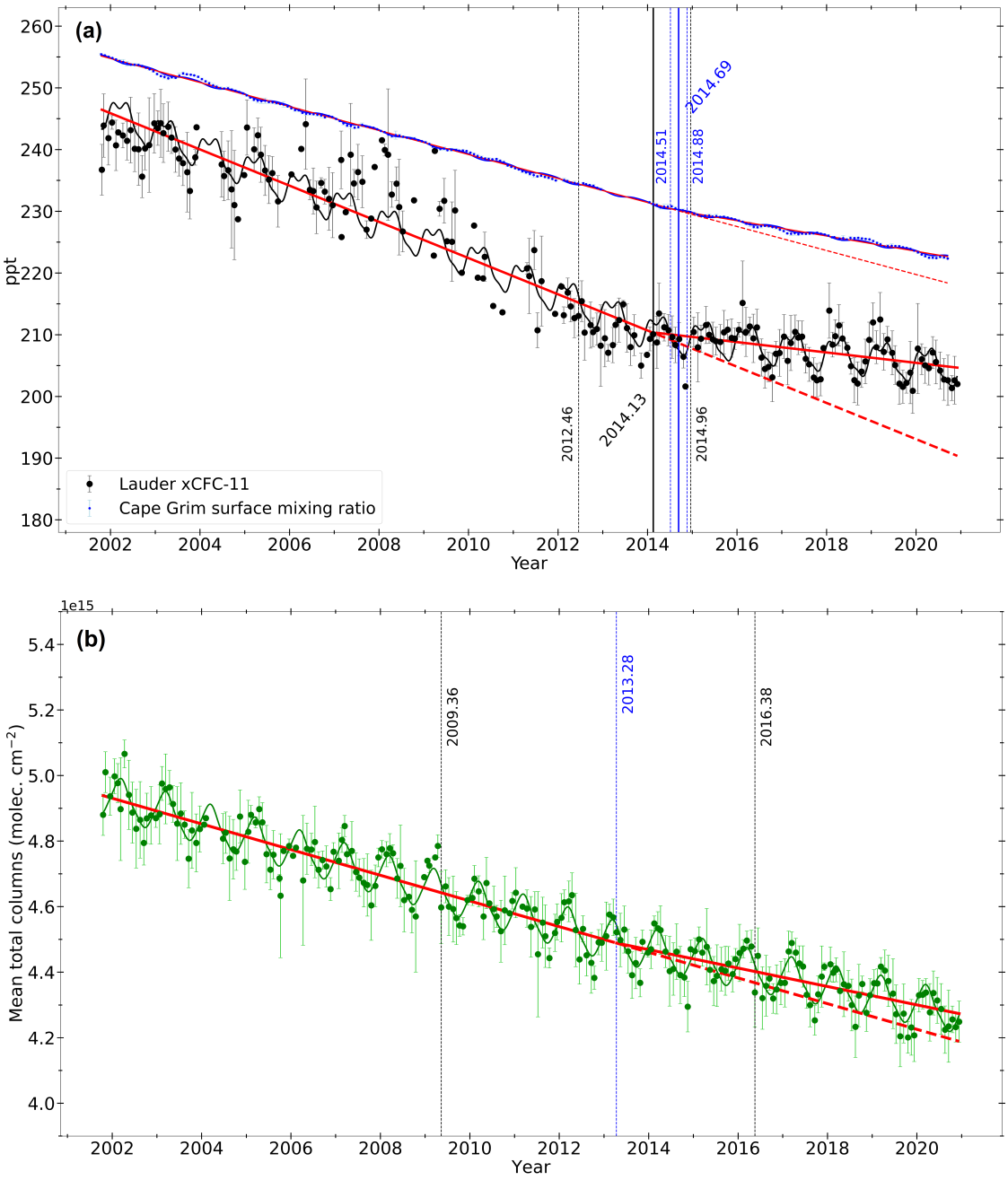

Figure 3.6. (a) *In situ* monthly CFC-11 at Cape Grim (in blue) and monthly xCFC-11 FTIR above Lauder (in black). (b) TOMCAT model monthly time series of CFC-11 total columns above Lauder. The "best estimation/realistic" simulation (tracer A) has been chosen. All vertical bars represent the standard deviations (1σ) around the monthly means.

	2001 – 2020	Break location	2001 – Break	Break – 2020	
***In situ* Cape Grim**	-1.77 ± 0.02	2014.69	-1.94 ± 0.01	-1.23 ± 0.03	Surface mixing ratio trends (ppt yr^{-1})
	-0.74 ± 0.01		-0.82 ± 0.01	-0.52 ± 0.01	Relative trends (% yr^{-1})
xCFC-11 FTIR LAU	-2.32 ± 0.08	2014.13	-2.94 ± 0.17	-0.86 ± 0.23	Dry air mole fraction trends (ppt yr^{-1})
	-1.05 ± 0.04		-1.34 ± 0.08	-0.39 ± 0.10	Relative trends (% yr^{-1})
xCFC-11 TOMCAT	-1.72 ± 0.05	2011.25	-2.05 ± 0.15	-1.38 ± 0.12	Dry air mole fraction trends (ppt yr^{-1})
for LAU (tracer A run)	-0.77 ± 0.02		-0.92 ± 0.06	-0.62 ± 0.05	Relative trends (% yr^{-1})
TOMCAT for LAU	-3.52 ± 0.11	2013.28	-3.92 ± 0.22	-2.81 ± 0.33	Total columns trends (10^{13} molec. cm^{-2} yr^{-1})
(tracer A run)	-0.77 ± 0.02		-0.86 ± 0.05	-0.61 ± 0.07	Relative trends (% yr^{-1})
xCFC-11 TOMCAT	-3.86 ± 0.05	–	–	–	Dry air mole fraction trends (ppt yr^{-1})
for LAU (tracer C run)	-1.96 ± 0.03		–	–	Relative trends (% yr^{-1})
TOMCAT for LAU	-7.93 ± 0.10	–	–	–	Total columns trends (10^{13} molec. cm^{-2} yr^{-1})
(tracer C run)	-1.96 ± 0.02		–	–	Relative trends (% yr^{-1})

Table 3.3. CFC-11 annual trends derived from the *in situ* measurements at Cape Grim, xCFC-11 and CFC-11 annual trends derived from the Lauder FTIR time series and TOMCAT model.

According to Holzer and Waugh (2015), the tropospheric mean time needed for the CFCs to travel from the NH, where the principal emissions happen, to the SH varies from 1.1 years (in the South Hemisphere tropics) to 1.4 years (at the South Pole). These values are compatible with our observations and TOMCAT simulations, taking into account the uncertainty ranges.

3.5 Summary and conclusions

We have applied consistent retrievals and analysed CFC-11 total column time series, using Jungfraujoch and Lauder high-resolution FTIR solar spectra recorded within the framework of the NDACC network. For the first time, the Jungfraujoch time series was extended back to include spectra recorded before the 2000s, and fully harmonised to account for instrument replacements and upgrades. Our study is the first to present a merged CFC-11 FTIR dataset from Lauder. In both cases, we adopted a large spectral window (830.0 – 859.3 cm^{-1}) so as to include the broad CFC-11 feature, accounting for the interfering species, notably water vapour. The DOFS values are 1.36 for Jungfraujoch, and 1.57 for Lauder. The estimates of the relative total random and systematic uncertainties are 3.3% and 7.5%, respectively, for the Jungfraujoch station, and 2.2% and 7.2%, respectively, for the Lauder station.

The FTIR time series, supplemented with *in situ* surface data from Cape Grim, were compared with a TOMCAT model run implementing the undeclared CFC-11 emissions reported by Montzka et al. (2018), quantitatively confirming their impact on atmospheric CFC-11, both on the vertical and horizontal scales.

Trends between 2000 and 2020 were analysed for the Jungfraujoch station and between 2001 and 2020 for the Lauder and Cape Grim stations. Very good agreement was found between the observations and the model trends, especially for the Jungfraujoch station. A break point around 2011 was found for the Jungfraujoch FTIR and model data, while it appears around 2014 for the Southern Hemisphere. In the Northern Hemisphere, total columns declined by $(0.95 \pm 0.13)\%\ yr^{-1}$ and $(1.03 \pm 0.08)\%\ yr^{-1}$ (between 2000 and 2011), for the FTIR and model time series, respectively. A slowdown in the decay was observed after 2011, where we obtained a decay of $(0.61 \pm 0.15)\%\ yr^{-1}$ and $(0.55 \pm 0.09)\%\ yr^{-1}$ (between 2011 and 2020), for the FTIR and model time series respectively. In the Southern Hemisphere, the relative trends before the break point (2001 – 2014) are $(-0.82 \pm 0.01)\%\ yr^{-1}$ and $(-0.86 \pm 0.05)\%\ yr^{-1}$, for the *in situ* and model datasets, respectively; while the relative trends after the break point (2014 – 2020) are $(-0.52 \pm 0.01)\%\ yr^{-1}$, $(-0.39 \pm 0.10)\%\ yr^{-1}$, and $(-0.61 \pm 0.07)\%\ yr^{-1}$, for the *in situ*, FTIR, and model time series, respectively. These values are in a good agreement with those reported by the Report on the Unexpected Emissions of CFC-11, 2021 (Chipperfield et al., 2021). Therefore, the trend change estimated by the TOMCAT model was around 47% in the Northern Hemisphere and around 30% in the Southern Hemisphere.

These trend changes confirm that FTIR measurements are able to detect variations in CFC-11 emissions of the order of magnitude of those reported by Rigby et al. (2019). Taking into account the uncertainties, the differences in the break location between the Northern (≈ 2011) and the Southern (≈ 2014) Hemispheres are representative of the mean interhemispheric transit time, estimated as ≈ 1.1 years in the Southern Hemisphere tropics, and ≈ 1.4 years at the South Pole (Holzer and Waugh, 2015).

Our results confirm the success of the Montreal Protocol which has been able to significantly reduce CFC-11 emissions. Still, renewed emissions related to illegal production occurred for a few years but were quickly identified (Montzka et al., 2018; Rigby et al., 2019) and appear to have now decreased significantly (Montzka et al., 2021; Park et al., 2021). These FTIR measurements can also be used to monitor CFC-11 and help to detect rogue emissions, of a magnitude similar to that observed in 2012 – 2018, providing complementary monitoring to surface-measurement networks.

Because of the constant monitoring of the atmosphere, the scientific community has been able to swiftly spot non-compliant emissions of CFC-11 and identify their origin, which apparently led to their reduction. It is important to note that the model simulations implementing these additional emissions, the surface *in situ* and ground-based remote sensing time series, together provide a very consistent picture demonstrating a proper understanding of the processes driving the CFC-11 atmospheric burden and its evolution.

Chapter 4

First HFC-134a retrievals from ground-based FTIR solar absorption spectra

Numbered sections of this chapter follow:

Pardo Cantos, I., Mahieu, E., Chipperfield, M. P., Servais, C., Reimann, S., and Vollmer, M. K. (2024). First HFC-134a retrievals from ground-based FTIR solar absorption spectra, comparison with TOMCAT model simulations, *in-situ* AGAGE observations, and ACE-FTS satellite data for the Jungfraujoch station. *Journal of Quantitative Spectroscopy and Radiative Transfer*, 318. https://doi.org/10.1016/j.jqsrt.2024.108938.

Abstract. Successive regulations on the production and consumption of chlorofluorocarbons (CFCs) and hydrochlorofluorocarbons (HCFCs) have led to the use of hydrofluorocarbons (HFCs) as substitution products. Consequently, these potent greenhouse gases are now controlled under the Kigali Amendment (2016) to the Montreal Protocol. HFC-134a is the preferred substitute to CFC-12 as a refrigerant and is the most abundant HFC in the atmosphere today. This work presents the first retrievals from ground-based Fourier Transform Infrared (FTIR) high-resolution solar absorption spectra, recorded at the Jungfraujoch station as part of the Network for the Detection of Atmospheric Composition Change (NDACC). To verify these retrievals, the FTIR time series was compared to three other datasets: a simulation of the TOMCAT 3-D chemical transport model, the Fourier Transform Spectrometer on board the Atmospheric Chemistry Experiment (ACE-FTS) L2 v5.2 retrievals, and the Jungfraujoch *in situ* surface observations conducted within the Advanced Global Atmospheric Gases Experiment (AGAGE) network. The overall trends of HFC-134a (2004 – 2022) were analysed to assess the relative growth rates of this atmospheric compound. These trends are 7.34 ± 0.16%/year (FTIR), 7.12 ± 0.05%/year (TOMCAT), 7.29 ± 0.16%/year (ACE-FTS), and 6.61 ± 0.05%/year (*in situ*). The relative trends are in good agreement, so these novel FTIR retrievals are validated. Consequently, this strategy could be implemented at other NDACC sites to achieve a quasi-global detection of this species using the FTIR remote sensing technique.

4.1 Introduction

Since the discovery of the implication of chlorofluorocarbons (CFCs) in stratospheric ozone depletion by Molina and Rowland (1974), the Montreal Protocol on Substances that Deplete the Ozone Layer (1987) has aimed to limit the production and consumption of CFCs and other Ozone-Depleting Substances (ODSs) to protect the ozone layer and allow it to recover. The industry has therefore developed and produced substitutes for CFCs, the hydrochlorofluorocarbons (HCFCs). These substances have shorter atmospheric lifetimes and convey less chlorine atoms on a per molecule basis, which is why they are characterised by smaller ozone depletion potentials (ODPs). Still, HCFCs contribute to stratospheric ozone depletion, which led to their ban. Consequently, hydrofluorocarbons (HFCs), which are chlorine- and bromine-free molecules that do not affect the ozone layer, have been introduced to replace both CFCs and HCFCs (Harrison et al., 2021). Nevertheless, all these substances are strong infrared (IR) radiation absorbers and hence contribute to the Earth's radiative forcing (Velders et al., 2022). As HFCs are very potent greenhouse gases, they were included in the list of substances controlled by the Kyoto Protocol (1997), but no emission limits were established. Therefore, the Kigali Amendment (2016) to the Montreal Protocol came into force in 2019 to gradually reduce the global production and use of long-lived HFCs (Liang et al., 2022). HFCs are mainly used in refrigeration systems, air conditioning, and foam-blowing as well as firefighting agents and propellants (Liang et al., 2022). In the last years, the consumption and emissions of CFCs have decreased. While HCFC consumption and emissions have stabilised in recent years, those of the HFCs continue to rise (Liang et al., 2022). Since 2000, global HFC emissions estimated from atmospheric observations show a significant gap to the total CO_2-eq HFC emissions reported by Annex I countries in the United Nations Framework Convention on Climate Change (UNFCCC) in 2019 (Fig. 2-2 in WMO, 2022). Unfortunately, this gap between estimated and reported emissions has been broadening in the recent years. This difference could be explained by emissions from non-Annex I countries and/or by unrecorded emissions, considering that many countries still do not report to the UNFCCC, or not possess monitoring systems for recurrent atmospheric observations (Liang et al., 2022). The total CO_2-eq emissions (based on 100-yr time horizon Global Warming Potential, GWP) by HFCs in 2020 has been estimated to be 1.22 ± 0.05 Gt CO_2-eq yr^{-1} (Liang et al., 2022).

1,1,1,2-Tetrafluoroethane or CH_2FCF_3 (HFC-134a) has replaced CFC-12 as the preferred refrigerant and is the most abundant HFC in the atmosphere (Liang et al., 2022). Its total atmospheric lifetime is 13.5 years (14.1 years in the troposphere and 313 years in the stratosphere) (Burkholder et al., 2022). The large difference between the tropospheric and the stratospheric lifetimes is due to the reaction with tropospheric OH, the main atmospheric sink for HFC-134a (responsible for 99% of its atmospheric degradation) (Harrison et al., 2021). Atmospheric HFC-134a loss produces COF_2, HF and trifluoroacetic acid (TFA; CF_3COOH). This is a toxic breakdown product that accumulates in water reservoirs through wet deposition. However, it is known that the environmental impact of TFA still needs to be investigated (Daniel et al., 2022). It is estimated that HFC-134a emissions started in the early 1990s as the atmospheric HFC-134a levels began to rise in the mid-1990s. This is based on global *in situ* measurements by NOAA (National Oceanic and Atmospheric Administration) (Montzka et al., 1996, 2015). The GWP of HFC-134a is 1470 (100-yr) and it is the largest contributor to radiative forcing from HFCs with 44% of their total contribution (44.1 ± 0.6 mW m^{-2}) in 2020, which is about

30% more than in 2016. The share of HFC-134a in total HFCs emissions in 2020 is about 30%, which is an increase of about 20% since 2016 (Liang et al., 2022). Global emissions of HFC-134a estimated by the Advanced Global Atmospheric Gases Experiment (AGAGE) and NOAA networks are 247 ± 28 Gg yr^{-1} (or 364 ± 41 Tg CO_2-eq yr^{-1}) and 243 ± 27 Gg yr^{-1} (or 358 ± 39 Tg CO_2-eq yr^{-1}), respectively, in 2020 (Liang et al., 2022).

In this work, we describe the first retrieval strategy from ground-based Fourier Transform Infrared (FTIR) solar absorption spectra, and we analyse the HFC-134a atmospheric abundances above the Jungfraujoch station. To evaluate this first HFC-134a FTIR time series, we compare our retrieved total columns (presented as dry air mole fractions) to surface air measurements (AGAGE), satellite data (ACE-FTS instrument on board SCISAT) over Europe and TOMCAT model simulations for the period from January 2004 to December 2022. In Section 4.2, we describe the FTIR, *in situ* and satellite observations as well as the 3-D chemical transport model. In Section 4.3, we describe the retrieval strategy, and in Section 4.4, we present the results and discuss the trend analysis for the different datasets. Finally, we conclude this study in Section 4.5.

4.2 Measurement methods and datasets

4.2.1 NDACC FTIR observations at the Jungfraujoch station

The FTIR spectra used in this study were recorded under clear-sky conditions at the Jungfraujoch research station (46.55°N, 7.98°E) in the Swiss Alps at 3580 m above mean sea level (a.m.s.l.). The Jungfraujoch station is located between the Mönch (4107 m) and the Jungfrau (4158 m) summits, in a very dry area compared to other NDACC stations, due to the high altitude and the proximity of the Aletsch glacier (Mahieu et al., 2021). Spectra have been recorded since the early 1950s by the team of the Institute of Astrophysics of the University of Liège (Belgium). The high-resolution FTIR measurements began in 1984 (Zander et al., 2008) and are now conducted as part of the Network for the Detection of Atmospheric Composition Change (NDACC) (De Mazière et al., 2018). The retrievals presented in this article were obtained from a subset of high-resolution infrared solar absorption spectra recorded with a Bruker IFS-120HR spectrometer, modified by the team, and in operation since the early 1990s. These observations were made with a HgCdTe (mercury cadmium telluride, MCT) detector and they cover the 700 – 1400 cm^{-1} spectral range with a spectral resolution of 0.0061 cm^{-1}, that is a maximum optical path difference (OPD) of 82 cm.

4.2.2 AGAGE *in situ* observations at the Jungfraujoch station

In addition to measurements by FTIR, fully independent observations of HFC-134a at Jungfraujoch are also available through *in situ* measurements using preconcentration gas chromatography - mass spectrometry (GCMS) (Reimann et al., 2020). As part of a suite of ≈ 50 halogenated substances, high-precision HFC-134a measurements have been conducted within the AGAGE network (Prinn et al., 2018). At Jungfraujoch, measurements began in 2000 using a GCMS-ADS (adsorption/desorption) system (Simmonds et al., 1995) followed by Medusa-GCMS technology in 2008 (Prinn et al., 2018; Miller et al., 2008). For the Medusa-GCMS, 2L

samples are preconcentrated on a first trap and held at ≈ -160 °C. The samples are desorbed at 100 °C and cryofocussed on a second trap before injection into the GCMS. The measurement of one sample takes about 70 minutes. After each pair of air samples, a calibration gas (quaternary standard) is measured to track and correct for MS signal drift. Measurement precision for HFC-134a is about 0.3% (1σ). The HFC-134a measurements are fully intercalibrated within the AGAGE network and are reported as dry-air mole fraction in pmol mol^{-1} (parts-per-trillion, ppt) on the Scripps Institution of Oceanography (SIO) calibration scale SIO-05 with an estimate accuracy of $\approx 2\%$. For the present study, only baseline measurements (deemed representative for a broad atmospheric region) were used, based on a statistical filtering algorithm (O'Doherty et al., 2001; Cunnold et al., 2002).

4.2.3 ACE-FTS observations

The ACE-FTS instrument on board the Atmospheric Chemistry Experiment (ACE), also known as SCISAT, is the main instrument of this Canadian satellite (Bernath et al., 2005). SCISAT was launched into low Earth circular orbit by NASA in August 2003. Since February 2004, this satellite has been collecting data of the atmospheric pressure, temperature, and several molecular abundances (Fernando et al., 2019). ACE-FTS is a Fourier Transform Spectrometer (FTS) that records up to 30 IR transmittance spectra per day at sunrise and sunset by solar occultation. The locations of the occultations are determined by the orbit of the satellite and its relative position to the Sun (Harrison et al., 2021). This instrument operates in the range from 750 to 4400 cm^{-1} with a spectral resolution of 0.02 cm^{-1} (Fernando et al., 2019). The signal-to-noise ratio (SNR) ranges from about 100:1 to about 400:1 (Boone et al., 2023). The vertical resolution averages about 3 km and each occultation analyses the atmosphere from 150 km down to the cloud tops, or down to 5 km at best under clear-sky conditions (Harrison et al., 2021). Five micro-windows (MWs) are used for the HFC-134a retrievals: MW_1 = 828.78 – 829.28 cm^{-1}; MW_2 = 1090.20 – 1090.60 cm^{-1}; MW_3 = 1103.04 – 1105.84 cm^{-1}; MW_4 = 1949.93 – 1950.28 cm^{-1}; and MW_5 = 2623.63 – 2624.28 cm^{-1} (Fernando et al., 2019). For this study, we used ACE-FTS Level 2 v5.2 retrievals of the HFC-134a molecular abundances, expressed as volume mixing ratios (VMRs), from 5.5 km to 15.5 km for a latitude band around the Jungfraujoch station (40-50°N). We limited the ACE-FTS measurements to 15.5 km because the vertical profile decreases meaningfully above this altitude (Bernath et al., 2005; Harrison et al., 2021). Further information on the ACE-FTS version 5 retrievals can be found in Boone et al. (2023).

4.2.4 The TOMCAT/SLIMCAT chemical transport model

To help interpret the observations, we used output from a simulation of the TOMCAT / SLIMCAT (hereafter TOMCAT) three-dimensional (3-D) chemical transport model (CTM) (Chipperfield, 2006). The simulation used here had a horizontal resolution of $2.8^\circ \times 2.8^\circ$ with 32 levels from the surface to ≈ 60 km. The model was forced using meteorology from European Centre for Medium-Range Weather Forecasts (ECMWF) ERA5 reanalyses (Hersbach et al., 2020) and was integrated from 1979 until 2022. The model contained a detailed treatment of stratospheric chemistry including interactive calculation of photochemistry (OH, photolysis) relevant for HFCs.

The model run was constrained by specifying the monthly mean global mean surface VMRs of the long-lived source gases. For species such as CFCs and HCFCs, these are taken from the Scientific Assessment of Ozone Depletion (2018). For HFCs, including HFC-134a, the global mean surface VMRs are taken from the NOAA Annual Greenhouse Gas Index (data obtained from `https://gml.noaa.gov/aggi/aggi.html`). This boundary condition constraint means that the model does not simulate the spatial and short-term temporal variation in the surface concentration of HFC-134a. The model does, however, simulate the relative HFC-134a profile shape through atmospheric transport and loss processes. For comparison with observations, the simulated model profile was sampled daily (at 0 UTC) at the location of Jungfraujoch.

4.3 HFC-134a total column retrievals

4.3.1 Retrieval strategy

Since the main absorber in the infrared domain is water vapour, the dry conditions of the Jungfraujoch station facilitate the detection, retrieval, and analysis of trace gases with very weak spectral absorptions, such as HFC-134a. The application to other NDACC sites has yet to be tested.

We investigated all the significant HFC-134a features included in the pseudo-linelist produced by G. C. Toon from the Jet Propulsion Laboratory (`https://mark4sun.jpl.nasa.gov/`), which is based on six laboratory absorption cross-section datasets from Clerbaux et al. (1993); Highwood and Shine (2000); Nemtchinov and Varanasi (2004); Sharpe et al. (2004); Gohar et al. (2004), and Harrison (2015) (`https://mark4sun.jpl.nasa.gov/data/spec/Pseudo/HFC-134a_PLL.compressed.pdf`). However, only two were suited for the inversion of our ground-based solar atmospheric spectra: 1104.300 – 1105.585 cm^{-1} and 1182.0 – 1186.4 cm^{-1}. In this work, we will only analyse the results for the first window since the second one shows a strong water vapour absorption between about 1185.0 cm^{-1} and 1186.4 cm^{-1}, which masks the main absorption of HFC-134a, even at Jungfraujoch (see Figure 4.2). In addition, the HFC-134a absorption in the second window is smaller and more unstructured than in the first window. The first window range was also used by the ACE-FTS team for the HFC-134a retrievals (Fernando et al., 2019). To maximise the absorption depth of our target molecule and the information content, only the subset of observations with an apparent solar zenith angle (SZA) between 60° and 85° was fitted. For this work, we did not filter the observations according to water vapour or ozone columns since there is no dependency to the air mass, or the H_2O or O_3 total columns (Figure 4.3). However, some filtering could be necessary in more humid sites or in sites located at lower altitudes than Jungfraujoch.

For the retrieval of the HFC-134a total columns, we adopted a Tikhonov L1 regularisation with an α-parameter of 50. The simulations and retrievals of the total columns were performed using the SFIT4 v1.0.18 algorithm, which applies the Optimal Estimation Method (OEM) of Rodgers (2000). The layer scheme spanned 41 layers from 3.58 km to 120 km high, and thickness gradually rose from 0.65 km for the lowest layer up to 14 km for the highest layer.

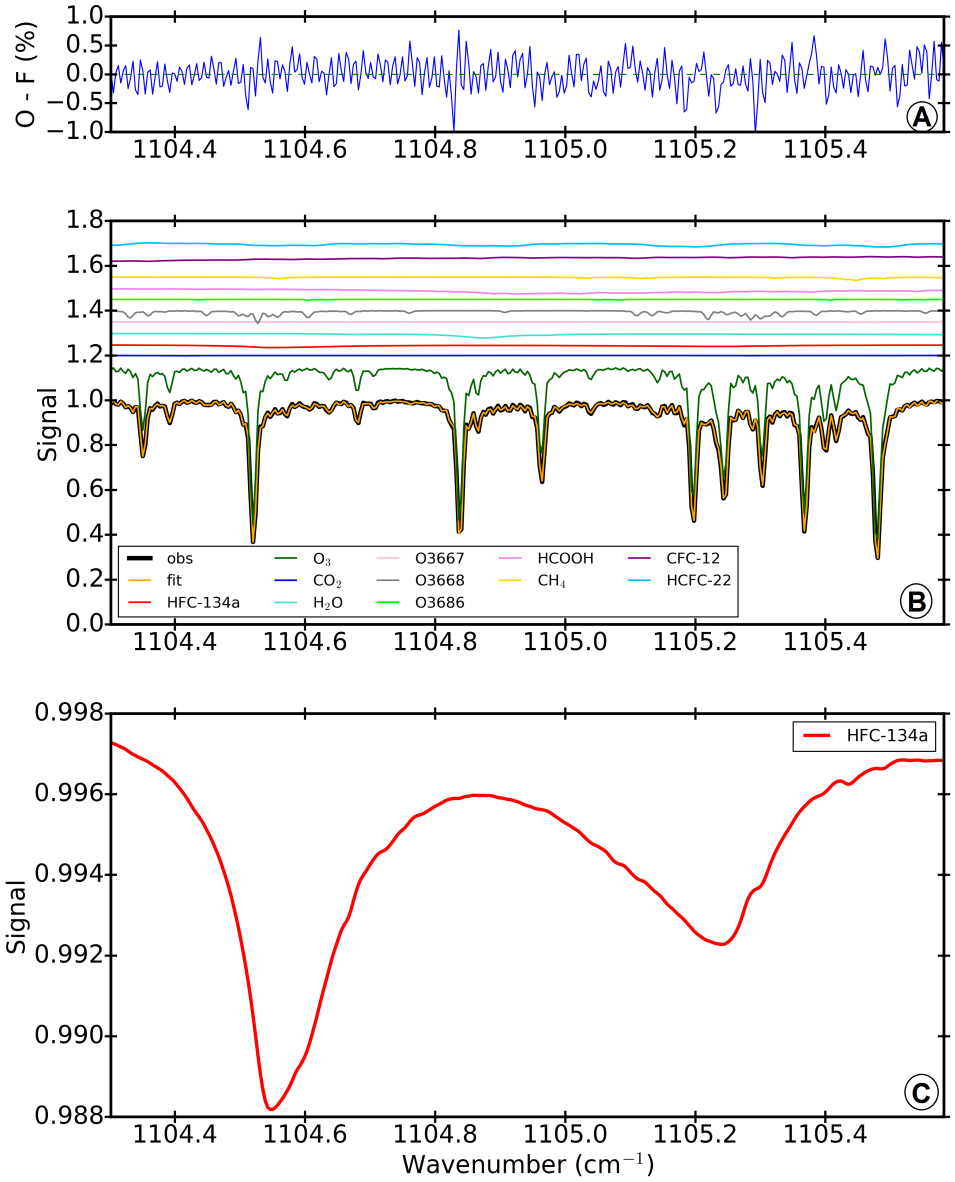

Figure 4.1. Spectral window for HFC-134a. Panel A displays the observed – calculated residuals, in %, from the simulation to the spectrum recorded on 25th May 2016. The root-mean-square of the fitting residuals is 0.27%. Panel B shows the simulation of the 1104.300 – 1105.585 cm^{-1} spectral window for spectra recorded by the Bruker IFS-120HR FTIR instrument at the Jungfraujoch station at an apparent solar zenith angle of 77.2°, and a maximum optical path difference of 82 cm. The signal-to-noise ratio for this spectrum is 952. The main interfering species (O_3, CO_2, H_2O, the ozone isotopologues, HCOOH, CH_4, CFC-12, and HCFC-22) are shifted vertically for clarity. Be aware of the scale of the vertical axis in Panel C, where the HFC-134a absorption is magnified.

The simulated interfering species are CO_2, H_2O, O_3, some ozone isotopologues (O3667, O3668, and O3686), formic acid (HCOOH), CH_4, CCl_2F_2 (CFC-12), and $CHClF_2$ (HCFC-22). These interfering molecules were also used for the HFC-134a ACE-FTS retrievals by Fernando et al. (2019). The spectroscopic parameters for the interfering species were obtained from the HITRAN2020 database (Gordon et al., 2022) and the empirical pseudo-linelist created by G. C. Toon for the unresolved features of the halocarbons (`https://mark4sun.jpl.nasa.gov/pseudo.html`). The spectroscopic parameters of water vapour were obtained from the ATM20

(https://mark4sun.jpl.nasa.gov/specdata.html) compilation.

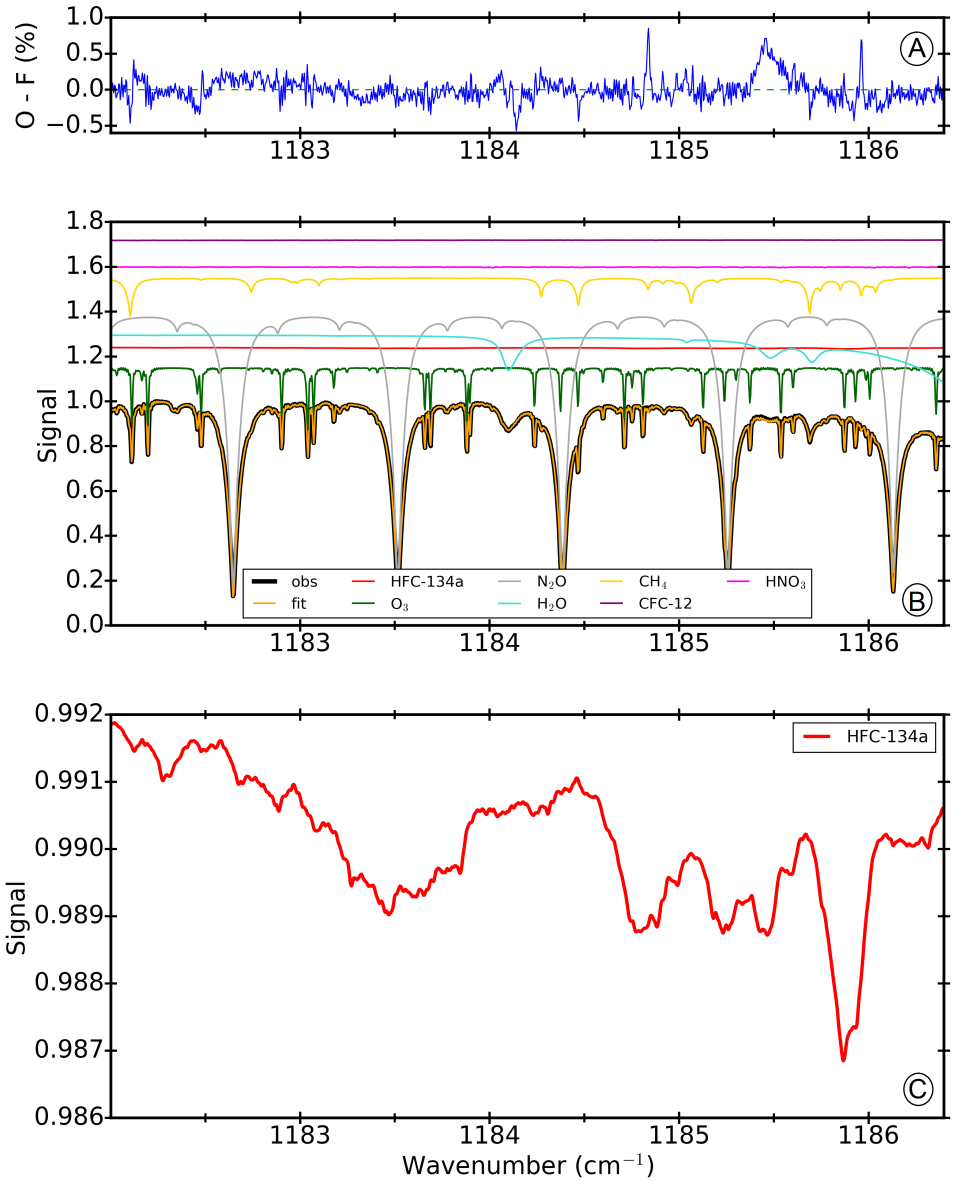

Figure 4.2. Second spectral window test for HFC-134a. Panel A displays the observed – calculated residuals, in %, from the simulation to the same spectrum as the one shown in Figure 4.1 (recorded on 25th May 2016). The root-mean-square of the fitting residuals is 0.23%. Panel B shows the simulation of the 1182.0 – 1186.4 cm^{-1} spectral window from spectra recorded by the Bruker IFS-120HR FTIR instrument at the Jungfraujoch station at an apparent solar zenith angle of 77.2°, and a maximum optical path difference of 82 cm. The signal-to-noise ratio for this spectrum is 952. The main interfering species (O_3, N_2O, H_2O, CH_4, CFC-12, and HNO_3) are shifted vertically for clarity. Be aware of the scale of the vertical axis in Panel C, where the HFC-134a absorption is magnified. The water vapour absorption present between about 1185.0 cm^{-1} and 1186.4 cm^{-1} becomes stronger for more humid days, masking the main absorption of HFC-134a in this spectral window.

A priori profiles of the interfering species were obtained from the Whole Atmosphere Community Climate Model (WACCM, version 6) climatological profiles over the period 1980 – 2040 (Gettelman et al., 2019), except for water vapour. *A priori* profiles of water vapour were supplied by the ERA-Interim (Berrisford et al., 2011) and ERA-5 (Hersbach et al., 2020) me-

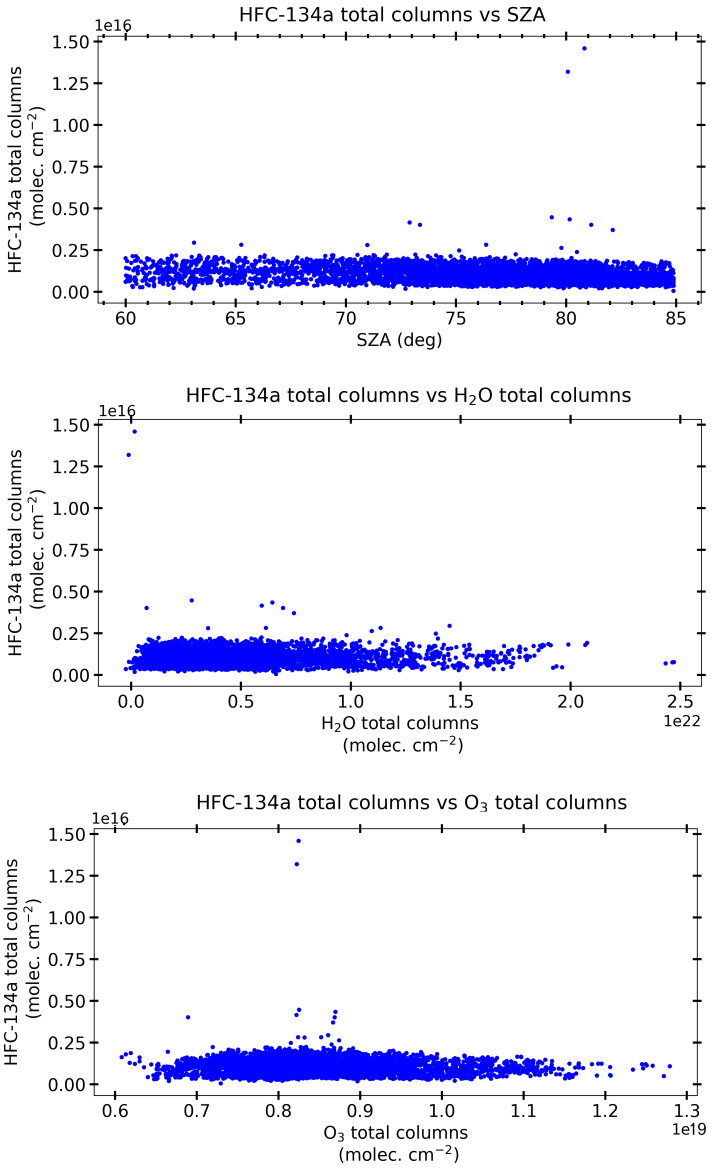

Figure 4.3. HFC-134a total columns retrieved from the ground-based FTIR solar spectra at the Jungfraujoch station versus the solar zenith angles on the top, versus the H_2O total columns on the middle, and versus the O_3 total columns on the bottom.

teorological reanalyses complemented with WACCMv6 monthly means for the uppermost atmospheric layers. Since HFC-134a is not included in the WACCM simulations, we used the ACE-FTS vertical distribution for 2006 (Harrison et al., 2021) as *a priori* profile for HFC-134a for the upper troposphere and lower stratosphere (5 – 15 km). The lower tropospheric *a priori* profile was considered constant from the lower limit of ACE-FTS HFC-134a profile (5 km). In the same way, the middle stratospheric *a priori* profile was considered constant from the upper limit of ACE-FTS HFC-134a profile (15 km). Using another year profile, for example 2018 (Harrison et al., 2021), as *a priori*, has no measurable effect on the retrieved FTIR products.

Panel B in Figure 4.1 shows a simulation of the 1104.300 – 1105.585 cm^{-1} spectral window. The observed spectrum (obs) is displayed in black and the simulated spectrum (fit) is shown in orange. Each individual molecule is shown in the colours indicated in the legend. As

can be observed, the main interferences in this window are due to ozone (in dark green). The absorption feature of HFC-134a (in red) peaks around 1104.55 cm^{-1} and 1105.24 cm^{-1} (see Panel C for clarity), surrounding the water vapour absorption (in light turquoise) in the center of the window. Even though the interferences from the other molecules appear very weak, we cannot ignore them since the absorption of our target molecule represents only about 1% (Panel C), so any small contribution from other species can be important for the retrievals. Panel A shows the fitting residuals (observed – calculated) from the simulated spectrum to a spectrum obtained on 25th May 2016. The residuals are close to the noise level, except around some of the most intense ozone absorption lines. The root-mean-square (RMS) of the fitting residuals is 0.27% and the H_2O total column is 7.3×10^{21} molec. cm^{-2} for this example. This spectrum is a good representation of the whole time series (2004 – 2022), as the median and mean RMS are 0.27% and 0.28%, respectively, and the median and the mean H_2O total columns are 5.4×10^{21} molec. cm^{-2} and 6.8×10^{21} molec. cm^{-2}, respectively. This spectrum was recorded with a maximum OPD of 82 cm at a solar zenith angle of 77.2°, which is at the median of the SZA of the whole spectra used in this study.

4.3.2 Uncertainty analysis of the measurements

The main sources of error affecting the retrievals of the total columns are listed in Table 4.1. This uncertainty budget was calculated for one year of spectra (2014), taken as an example in the middle of the time series. The random and systematic components are presented separately. To create the random component of the error covariance matrix, we used a constant relative standard deviation of 18%, based on ACE-FTS L2 v5.2 HFC-134a retrievals (Boone et al., 2023), for each level of the grid (1 km-levels between 5.5 and 15.5 km; between 40 and 50°N), which represents the average relative standard deviation for four months of the ACE-FTS time series (April – July 2012). The systematic part was produced using the mean relative difference between the ACE-FTS L2 v5.2 HFC-134a retrievals and the TOMCAT simulations in the lowest model layer for the same four months. The model simulations were used for this estimation as no other satellite observations are currently available. A constant relative difference of 10% was used for each layer of the grid. This value is similar to the systematic component used for HCFC-22 by Prignon et al. (2019). The correlation width of the HFC-134a profile was assumed to be 3 km. The random uncertainty for the SZA was set to ±0.1°, while the systematic uncertainty was assumed to be ±0.03°. The relative systematic uncertainties of the spectroscopic parameters of HFC-134a (line intensity, temperature, and pressure) were set to 5%, according to the empirical pseudo-linelist produced by G. C. Toon.

The mean total random and systematic uncertainties are $9.8 \pm 2.8\%$ and $8.9 \pm 1.5\%$, respectively. The error budgets for 5 years before and after 2014 were also calculated. For 2009, the total random and systematic uncertainties are $14.5 \pm 3.8\%$ and $13.3 \pm 3.0\%$, respectively, while for 2019, they are $8.5 \pm 2.5\%$ and $7.1 \pm 1.1\%$, respectively. These results highlight the challenge to retrieve HFC-134a from ground-based FTIR solar absorption spectra in the early 2000s, while the atmospheric load only started to develop in the mid-1990s. Consequently, we decided to show here the HFC-134a total columns above Jungfraujoch from 2004 to 2022, spanning the same period as the ACE dataset. As shown in Table 4.1, the random error is mainly determined by the uncertainties of the measurement, the temperature, and the interfering species, while the systematic error is mainly influenced by the uncertainty of the temper-

	Relative uncertainty (%)	
Error type and source	**Mean**	**Standard deviation**
Random components		
Measurement	6.7	2.2
Temperature	4.3	1.0
SZA	0.8	0.3
Interfering species	5.5	1.9
Smoothing	1.0	0.1
Retrieval parameters	0.3	0.2
Total random	**9.8**	**2.8**
Systematic components		
HFC-134a line intensity	4.99	0.01
Temperature	7.1	1.9
SZA	0.3	0.1
Total systematic	**8.9**	**1.5**

Table 4.1. Mean relative errors (%) for one year (2014) concerning the HFC-134a total column retrievals for the Jungfraujoch station.

ature and the spectroscopic parameters. The other sources of uncertainty only contribute less than 1% to the total error (random and systematic). These relative uncertainties are determined by dividing the measurement uncertainty by the absolute total column value.

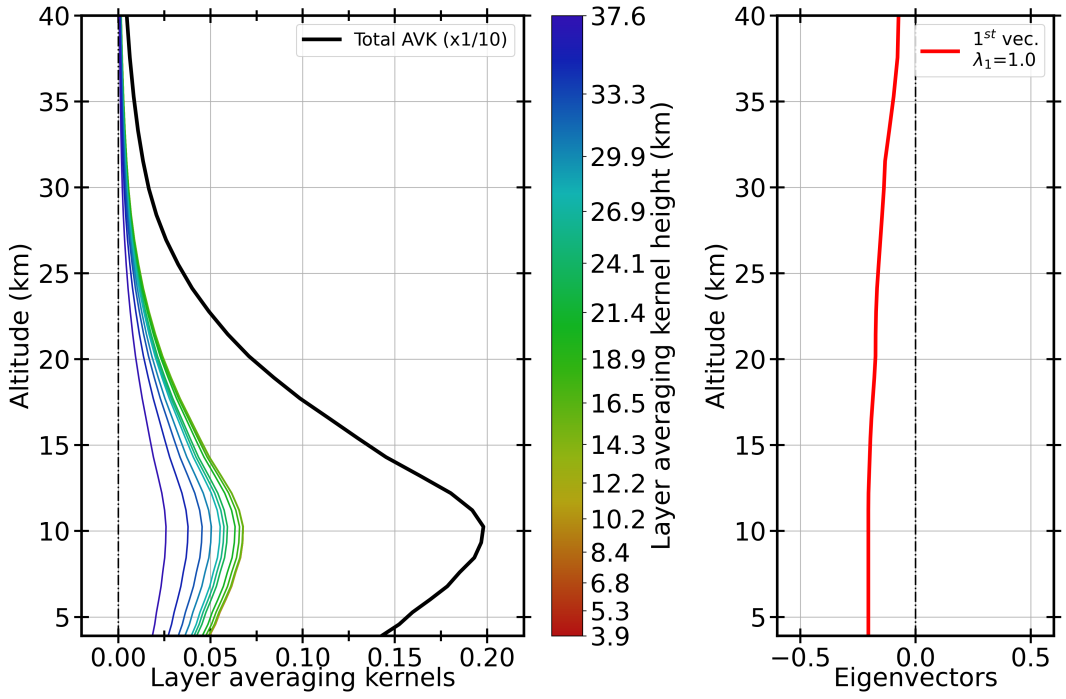

Figure 4.4. Mean layer averaging kernels and first eigenvector. The left panel shows the mean layer averaging kernels for mixing ratios computed for the spectra recorded at the Jungfraujoch station from January 2007 to December 2009. The ticks on the colour bar are the individual layer averaging kernels represented in the graph. The first eigenvector is shown in the right panel and its eigenvalue is 1.0.

The mean layer averaging kernels provide the information content of the retrieval processing required to characterise the relative weighting between the *a priori* and the true vertical profiles to the retrieved vertical distribution (Rodgers, 2000). Figure 4.4 shows the mean layer averaging kernels (left panel) and the first eigenvector (right panel) calculated for the spectra recorded above the Jungfraujoch station during three years (2007 – 2009). The thick black line indicates the total column averaging kernel scaled by 0.1 (from 3.58 km, the station altitude, up to 40 km), while the coloured lines show the different individual layer averaging kernels, indicated by the vertical colour bar. The degrees of freedom for signal (DOFS) inform on how much information can be extracted from the retrievals. The mean DOFS of the entire time series is 1.0, so the retrievals provide one useful piece of information. The 100% of the information characterising the troposphere comes from the retrievals and not from the assumed *a priori*, as indicated by the first eigenvalue (λ_1 = 1.0).

We also analysed the effects of the misalignment of the Bruker IFS-120HR spectrometer between July 2011 and December 2012, because the retrieved total columns presented a discontinuity in this period, with a local maximum that was not observed in the other datasets. For this purpose, we retrieved an effective apodization. Nevertheless, this perturbation did not show consistent effects on the retrieved total columns. This effect was also observed in the partial columns of other species retrieved at the Jungfraujoch station during the same period, such as HCFC-22 (Prignon et al., 2019).

4.4 Results and discussion

In this section, we present the HFC-134a time series obtained after the retrieval of the total columns, as well as the trend analyses and seasonality. Since these are the first HFC-134a retrievals from ground-based FTIR solar absorption spectra, we compare our results with other three independent datasets, described in Section 4.2.

4.4.1 Time series of HFC-134a above the Jungfraujoch NDACC site

With the aim of keeping good spectra, we did not consider data with a fit RMS higher than 0.6 (considering that the mean fit RMS is 0.3). We also removed data from July 2011 to December 2012 due to the low reliability of the retrievals, as explained in the section above. Before filtering, we had 5019 spectra for the whole time series (January 2004 – December 2022), i.e. 1542 daily measurements. After filtering, we retained specifically 1382 daily observations (196 months). To use the same units and to easily compare the four independent time series, we show here the FTIR dry air mole fractions (xHFC-134a) instead of the retrieved total columns. These xHFC-134a were determined by dividing the HFC-134a total columns by the dry air pressure column (DPC), which can be obtained as described in Barthlott et al. (2015) and Pardo Cantos et al. (2022). The water vapour columns used to calculate the xHFC-134a were obtained using a dedicated retrieval strategy for water vapour, described by Sussmann et al. (2009).

4.4.2 Comparison with independent datasets

Figure 4.5 shows the annual means of the four different datasets from January 2004 to December 2022. As orange dots, the xHFC-134a from FTIR measurements at the Jungfraujoch station; in blue up-pointing triangles, the HFC-134a surface volume mixing ratios derived from TOMCAT model simulations; in purple squares, the HFC-134a VMRs from ACE-FTS for a latitude band between 40 and 50°N (centered around the Jungfraujoch station location) and averaged over an altitude range between 5.5 and 15.5 km; finally, the green down-pointing triangles show the *in situ* HFC-134a mole fractions measured at the Jungfraujoch station within the AGAGE network. The error bars show the standard deviation around the annual means. The mean relative standard deviations are 9.5% for the FTIR annual xHFC-134a averages, commensurate with the random uncertainty shown in Table 4.1; 2.3% for the annual means of the TOMCAT model surface VMRs; 10.9% for the ACE-FTS HFC-134a VMRs; and 3.4% for the *in situ* baseline mole fractions.

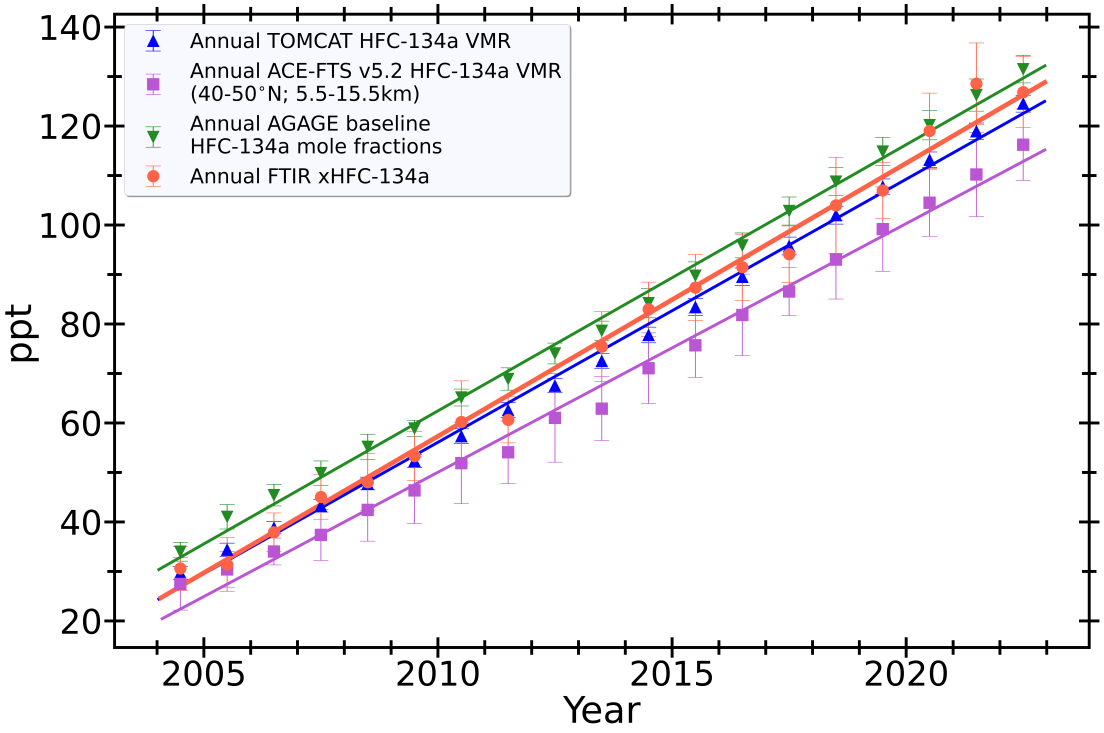

Figure 4.5. Atmospheric HFC-134a annual means derived from the different datasets. As orange dots, the Jungfraujoch FTIR xHFC-134a data; as blue up-pointing triangles, the TOMCAT HFC-134a lower-most model level VMRs; as purple squares, the ACE-FTS L2 v5.2 HFC-134a VMRs; and as green down-pointing triangles, the *in situ* baseline HFC-134a mole fractions at Jungfraujoch. The vertical error bars depict one standard deviation. The respective linear trends are indicated by the straight lines.

For the FTIR time series, some periods must be emphasised. First, the 2021 annual mean is higher because the spectrometer was out of operation from January to May 2021, so this annual mean only includes the second half of the year, when the atmospheric HFC-134a content is higher, as shown in Figure 4.6. In addition, the quality of the spectra from 2021 is less accurate as the maintenance of the Bruker IFS-120HR spectrometer could not be performed frequently enough due to travel restrictions during the COVID-19 pandemic. The second pe-

riod to note extends from July 2011 to December 2012. This one-and-a-half-year data was suppressed because of the low quality of the retrievals during this period, as explained in Section 4.3. Consequently, the 2011 xHFC-134a annual mean is slightly lower because we only considered the first half of the year, when the atmospheric HFC-134a burden is lower. The FTIR and TOMCAT model time series are in good quantitative agreement. In fact, the mean relative systematic difference between TOMCAT VMRs and FTIR xHFC-134a monthly means is 5.3%, which is covered by the systematic uncertainty of the retrievals shown in Table 4.1. This mean relative systematic difference between the two datasets was determined by dividing the difference of the mean TOMCAT and FTIR values by the mean TOMCAT VMR. While the two datasets almost overlap for the earlier years, they diverge slightly later on. Still, the respective trends are consistent when the associated statistical uncertainties are considered. The ACE-FTS time series seems to be down shifted compared to the FTIR series, while the *in situ* baseline HFC-134a time series is higher than the FTIR time series. However, we should not forget that the ACE-FTS observations mainly represent the upper troposphere, as only a subset of the measured profiles reached down to 5.5 km. While the *in situ* measurements are representative of the surface mole fractions, the FTIR observations are less sensitive in the first few kilometers of the atmosphere, and they reach a maximum around 10 km to then decrease rapidly above, as shown in Figure 4.4. The differences between the four datasets may have several causes including the time required for vertical transport and mixing. The systematic uncertainty reported in Table 4.1 could also explain part of the bias between the *in situ* and the remote sensing datasets.

4.4.3 Trend analyses and seasonality

We analysed the linear trend of the entire FTIR time series (2004 – 2022). The trends and their uncertainties were estimated using the autoregressive wild bootstrap method developed by Friedrich et al. (2020b), with a 95% confidence interval. The absolute and relative linear trends are gathered in Table 4.2. These trends were calculated using the monthly means, even if only the annual means are shown in Figure 4.5 for reasons of clarity. The relative trends were calculated by dividing the absolute trend by the mean value (dry air mole fractions, or VMRs, or baseline mole fractions) of the whole time series.

Source	Trend (ppt yr^{-1})	Relative trend (% yr^{-1})
xHFC-134a FTIR	5.52 ± 0.12	7.34 ± 0.16
TOMCAT surface VMR	5.32 ± 0.04	7.12 ± 0.05
ACE-FTS v5.2 HFC-134a VMR	5.02 ± 0.11	7.29 ± 0.16
AGAGE baseline mole fractions	5.38 ± 0.04	6.61 ± 0.05

Table 4.2. Relative and absolute trends derived for the FTIR xHFC-134a at Jungfraujoch, the TOMCAT surface HFC-134a VMRs, the AGAGE HFC-134a mole fractions at Jungfraujoch, and the ACE-FTS HFC-134a VMRs, for the 2004 – 2022 period.

We found that the HFC-134a atmospheric concentration according to the FTIR measurements above the Jungfraujoch site increased by 5.52 ± 0.12 ppt per year, or a relative increase of 7.34 ± 0.16% per year. Regarding the other time series, a rise of 7.12 ± 0.05% per year (TOMCAT), 7.29 ± 0.16% per year (ACE-FTS), and 6.61 ± 0.05% per year (*in situ*) was ob-

served. Therefore, the FTIR, TOMCAT, and ACE relative trends agree when we weigh the uncertainties. The *in situ* relative trend is slightly lower by about 9%.

Other studies have already analysed the atmospheric HFC-134a trends (Montzka et al., 2015; Fernando et al., 2019; Harrison et al., 2021). The Scientific Assessment of Ozone Depletion (Liang et al., 2022) reports an increase in global HFC-134a from 85.5 ± 0.3 ppt in 2016 to 109.8 ± 0.2 ppt in 2020 in the upper troposphere, which corresponds to an increase of around 5 ppt yr^{-1}. A study by Bernath et al. (2021) describes a global trend for the ACE-FTS Level 2 v4.1 HFC-134a retrievals (2004 – 2020) of 5.71 ± 0.07 ppt per year, that is $6.86 \pm 0.22\%$ per year, which is in line with our results.

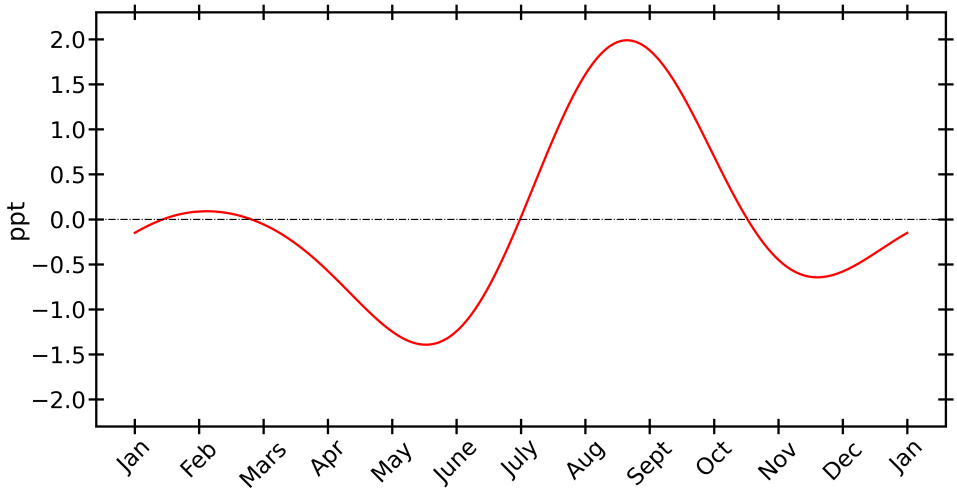

Figure 4.6. Seasonal cycle of xHFC-134a as derived from the FTIR observations at the Jungfraujoch station. The minimum atmospheric HFC-134a is at the end of spring, while the maximum occurs at the end of the summer.

Finally, we analysed the seasonal cycle of xHFC-134a (Figure 4.6), which exhibits minimum abundances at the end of spring (May-June), and maximum load at the end of summer (August-September). A local minimum is present in November, and a local maximum in February. It is important to note that the seasonal cycle peak-to-peak amplitude is relatively weak, around 3.5 ppt, that is 4.5%. This behaviour is also captured by the TOMCAT seasonal cycle, where the maximum occurs in early September and the minimum in early April. The annual cycle of the *in situ* baseline HFC-134a mole fractions at Jungfraujoch shows a minimum at the end of winter and a maximum load during the spring and summer. These *in situ* baseline measurements can account for the regional emissions and their main sink is oxidation by the OH radical. However, the FTIR measurements are also influenced by the tropopause height and the atmospheric circulation. Above the Jungfraujoch site, the mean tropopause height is around 11.3 ± 2.2 km (2σ) (Zander et al., 2010; Gardiner et al., 2008). On the one hand, the tropopause above Jungfraujoch sinks in fall and winter and reaches a minimum height at the beginning of March. On the other hand, the tropopause above the station rises in spring and summer and gets a maximum height in mid-August (Zander et al., 2010).

4.5 Summary and conclusions

In this study, we described the retrieval strategy we developed for HFC-134a from ground-based FTIR solar absorption spectra recorded at the high-altitude dry Jungfraujoch station. This was the first attempt to retrieve HFC-134a within the NDACC network. HFC-134a is the most abundant HFC in the atmosphere and the preferred substitute to CFC-12 as a refrigerant. Even though HFCs do not directly affect stratospheric ozone, they are very potent greenhouse gases, which is why they were included in the Kigali Amendment to the Montreal Protocol.

We chose the 1104.300 – 1105.585 cm^{-1} spectral window for the retrievals, in which the HFC-134a feature typically represents only 1% of the absorption depth. We chose this window as the water vapour absorption is not very intense, which is an essential point to consider in the cases where the absorption of the target molecule is weak. The main interfering species in this window is ozone and its absorption lines are well defined. The mean DOFS is equal to 1.0, which allows the determination of a single piece of information.

The trend of xHFC-134a was analysed from January 2004 to December 2022. The previous years were not analysed because the FTIR retrievals in early 2000 are quite challenging for this molecule, as demonstrated in the error budget analysis section (Section 4.3.2). The obtained FTIR HFC-134a time series was compared to three other independent datasets: TOMCAT model simulations, ACE-FTS satellite observations, and AGAGE *in situ* surface measurements also performed at the Jungfraujoch station. The calculated trends for the whole time series showed an increase of 7.34 ± 0.16% per year (FTIR), 7.12 ± 0.05% per year (TOMCAT), 7.29 ± 0.16% per year (ACE) and 6.61 ± 0.05% per year (*in situ*). The effects of the Kigali Amendment are not yet visible, as it only came into force in 2019. The seasonal cycle of HFC-134a over the Jungfraujoch showed a maximum atmospheric load at the end of summer and a minimum at the end of spring, which could be driven by the tropopause height.

As reported in the Scientific Assessment of Ozone Depletion (2022), global top-down derived emissions of HFCs show a significant gap with the total HFC emissions reported by Annex I countries to the UNFCCC in 2019. Understanding these differences between the reported and estimated emissions requires continuous atmospheric monitoring in support to the Kigali Amendment. The strategy presented in this manuscript has been validated by comparison with three other independent datasets. It could therefore be implemented at other NDACC sites to achieve quasi-global coverage of this species using the FTIR remote sensing technique.

Chapter 5

Conclusions and perspectives

Halogenated compounds, such as chlorofluorocarbons (CFCs), hydrochlorofluorocarbons (HCFCs), and hydrofluorocarbons (HFCs), have played a major role in both stratospheric ozone depletion and climate change. While the Montreal Protocol has successfully phased out most CFC emissions, contributing to the gradual recovery of the ozone layer, HFCs, introduced as substitutes for CFCs and HCFCs, have emerged as potent greenhouse gases. Although their impact on ozone depletion is negligible, their significant global warming potentials have led to their regulation under the Kigali Amendment. Understanding the atmospheric evolution of these compounds requires high-quality, long-term global measurements to detect trends, identify possible unreported emissions, such as to assess the effectiveness of international policies and potentially adapt them.

In this context, this research focuses on retrieving and analysing the long-term time series of halogenated gases from ground-based Fourier Transform Infrared (FTIR) spectra. At the beginning of this thesis, striking observations were reported: the atmospheric decline of CFC-11 appeared to be slowing down due to undeclared emissions. Would it be possible to observe this trend change using ground-based FTIR measurements from a high-altitude remote site (Jungfraujoch station)? Could this change also be detected at another NDACC station located at a similar latitude but at lower altitude in the Southern Hemisphere (Lauder station)? Given that CFC-11 is one of the two most significant CFCs, reinforcing its monitoring was clearly essential.

Another challenge then arose: could we use ground-based FTIR observations and retrieve atmospheric HFC-134a (the most abundant HFC), in order to support the Kigali Amendment to the Montreal Protocol, despite its atmospheric concentration being only half that of CFC-11? What would be the optimal spectral window to minimise interference from other absorbing species?

This thesis outlines the steps and developments undertaken to achieve these objectives. These efforts contribute to enhancing observational capabilities within the NDACC network and complement existing measurement techniques, ensuring a more comprehensive understanding of the atmospheric evolution of these gases. The following conclusions summarise the main findings of this research, providing a guide for expanding the list of target molecules within the NDACC network to achieve near-global coverage of these species using FTIR remote sensing. Additionally, some perspectives and potential future work are discussed.

5.1 Main conclusions

This research demonstrates the crucial role of ground-based FTIR remote sensing in monitoring atmospheric halogenated compounds, in particular CFC-11 and HFC-134a. The retrieval and trend analysis of these species at various NDACC stations confirm the success of international regulations, such as the Montreal Protocol and its amendments, in reducing production and use of ozone-depleting substances and potent greenhouse gases.

The first study in this thesis focused on the long-term evolution of CFC-11, in particular the slowdown in its atmospheric decline during the second decade of the 21st century. The retrieved total column using high-resolution FTIR solar spectra from Jungfraujoch was compared to total columns retrieved from spectra recorded at Lauder, Jungfraujoch's counterpart station in the Southern Hemisphere. For the first time, a harmonised CFC-11 time series for Jungfraujoch, spanning from June 1986 to December 2020, was presented, illustrating with a enhanced precision the atmospheric evolution of this molecule and the impact of the Montreal Protocol over nearly 35 years. Additionally, the first FTIR CFC-11 time series from Lauder was introduced, enabling interhemispheric comparisons. This study focused on the post-2000 decrease in CFC-11 to analyse the slowdown in its decline reported by Montzka et al. (2018) from 2012 onward. The trend analysis showed good agreement with model predictions and *in situ* observations, revealing a slowdown in CFC-11 decline starting in 2011 in the Northern Hemisphere (NH) and in 2014 in the Southern Hemisphere (SH). This delay aligns with the interhemispheric transit time, considering uncertainties, from the NH, where most emissions occur, to the SH. Before the slowdown, CFC-11 decreased by approximately 1% (0.8%) per year in the NH (SH), while post-2011 (NH) and post-2014 (SH), the decline slowed to around 0.6% (0.5%) per year.

The second study in this thesis involved the development of a retrieval strategy for HFC-134a from ground-based FTIR solar spectra at the Jungfraujoch station, making it the first retrievals of that species within the NDACC network. The chosen spectral window allows to detect this weak absorption since no water vapour lines are present, making possible to extend this strategy to more humid sites. The HFC-134a trend from 2004 to 2022 showed an annual increase of approximately 7%, consistent across all datasets used for comparison, including FTIR observations, TOMCAT model simulations, ACE-FTS satellite data, and AGAGE *in situ* measurements.

These studies confirm the effectiveness of the Montreal Protocol in reducing CFC-11 emissions. Moreover, they demonstrate the capability of the FTIR technique to detect harmful atmospheric compounds even when their concentrations and/or IR absorption are relatively low. In the case of HFCs, their atmospheric concentrations continue to rise, as evidenced by the HFC-134a trends. The effects of the Kigali Amendment should become apparent in the coming years. Furthermore, discrepancies between reported and observed emissions highlight the ongoing need for continuous atmospheric monitoring. The validated FTIR retrieval strategies presented in this thesis can be applied across other NDACC sites, contributing to a more comprehensive global assessment of halogenated gases and supporting policy enforcement efforts. Therefore, continuous monitoring remains crucial to detecting rogue emissions and protecting the Earth's atmosphere in the dual fight: restoring the ozone layer and mitigating global warming.

5.2 Perspectives

This research has addressed several important questions for both the scientific community and the general public. However, science is constantly evolving, and new questions frequently arise. In this section, I outline potential future directions for this project, based on my experience and aspirations.

Is it possible to expand HFC-134a retrievals to other NDACC stations?

The first proposed continuation of this work is already in progress. The retrieval strategy for HFC-134a total columns has proven to be successful and applicable to other NDACC stations, as the selected spectral window is free from water vapour absorption. As a result, several NDACC research groups have expressed interest in applying this "recipe" to spectra recorded at their stations. In response to these requests, I reached out to additional research groups to ensure broad global coverage and enable interhemispheric comparisons. The stations currently performing HFC-134a retrievals are listed in Table 5.1. Expanding these retrievals will enhance our understanding of HFC-134a's atmospheric behaviour and enable more effective monitoring of its evolution, given that it is the most abundant HFC in Earth's atmosphere.

Station	Region	Lat (°)	Lon (°)	Alt (m)	People in charge of HFC-134a retrievals
Arrival Heights	Antarctica	-77.83	166.67	184	Dan Smale
Tsukuba	Japan	36.05	140.13	31	Hideaki Nakajima
Izaña	Spain	28.30	-16.48	2367	Omaira García Rodríguez
Eureka	Canada	80.05	-86.42	610	Petra Duff & Beatriz Herrera Gutierrez

Table 5.1. Stations of the NDACC-IRWG where HFC-134a retrievals are in progress.

Furthermore, retrieving HFC-134a at additional NDACC sites could potentially allow inverse modelling for emission estimates. Increasing the number of observations from different locations improves both accuracy and reliability. A broader geographic distribution of measurements enhances spatial resolution, improving the identification of emission sources, while frequent observations refine temporal resolution, allowing for better tracking of emission trends over time.

Although large-scale implementation may not be feasible in the immediate future, continuous monitoring of HFC-134a remains essential to supporting the Kigali Amendment regulations and identifying potential undeclared production. Since the Kigali Amendment entered into force in 2019, several more years of data collection will be required before any changes in trends become observable using ground-based FTIR measurements.

Can we take advantage of using PROFFIT for the retrieval of new species?

During a two-weeks research stay in Tenerife in 2024, we initiated HFC-134a retrievals using PROFFIT. Similar to SFIT4, PROFITT is an algorithm used to retrieve atmospheric trace gas concentrations from spectral measurements and is employed by several NDACC groups, including the Izaña team. This collaboration sparked new ideas and perspectives. In addition

to implementing HFC-134a retrievals at Izaña, as discussed earlier, we considered conducting a detailed comparison between SFIT4 and PROFFIT to better understand the differences between these algorithms. This would also allow us to implement certain retrieval strategies in PROFFIT, taking advantage of its capability to use cross sections directly, unlike SFIT4, which relies on calculated pseudo-linelists.

At the beginning of my PhD, I learned to use SFIT4 by performing retrievals of CFC-12. These retrievals have been refined by our team and have also been used by the University of Bremen team for historical time series of CFC-12 at Jungfraujoch (with a manuscript to be submitted soon). Given the high precision of CFC-12 measurements, this molecule could serve as an excellent test case for comparing retrievals using PROFFIT and SFIT4 and for evaluating the impact of using pseudo-lines versus cross sections. These tests could open the possibility for retrieving total columns of other molecules, such as HFC-125 (CF_3CHF_2) and HFC-32 (CH_2F_2), for which pseudo-linelists are unavailable and laboratory cross section measurements are required instead. This could also allow to continue the validation of ACE-FTS measurements using ground-based FTIR observations.

Can we detect the expected decay of CFC-11 after 2018?

As reported by Montzka et al. (2021) and Park et al. (2021), the global decline rate of atmospheric CFC-11 concentrations after 2018 returned to levels observed during the 2008 – 2012 period, indicating that undeclared production had decreased or even ceased (Montzka et al., 2018; Rigby et al., 2019). These changes in the decay rate highlight the importance of continuous monitoring in detecting and reporting rogue emissions, thereby supporting international policies.

Although the FTIR technique was unable to detect this post-2018 trend change in Pardo Cantos et al. (2022), since the CFC-11 time series at Jungfraujoch and Lauder were analysed until December 2020, new retrievals and analyses are now necessary. At the time of that publication, no significant trend change was observable. However, we now have an additional 4 – 5 years of observations. Therefore, a reanalysis of the full time series will be needed to determine whether FTIR observations can detect this trend change, providing valuable ground-based complementary monitoring of this harmful atmospheric species.

What if we were interested in atmospheric compounds other than halogenated gases?

The skills and expertise acquired during this doctoral research will enable me to study a wide range of atmospheric molecules, not limited to those regulated by the Montreal Protocol but also those related to other problematics, such as air pollution. One example is acetone, a volatile organic compound (VOC) that contributes to the formation of tropospheric ozone, a key component of smog.

Another interesting question involves investigating the impact of nitrogen-containing atmospheric gases on stratospheric ozone. As the atmospheric abundance of chlorine-containing gases continues to decline due to the success of the Montreal Protocol, nitrogen-containing gases could become more influential in stratospheric ozone depletion (Ravishankara et al., 2009; Chipperfield, 2009).

Nitrogen-containing gases, such as ammonia (NH_3) and nitrogen oxides (NO_x), are major contributors to air pollution and play critical roles in atmospheric chemistry and environmental processes. These gases are widely monitored due to their effects on air quality, human health, and ecosystems. However, an important question remains: could nitrogen-bearing gases other than N_2O contribute to the accumulation of nitrogen in the stratosphere? Exploring this possibility could provide valuable insights into future challenges for stratospheric ozone protection.

Appendix A

List of NDACC-IRWG stations

Station	Lat (°)	Lon (°)	Alt (m)	Region	Managed by
Eureka	80.05	-86.42	610	Canada	Department of Physics, University of Toronto (Canada)
Ny Ålesund	78.92	11.93	15	Norway	Institute of Environmental Physics, University of Bremen (Germany)
Thule	76.53	-68.74	30 – 220	Greenland	UCAR, Boulder (USA)
Kiruna	67.84	20.41	419	Sweden	Institute of Space Physics, Kiruna (Sweden)
Søndre Strømfjord	66.99	-50.95	180 – 300	Greenland	DCC & DMI, Copenhagen (Denmark)
Harestua	60.20	10.80	596	Norway	IASB/BIRA, Brussels (Belgium)
St. Petersburg	59.90	29.80	20	Russia	Faculty of Physics, St. Petersburg State University (Russia)
Bremen	53.10	8.80	27	Germany	Institute of Environmental Physics, University of Bremen (Germany)
Paris	48.97	2.37	60	France	Sciences and Engineering Faculty, Sorbonne Université, Paris (France)
Zugspitze	47.42	10.98	2964	Germany	IMK-IFU, Garmisch-Partenkirchen (Germany)
Jungfraujoch	46.55	7.98	3580	Switzerland	Department AGO, University of Liège (Belgium)
Toronto	43.66	-79.40	174	Canada	Department of Physics, University of Toronto (Canada)
Rikubetsu	43.46	143.77	380	Japan	Solar-Terrestrial Environment Lab., Nagoya University (Japan)
Boulder	39.99	-105.26	1634	USA	NOAA ESRL, Global Monitoring Laboratory, Colorado (USA)
Tsukuba	36.05	140.13	31	Japan	National Institute for Environmental Studies, Tsukuba (Japan)
Table Mountain Facility	34.4	-117.7	2300	USA	JPL, Wrightwood (USA)
Hefei	31.90	117.17	29	China	University of Science and Technology of China, Hefei (China)
Izaña	28.30	-16.48	2367	Spain	AEMet, Tenerife (Spain)

Station	Lat (°)	Lon (°)	Alt (m)	Region	Managed by
Mauna Loa	19.54	-155.58	3397	USA	NOAA ESRL, Global Monitoring Laboratory, Colorado (USA)
Altzomoni	19.12	-98.66	3985	Mexico	ICAyCC, Universidad Nacional Autónoma de México (Mexico)
Paramaribo	5.75	-55.2	23	Suriname	Meteorological Service of Suriname, Paramaribo (Suriname)
St. Denis	-20.90	55.50	85	France	LACy, Reunion Island University (France)
Maido	-21.10	55.40	2155	France	LACy, Reunion Island University (France)
Wollongong	-34.41	150.88	30	Australia	Department of Chemistry, University of Wollongong (Australia)
Lauder	-45.04	169.68	370	NZ	NIWA, Lauder (New Zealand)
Arrival Heights	-77.83	166.67	184	Antarctica	NIWA, Lauder (New Zealand)

Table A.1. Active stations of the NDACC-IRWG (March 2025). Station names, their coordinates (latitude, longitude, and altitude above mean sea level), the regions where they are located, and the scientific groups operating each FTIR spectrometer. Positive latitudes indicate stations in the Northern Hemisphere, while negative latitudes correspond to stations in the Southern Hemisphere. Positive longitudes represent locations east of the Prime Meridian, while negative longitudes indicate locations west of it. The acronyms of the different laboratories and institutes are listed in the *Glossary of Acronyms* at the beginning of this manuscript (`https://ndacc.larc.nasa.gov/`). See Figure 2.3.

Appendix B

List of AGAGE stations

Station	Lat (°)	Lon (°)	Alt (m)	Region
Zeppelin	78.91	11.89	474	Svalbard
Mace Head	53.33	-9.90	8	Ireland
Tacolneston	52.52	1.14	185	UK
Taunus	50.22	8.45	825	Germany
Jungfraujoch	46.55	7.98	3571	Switzerland
Monte Cimone	44.19	10.70	2165	Italy
Cape Ochi-ishi	43.16	145.50	42	Japan
Trinidad Head	41.05	-124.15	107	USA
Gosan	33.29	126.16	72	South Korea
Dongtan	31.52	121.98	3	China
Hateruma	24.06	123.81	10	Japan
Xichong	22.48	114.56	3	China
Ragged Point	13.17	-59.43	30	Barbados
Mt. Mugogo	-1.59	29.57	2590	Rwanda
Cape Matatula	-14.25	-170.56	42	American Samoa
Kennaook/Cape Grim	-40.68	144.69	94	Australia

Table B.1. Active stations of the AGAGE network (March 2025). The table lists the station names, their coordinates (latitude, longitude, and altitude above mean sea level), and the regions where they are located. Positive latitudes indicate stations in the Northern Hemisphere, while negative latitudes correspond to stations in the Southern Hemisphere. Similarly, positive longitudes represent locations east of the Prime Meridian, while negative longitudes indicate locations west of it (`https://www-air.larc.nasa.gov/missions/agage/`). See Figure 2.10.

Appendix C

List of publications

Mahieu, E., Flock, O., Notholt, J., Palm, M., **Pardo Cantos, I.**, Prignon, M., Roland, G., Servais, C., and Verma, A. (2019). Surveillance à long terme de l'atmosphère terrestre à la station du Jungfraujoch. *Bulletin de la Société Royale des Sciences de Liège*, 88, 31-41. https://doi.org/10.25518/0037-9565.9136.

Mahieu, E., Fischer, E. V., Franco, B., Palm, M., Wizenberg, T., Smale, D., Clarisse, L., Clerbaux, C., Coheur, P.-F., Hannigan, J. W., Lutsch, E., Notholt, J., **Pardo Cantos, I.**, Prignon, M., Servais, C., and Strong, K. (2021). First retrievals of peroxyacetyl nitrate (PAN) from ground-based FTIR solar spectra recorded at remote sites, comparison with model and satellite data. *Elementa: Science of the Anthropocene*, 9 (1). https://doi.org/10.1525/elementa.2021.00027.

Pardo Cantos, I., Mahieu, E., Chipperfield, M. P., Smale, D., Hannigan, J. W., Friedrich, M., Fraser, P., Krummel, P., Prignon, M., Makkor, J., Servais, C., and Robinson, J. (2022). Determination and analysis of time series of CFC-11 (CCl_3F) from FTIR solar spectra, *in-situ* observations, and model data in the past 20 years above Jungfraujoch (46°N), Lauder (45°S), and Cape Grim (40°S) stations. *Environmental Science: Atmospheres*, 2(6), 1487-1501. https://doi.org/10.1039/d2ea00060a.

Zeng, X., Wang, W., Liu, C., Shan, C., Xie, Y., Wu, P., Zhu, Q., Zhou, M., De Mazière, M., Mahieu, E., **Pardo Cantos, I.**, Makkor, J., and Polyakov, A. (2022). Retrieval of atmospheric CFC-11 and CFC-12 from high-resolution FTIR observations at Hefei and comparisons with other independent datasets. *Atmospheric Measurement Techniques*, 15 (22), 6739-6754. https://doi.org/10.5194/amt-15-6739-2022.

Pardo Cantos, I., Mahieu, E., Chipperfield, M. P., Servais, C., Reimann, S., and Vollmer, M. K. (2024). First HFC-134a retrievals from ground-based FTIR solar absorption spectra, comparison with TOMCAT model simulations, *in-situ* AGAGE observations, and ACE-FTS satellite data for the Jungfraujoch station. *Journal of Quantitative Spectroscopy and Radiative Transfer*, 318. https://doi.org/10.1016/j.jqsrt.2024.108938.

Makkor, J., Palm, M., **Pardo Cantos, I.**, Buschmann, M., Mahieu, E., Wang, Z., Chipperfield, M., Notholt, J. (2025). First measurements of CFC-12 in 1951 at Jungfraujoch and comparison to current measurements and atmospheric models. *Manuscript to be submitted to GRL.*

Bibliography

Abalos, M., Polvani, L., Calvo, N., Kinnison, D., Ploeger, F., Randel, W., and Solomon, S. (2019). New insights on the impact of ozone-depleting substances on the Brewer-Dobson circulation. *Journal of Geophysical Research: Atmospheres*, 124(5):2435–2451. https://doi.org/10.1029/2018JD029301.

Ahrens, C. D. (2001). *Essentials of meteorology: an invitation to the atmosphere. 6th ed.* Brooks/Cole/Thomson Learning Australia.

Andrews, D. G. (2010). *An introduction to atmospheric physics*. Cambridge University Press.

Barthlott, S., Schneider, M., Hase, F., Wiegele, A., Christner, E., González, Y., Blumenstock, T., Dohe, S., García, O., Sepúlveda, E., et al. (2015). Using XCO_2 retrievals for assessing the long-term consistency of NDACC/FTIR data sets. *Atmospheric Measurement Techniques*, 8(3):1555–1573. https://doi.org/10.5194/amt-8-1555-2015.

Bernath, P., Crouse, J., Hughes, R., and Boone, C. (2021). The Atmospheric Chemistry Experiment Fourier Transform Spectrometer (ACE-FTS) version 4.1 retrievals: Trends and seasonal distributions. *Journal of Quantitative Spectroscopy and Radiative Transfer*, 259:107409. https://doi.org/10.1016/j.jqsrt.2020.107409.

Bernath, P. F., McElroy, C. T., Abrams, M., Boone, C. D., Butler, M., Camy-Peyret, C., Carleer, M., Clerbaux, C., Coheur, P.-F., Colin, R., et al. (2005). Atmospheric Chemistry Experiment (ACE): mission overview. *Geophysical Research Letters*, 32(15). https://doi.org/10.1029/2005GL022386.

Bernath, P. F., Steffen, J., Crouse, J., and Boone, C. D. (2020). Sixteen-year trends in atmospheric trace gases from orbit. *Journal of Quantitative Spectroscopy and Radiative Transfer*, 253:107–178. https://doi.org/10.1016/j.jqsrt.2020.107178.

Berrisford, P., Dee, D., Poli, P., Brugge, R., Fielding, K., Fuentes, M., Kållberg, P., Kobayashi, S., Uppala, S., and Simmons, A. (2011). The ERA-Interim archive version 2.0. ERA report series 1, ECMWF. *ECMWF Publications*. https://www.ecmwf.int/en/elibrary/73682-era-interim-archive-version-20.

Bohren, C. F. and Clothiaux, E. E. (2006). *Fundamentals of atmospheric radiation: an introduction with 400 problems*. John Wiley & Sons Ldt.

Bönisch, H., Engel, A., Birner, T., Hoor, P., Tarasick, D. W., and Ray, E. A. (2011). On the structural changes in the Brewer-Dobson circulation after 2000. *Atmospheric Chemistry and Physics*, 11(8):3937–3948. https://doi.org/10.5194/acp-11-3937-2011.

Boone, C., Bernath, P., and Lecours, M. (2023). Version 5 retrievals for ACE-FTS and ACE-imagers. *Journal of Quantitative Spectroscopy and Radiative Transfer*, 310:108749. https://doi.org/10.1016/j.jqsrt.2023.108749.

Boone, C., Jones, S., and Bernath, P. (2019). Data usage guide and file format description for ACE-FTS level 2 data version 4.0 ASCII format. https://g-624536.53220.5898.data.globus.org/1/published/publication_286/submitted_data/ACE-SOC-0033-ACE-FTS_ascii_data_usage_and_fileformat_for_v4.0.pdf; Accessed: 2021-05-30.

Brasseur, G. P. and Solomon, S. (2005). *Aeronomy of the middle atmosphere: Chemistry and physics of the stratosphere and mesosphere*, volume 32. Springer Science & Business Media.

Brewer, A. (1949). Evidence for a world circulation provided by the measurements of helium and water vapour distribution in the stratosphere. *Quarterly Journal of the Royal Meteorological Society*, 75(326):351–363. https://doi.org/10.1002/qj.49707532603.

Bullister, J. L. (2015). Atmospheric Histories (1765–2015) for CFC-11, CFC-12, CFC-113, CCl_4, SF_6 and N_2O. *Carbon Dioxide Information Analysis Center, Oak Ridge National Laboratory, US Department of Energy, Oak Ridge, Tennessee*. https://doi.org/10.3334/CDIAC/otg.CFC_ATM_Hist_2015.

Burkholder, J., Hodnebrog, O., et al. (2022). Annex: summary of abundances, lifetimes, ODPs, REs, GWPs, and GTPs. *Scientific Assessment of Ozone Depletion*, pages 435–492. https://csl.noaa.gov/assessments/ozone/2022/.

Butchart, N. (2014). The Brewer-Dobson circulation. *Reviews of geophysics*, 52(2):157–184. https://doi.org/10.1002/2013RG000448.

Chapman, S. (1930). A theory of upper-atmospheric ozone. *Mem. Roy. Meteor. Soc.*, 3:103–125.

Chipperfield, M. (2006). New version of the TOMCAT/SLIMCAT off-line chemical transport model: Intercomparison of stratospheric tracer experiments. *Quarterly Journal of the Royal Meteorological Society: A journal of the atmospheric sciences, applied meteorology and physical oceanography*, 132(617):1179–1203. https://doi.org/10.1256/qj.05.51.

Chipperfield, M. (2009). Nitrous oxide delays ozone recovery. *Nature Geoscience*, 2(11):742–743. https://doi.org/10.1038/ngeo678.

Chipperfield, M., Cariolle, D., Simon, P., Ramaroson, R., and Lary, D. (1993). A three-dimensional modeling study of trace species in the arctic lower stratosphere during winter 1989–1990. *Journal of Geophysical Research: Atmospheres*, 98(D4):7199–7218. https://doi.org/10.1029/92JD02977.

Chipperfield, M., Hegglin, M., Montzka, S., Newman, P., Park, S., Reimann, S., Rigby, M., Stohl, A., Velders, G., Walter-Terrinoni, H., et al. (2021). Report on unexpected emissions of CFC-11. https://ozone.unep.org/system/files/documents/SAP-2021-report-on-the-unexpected-emissions-of-CFC-11-1268_en.pdf.

Chipperfield, M. P., Santee, M. L., Froidevaux, L., Manney, G. L., Read, W. G., Waters, J. W., Roche, A. E., and Russell, J. M. (1996). Analysis of UARS data in the southern polar vortex in September 1992 using a chemical transport model. *Journal of Geophysical Research: Atmospheres*, 101(D13):18861–18881. https://doi.org/10.1029/96JD00936.

Clerbaux, C., Colin, R., Simon, P. C., and Granier, C. (1993). Infrared cross sections and global warming potentials of 10 alternative hydrohalocarbons. *Journal of Geophysical Research: Atmospheres*, 98(D6):10491–10497. https://doi.org/10.1029/93JD00390.

Crutzen, P. J. (1970). The influence of nitrogen oxides on the atmospheric ozone content. *Quarterly Journal of the Royal Meteorological Society*, 96(408):320–325. https://doi.org/10.1002/qj.49709640815.

Cunnold, D., Steele, L., Fraser, P., Simmonds, P., Prinn, R., Weiss, R., Porter, L., O'Doherty, S., Langenfelds, R., Krummel, P., et al. (2002). In situ measurements of atmospheric methane at GAGE. *Journal of Geophysical Research*, 107(D14). https://doi.org/10.1029/2001JD001226.

Daniel, J., Reimann, S., et al. (2022). Chapter 7: scenarios and information for policymakers. *Scientific Assessment of Ozone Depletion*, pages 385–434. https://csl.noaa.gov/assessments/ozone/2022/.

De Mazière, M., Thompson, A. M., Kurylo, M. J., Wild, J. D., Bernhard, G., Blumenstock, T., Braathen, G. O., Hannigan, J. W., Lambert, J.-C., Leblanc, T., et al. (2018). The Network for the Detection of Atmospheric Composition Change (NDACC): history, status and perspectives. *Atmospheric Chemistry and Physics*, 18(7):4935–4964. https://doi.org/10.5194/acp-18-4935-2018.

Delmas, R., Megie, G., and Peuch, V. (2005). *Physique et chimie de l'atmosphère*. Belin.

Dhomse, S., Feng, W., Montzka, S. A., Hossaini, R., Keeble, J., Pyle, J., Daniel, J., and Chipperfield, M. (2019). Delay in recovery of the Antarctic ozone hole from unexpected CFC-11 emissions. *Nature communications*, 10(5781). https://doi.org/10.1038/s41467-019-13717-x.

Dinelli, B. M., Raspollini, P., Gai, M., Sgheri, L., Ridolfi, M., Ceccherini, S., Barbara, F., Zoppetti, N., Castelli, E., Papandrea, E., et al. (2021). The ESA MIPAS/Envisat level2-v8 dataset: 10 years of measurements retrieved with ORM v8.22. *Atmospheric Measurement Techniques*, 14(12):7975–7998. https://doi.org/10.5194/amt-14-7975-2021.

Dobson, G. M. B. (1956). Origin and distribution of the polyatomic molecules in the atmosphere. *Proceedings of the Royal Society of London. Series A. Mathematical and Physical Sciences*, 236(1205):187–193. https://doi.org/10.1098/rspa.1956.0127.

Dobson, G. M. B., Harrison, D., and Lawrence, J. (1929). Measurements of the amount of ozone in the Earth's atmosphere and its relation to other geophysical conditions. Part III. *Proceedings of the Royal Society of London. Series A, Containing Papers of a Mathematical and Physical Character*, 122(790):456–486. https://doi.org/10.1098/rspa.1929.0034.

Duchatelet, P. (2011). *Fluorine in the atmosphere: Inorganic fluorine budget and long-term trends based on FTIR measurements at Jungfraujoch*. PhD thesis, Université de Liège. Available at https://hdl.handle.net/2268/91413.

EPA (2024). International treaties and cooperation about the protection of the stratospheric ozone layer. https://www.epa.gov/ozone-layer-protection/international-treaties-and-cooperation-about-protection-stratospheric-ozone; Accessed: 2024-10-11.

Farman, J. C., Gardinier, B. G., and Shanklin, J. D. (1985). Large losses of total ozone in Antarctica reveal seasonal ClO_x/NO_x interaction. *Nature*, 315:207–210. https://doi.org/10.1038/315207a0.

Fernando, A. M., Bernath, P. F., and Boone, C. D. (2019). Trends in atmospheric HFC-23 (CHF_3) and HFC-134a abundances. *Journal of Quantitative Spectroscopy and Radiative Transfer*, 238:106540. https://doi.org/10.1016/j.jqsrt.2019.06.019.

Fleming, E. L., Newman, P. A., Liang, Q., and Daniel, J. S. (2020). The impact of continuing CFC-11 emissions on stratospheric ozone. *Journal of Geophysical Research: Atmospheres*, 125(3):00–00. https://doi.org/10.1029/2019JD031849.

Fraser, P., Hyson, P., Enting, I., and Pearman, G. (1983). Global distribution and southern hemispheric trends of atmospheric CCl_3F. *Nature*, 302:692–695. https://doi.org/10.1038/302692a0.

Fraser, P. J., Pearman, G. I., and Derek, N. (2018). CSIRO Non-carbon dioxide greenhouse gas research. Part 1: 1975–90. *Historical Records of Australian Science*, 29(1):1–13. https://doi.org/10.1071/HR17016.

Friedrich, M., Beutner, E., Reuvers, H., Smeekes, S., Urbain, J.-P., Bader, W., Franco, B., Lejeune, B., and Mahieu, E. (2019). Nonparametric estimation and bootstrap inference on trends in atmospheric time series: an application to ethane. *arXiv*. https://doi.org/10.48550/arXiv.1903.05403.

Friedrich, M., Beutner, E., Reuvers, H., Smeekes, S., Urbain, J.-P., Bader, W., Franco, B., Lejeune, B., and Mahieu, E. (2020a). A statistical analysis of time trends in atmospheric ethane. *Climatic Change*, 162(1):105–125. https://doi.org/10.1007/s10584-020-02806-2.

Friedrich, M., Smeekes, S., and Urbain, J.-P. (2020b). Autoregressive wild bootstrap inference for nonparametric trends. *Journal of Econometrics*, 214(1):81–109. https://doi.org/10.1016/j.jeconom.2019.05.006.

García, O. E., Schneider, M., Sepúlveda, E., Hase, F., Blumenstock, T., Cuevas, E., Ramos, R., Gross, J., Barthlott, S., Röhling, A. N., et al. (2021). Twenty years of ground-based NDACC FTIR spectrometry at Izaña Observatory–overview and long-term comparison to other techniques. *Atmospheric Chemistry and Physics*, 21(20):15519–15554. https://doi.org/10.5194/acp-21-15519-2021.

Gardiner, T., Forbes, A., De Mazière, M., Vigouroux, C., Mahieu, E., Demoulin, P., Velazco, V., Notholt, J., Blumenstock, T., Hase, F., et al. (2008). Trend analysis of greenhouse gases over Europe measured by a network of ground-based remote FTIR instruments. *Atmospheric Chemistry and Physics*, 8(22):6719–6727. https://doi.org/10.5194/acp-8-6719-2008.

Gettelman, A., Mills, M., Kinnison, D., Garcia, R., Smith, A., Marsh, D., Tilmes, S., Vitt, F., Bardeen, C., McInerny, J., et al. (2019). The Whole Atmosphere Community Climate Model version 6 (WACCM6). *Journal of Geophysical Research: Atmospheres*, 124(23):12380–12403. https://doi.org/10.1029/2019JD030943.

GML-NOAA (2024). Long-term Observations of Greenhouse gases and Ozone-depleting Substances (LOGOS). https://gml.noaa.gov/hats/; Accessed: 2024-11-04.

Gohar, L., Myhre, G., and Shine, K. (2004). Updated radiative forcing estimates of four halocarbons. *Journal of Geophysical Research: Atmospheres*, 109(D1). https://doi.org/10.1029/2003JD004320.

Gordon, I. E., Rothman, L. S., Hargreaves, R., Hashemi, R., Karlovets, E. V., Skinner, F., Conway, E. K., Hill, C., Kochanov, R. V., Tan, Y., et al. (2022). The HITRAN2020 molecular spectroscopic database. *Journal of Quantitative Spectroscopy and Radiative Transfer*, 277:107949. https://doi.org/10.1016/j.jqsrt.2021.107949.

Griffiths, P. R. and Haseth, J. A. (2007). *Fourier Transform Infrared Spectrometry - Second Edition*. Wiley.

Gueymard, C. A. (2018). A reevaluation of the solar constant based on a 42-year total solar irradiance time series and a reconciliation of spaceborne observations. *Solar Energy*, 168:2–9. https://doi.org/10.1016/j.solener.2018.04.001.

Hannigan, J., Palm, M., Jones, N., Ortega, I., Langerock, B., Mahieu, E., Zhou, M., and Smale, D. (2024). SFIT4 Line-by-line nonlinear spectral fitting software: version 1.0.21 [computer software]. https://wiki.ucar.edu/display/sfit4/SFIT+Core+Code.

Harris, N. R., Wuebbles, D. J., Daniel, J. S., Hu, J., Kuijpers, L. J., Law, K. S., Prather, M. J., and Schofield, R. (2014). Chapter 5: Scenarios and information for policymakers. *Scientific Assessment Ozone Depletion: 2014. Global Ozone Research and monitoring Project-Report N° 55*. https://csl.noaa.gov/assessments/ozone/2014/report/2014OzoneAssessment.pdf.

Harrison, J. J. (2015). Infrared absorption cross sections for 1,1,1,2-tetrafluoroethane. *Journal of Quantitative Spectroscopy and Radiative Transfer*, 151:210–216. https://doi.org/10.1016/j.jqsrt.2014.09.023.

Harrison, J. J., Chipperfield, M. P., Boone, C. D., Dhomse, S. S., and Bernath, P. F. (2021). Fifteen Years of HFC-134a Satellite Observations: Comparisons with SLIMCAT Calculations. *Journal of Geophysical Research: Atmospheres*, 126(8):e2020JD033208. https://doi.org/10.1029/2020JD033208.

Hase, F. (2012). Improved instrumental line shape monitoring for the ground-based, high-resolution FTIR spectrometers of the Network for the Detection of Atmospheric Composition Change. *Atmospheric Measurement Techniques*, 5(3):603–610. https://doi.org/10.5194/amt-5-603-2012.

Hase, F., Blumenstock, T., and Paton-Walsh, C. (1999). Analysis of the instrumental line shape of high-resolution Fourier Transform IR spectrometers with gas cell measurements and new retrieval software. *Applied Optics*, 38(15):3417–3422. https://doi.org/10.1364/AO.38.003417.

Hase, F., Demoulin, P., Sauval, A., Toon, G., Bernath, P., Goldman, A., Hannigan, J., and Rinsland, C. (2006). An empirical line-by-line model for the infrared solar transmittance spectrum from 700 to 5000 cm^{-1}. *Journal of Quantitative Spectroscopy and Radiative Transfer*, 102(3):450–463. https://doi.org/10.1016/j.jqsrt.2006.02.026.

Hase, F., Hannigan, J., Coffey, M., Goldman, A., Höpfner, M., Jones, N., Rinsland, C., and Wood, S. (2004). Intercomparison of retrieval codes used for the analysis of high-resolution, ground-based FTIR measurements. *Journal of Quantitative Spectroscopy and Radiative Transfer*, 87(1):25–52. https://doi.org/10.1016/j.jqsrt.2003.12.008.

Hersbach, H., Bell, B., Berrisford, P., Hirahara, S., Horányi, A., Muñoz-Sabater, J., Nicolas, J., Peubey, C., Radu, R., Schepers, D., et al. (2020). The ERA5 global reanalysis. *Quarterly Journal of the Royal Meteorological Society*, 146(730):1999–2049. https://doi.org/10.1002/qj.3803.

Highwood, E. and Shine, K. P. (2000). Radiative forcing and global warming potentials of 11 halogenated compounds. *Journal of Quantitative Spectroscopy and Radiative Transfer*, 66(2):169–183. https://doi.org/10.1016/S0022-4073(99)00215-0.

Holtslag, A. and Boville, B. (1993). Local versus nonlocal boundary-layer diffusion in a global climate model. *Journal of Climate*, 6(10):1825–1842. https://doi.org/10.1175/1520-0442(1993)006<1825:LVNBLD>2.0.CO;2.

Holzer, M. and Waugh, D. W. (2015). Interhemispheric transit time distributions and path-dependent lifetimes constrained by measurements of SF_6, CFCs, and CFC replacements. *Geophysical Research Letters*, 42(11):4581–4589. https://doi.org/10.1002/2015GL064172.

IPCC (2021). *Climate Change 2021: The Physical Science Basis*. Cambridge University Press, Cambridge, United Kingdom and New York, NY, USA. https://doi.org/10.1017/9781009157896; https://www.ipcc.ch/report/ar6/wg1/.

IPCC (2022). *Climate Change 2022: Mitigation of Climate Change*. Cambridge University Press, Cambridge, United Kingdom and New York, NY, USA. https://www.ipcc.ch/report/ar6/wg3/.

Jacob, D. J. (1999). *Introduction to atmospheric chemistry*. Princeton University Press.

Kalnay, E., Kanamitsu, M., Kistler, R., Collins, W., Deaven, D., Gandin, L., Iredell, M., Saha, S., White, G., Woollen, J., et al. (1996). The NCEP/NCAR 40-year reanalysis project. *Bulletin of the American Meteorological Society*, 77(3):437–472. https://doi.org/10.1175/1520-0477(1996)077<0437:TNYRP>2.0.CO;2.

Kohlhepp, R., Ruhnke, R., Chipperfield, M. P., De Mazière, M., Notholt, J., Barthlott, S., Batchelor, R. L., Blatherwick, R. D., Blumenstock, T., Coffey, M., et al. (2012). Observed and simulated time evolution of HCl, $ClONO_2$, and HF total column abundances. *Atmospheric Chemistry and Physics*, 12(7):3527–3556. https://doi.org/10.5194/acp-12-3527-2012.

Kurylo, M. J. (1991). Network for the Detection of Stratospheric Change. *Remote Sensing of Atmospheric Chemistry*, 1491:168–174. https://doi.org/10.1117/12.46658.

Lachance, R. L., Buijs, H. L., and Soucy, M.-A. (2013). ACE-FTS on SCISAT: 10th year on-orbit anniversary. *Proc. SPIE 8867, Infrared Remote Sensing and Instrumentation XXI, 88670J*, 8867:141–154. https://doi.org/10.1117/12.2024985.

Liang, Q., Rigby, M., et al. (2022). Chapter 2: Hydrofluorocarbons (HFCs). *Scientific Assessment of Ozone Depletion*, pages 115–151. https://csl.noaa.gov/assessments/ozone/2022/.

Lickley, M., Solomon, S., Fletcher, S., Velders, G. J., Daniel, J., Rigby, M., Montzka, S. A., Kuijpers, L. J., and Stone, K. (2020). Quantifying contributions of chlorofluorocarbon banks to emissions and impacts on the ozone layer and climate. *Nature Communications*, 11(1380). https://doi.org/10.1038/s41467-020-15162-7.

Lutgens, F. and Tarbuck, E. (2001). *The atmosphere : an introduction to meteorology. 8th edition*. Prentice Hall.

Mahieu, E., Bader, W., Bovy, B., Demoulin, P., Flock, O., Franco, B., Lejeune, B., Prignon, M., Roland, G., and Servais, C. (2017). Surveillance de l'atmosphère terrestre depuis la station du Jungfraujoch : une épopée liègeoise entamée voici plus de 65 ans ! *Bulletin de la Société Géographique de Liège*, 68:119–130.

Mahieu, E., Fischer, E. V., Franco, B., Palm, M., Wizenberg, T., Smale, D., Clarisse, L., Clerbaux, C., Coheur, P.-F., Hannigan, J. W., et al. (2021). First retrievals of peroxyacetyl nitrate (PAN) from ground-based FTIR solar spectra recorded at remote sites, comparison with model and satellite data. *Elem Sci Anth*, 9(1):00027. https://doi.org/10.1525/elementa.2021.00027.

Mahieu, E., Flock, O., Notholt, J., Palm, M., Pardo Cantos, I., Prignon, M., Roland, G., Servais, C., and Verma, A. (2019). Surveillance à long terme de l'atmosphère terrestre à la station du Jungfraujoch. *Bulletin de la Société Royale des Sciences de Liège*, 88:31–41. https://doi.org/10.25518/0037-9565.9136.

Makkor, J., Palm, M., Buschmann, M., Mahieu, E., Chipperfield, M., and Notholt, J. (2025). Digitization and calibration of historical solar absorption infrared spectra from the Jungfraujoch site. *Atmospheric Measurement Techniques Discussions*. https://doi.org/10.5194/amt-2024-93.

Marsh, D. R., Mills, M. J., Kinnison, D. E., Lamarque, J.-F., Calvo, N., and Polvani, L. M. (2013). Climate change from 1850 to 2005 simulated in CESM1 (WACCM). *Journal of Climate*, 26(19):7372–7391. https://doi.org/10.1175/JCLI-D-12-00558.1.

Meier, A. (1997). *Determination of atmospheric trace gas amounts and corresponding natural isotopic ratios by means of ground-based FTIR spectroscopy in the high Arctic*. PhD thesis, Technical University of Braunschweig.

Migeotte, M. V. (1948). Spectroscopic evidence of methane in the Earth's atmosphere. *Physical Review*, 73(5):519. https://doi.org/10.1103/PhysRev.73.519.2.

Migeotte, M. V. (1949). The fundamental band of carbon monoxide at 4.7 μ in the solar spectrum. *Physical Review*, 75(7):1108. https://doi.org/10.1103/PhysRev.75.1108.

Miller, B. R., Weiss, R. F., Salameh, P. K., Tanhua, T., Greally, B. R., Mühle, J., and Simmonds, P. G. (2008). Medusa: A sample preconcentration and GC/MS detector system for in situ measurements of atmospheric trace halocarbons, hydrocarbons, and sulfur compounds. *Analytical Chemistry*, 80(5):1536–1545. https://doi.org/10.1021/ac702084k.

Molina, M. J. and Rowland, F. S. (1974). Stratospheric sink for chlorofluoromethanes: chlorine atom-catalysed destruction of ozone. *Nature*, 249:810–812. https://doi.org/10.1038/249810a0.

Montzka, S., McFarland, M., Andersen, S., Miller, B., Fahey, D., Hall, B., Hu, L., Siso, C., and Elkins, J. (2015). Recent trends in global emissions of hydrochlorofluorocarbons and hydrofluorocarbons: Reflecting on the 2007 adjustments to the Montreal Protocol. *The Journal of Physical Chemistry A*, 119(19):4439–4449. https://doi.org/10.1021/jp5097376.

Montzka, S., Myers, R., Butler, J., Elkins, J., Lock, L., Clarke, A., and Goldstein, A. (1996). Observations of HFC-134a in the remote troposphere. *Geophysical research letters*, 23(2):169–172. https://doi.org/10.1029/95GL03590.

Montzka, S. A., Dutton, G. S., Portmann, R. W., Chipperfield, M. P., Davis, S., Feng, W., Manning, A. J., Ray, E., Rigby, M., Hall, B. D., et al. (2021). A decline in global CFC-11 emissions during 2018–2019. *Nature*, 590:428–432. https://doi.org/10.1038/s41586-021-03260-5.

Montzka, S. A., Dutton, G. S., Yu, P., Ray, E., Portmann, R. W., Daniel, J. S., Kuijpers, L., Hall, B. D., Mondeel, D., Siso, C., et al. (2018). An unexpected and persistent increase in global emissions of ozone-depleting CFC-11. *Nature*, 557:413–417. https://doi.org/10.1038/s41586-018-0106-2.

Nemtchinov, V. and Varanasi, P. (2004). Absorption cross-sections of HFC-134a in the spectral region between 7 and 12 μm. *Journal of Quantitative Spectroscopy and Radiative Transfer*, 83(3-4):285–294. https://doi.org/10.1016/S0022-4073(02)00356-4.

O'Doherty, S., Simmonds, P., Cunnold, D., Wang, H., Sturrock, G., Fraser, P., Ryall, D., Derwent, R., Weiss, R., Salameh, P., et al. (2001). In situ chloroform measurements at Advanced Global Atmospheric Gases Experiment atmospheric research stations from 1994 to 1998. *Journal of Geophysical Research: Atmospheres*, 106(D17):20429–20444. https://doi.org/10.1029/2000JD900792.

Pardo Cantos, I., Mahieu, E., Chipperfield, M. P., Servais, C., Reimann, S., and Vollmer, M. K. (2024). First HFC-134a retrievals from ground-based FTIR solar absorption spectra, comparison with TOMCAT model simulations, *in-situ* AGAGE observations, and ACE-FTS satellite data for the Jungfraujoch station. *Journal of Quantitative Spectroscopy and Radiative Transfer*, 318. https://doi.org/10.1016/j.jqsrt.2024.108938.

Pardo Cantos, I., Mahieu, E., Chipperfield, M. P., Smale, D., Hannigan, J. W., Friedrich, M., Fraser, P., Krummel, P., Prignon, M., Makkor, J., et al. (2022). Determination and analysis of time series of CFC-11 (CCl_3F) from FTIR solar spectra, in situ observations, and model data in the past 20 years above Jungfraujoch (46°N), Lauder (45°S), and Cape Grim (40°S) stations. *Environmental Science: Atmospheres*, 2(6):1487–1501. https://doi.org/10.1039/D2EA00060A.

Park, S., Western, L. M., Saito, T., Redington, A. L., Henne, S., Fang, X., Prinn, R. G., Manning, A. J., Montzka, S. A., Fraser, P. J., et al. (2021). A decline in emissions of CFC-11 and related chemicals from eastern China. *Nature*, 590:433–437. https://doi.org/10.1038/s41586-021-03277-w.

Paton-Walsh, C. (2011). Remote sensing of atmospheric trace gases by ground-based solar Fourier Transform Infrared spectroscopy. *Fourier Transforms-New Analytical Approaches and FTIR Strategies*, pages 459–478. https://doi.org/10.5772/15257.

Patra, P., Takigawa, M., Dutton, G., Uhse, K., Ishijima, K., Lintner, B., Miyazaki, K., and Elkins, J. (2009). Transport mechanisms for synoptic, seasonal and interannual SF_6 variations and "age" of air in troposphere. *Atmospheric Chemistry and Physics*, 9(4):1209–1225. https://doi.org/10.5194/acp-9-1209-2009.

Polvani, L. M., Abalos, M., Garcia, R., Kinnison, D., and Randel, W. J. (2018). Significant weakening of Brewer-Dobson circulation trends over the 21st century as a consequence of the Montreal Protocol. *Geophysical Research Letters*, 45(1):401–409. https://doi.org/10.1002/2017GL075345.

Polyakov, A., Poberovsky, A., Makarova, M., Virolainen, Y., Timofeyev, Y., and Nikulina, A. (2021). Measurements of CFC-11, CFC-12, and HCFC-22 total columns in the atmosphere at the St. Petersburg site in 2009–2019. *Atmospheric Measurement Techniques*, 14(8):5349–5368. https://doi.org/10.5194/amt-14-5349-2021.

Prignon, M. (2021). *Stratospheric circulation changes: investigations using multidecadal observations and simulations of inorganic fluorine*. PhD thesis, Université de Liège. Available at https://hdl.handle.net/2268/260555.

Prignon, M., Chabrillat, S., Friedrich, M., Smale, D., Strahan, S., Bernath, P. F., Chipperfield, M., Dhomse, S., Feng, W., Minganti, D., et al. (2021). Stratospheric fluorine as a tracer of circulation changes: Comparison between infrared remote-sensing observations and simulations with five modern reanalyses. *Journal of Geophysical Research: Atmospheres*, 126(19). https://doi.org/10.1029/2021JD034995.

Prignon, M., Chabrillat, S., Minganti, D., O'Doherty, S., Servais, C., Stiller, G., Toon, G. C., Vollmer, M. K., and Mahieu, E. (2019). Improved FTIR retrieval strategy for HCFC-22

($CHClF_2$), comparisons with in situ and satellite datasets with the support of models, and determination of its long-term trend above Jungfraujoch. *Atmospheric Chemistry and Physics*, 19(19):12309–12324. https://doi.org/10.5194/acp-19-12309-2019.

Prinn, R., Simmonds, P., Rasmussen, R., Rosen, R., Alyea, F., Cardelino, C., Crawford, A., Cunnold, D., Fraser, P., and Lovelock, J. (1983). The atmospheric lifetime experiment: 1. introduction, instrumentation, and overview. *Journal of Geophysical Research: Oceans*, 88(C13):8353–8367. https://doi.org/10.1029/JC088iC13p08353.

Prinn, R., Weiss, R., Fraser, P., Simmonds, P., Cunnold, D., Alyea, F., O'Doherty, S., Salameh, P., Miller, B., Huang, J., et al. (2000). A history of chemically and radiatively important gases in air deduced from ALE/GAGE/AGAGE. *Journal of Geophysical Research: Atmospheres*, 105(D14):17751–17792. https://doi.org/10.1029/2000JD900141.

Prinn, R. G., Weiss, R. F., Arduini, J., Arnold, T., DeWitt, H. L., Fraser, P. J., Ganesan, A. L., Gasore, J., Harth, C. M., Hermansen, O., et al. (2018). History of chemically and radiatively important atmospheric gases from the Advanced Global Atmospheric Gases Experiment (AGAGE). *Earth System Science Data*, 10(2):985–1018. https://doi.org/10.5194/essd-10-985-2018.

Ravishankara, A., Daniel, J. S., and Portmann, R. W. (2009). Nitrous oxide (N_2O): the dominant ozone-depleting substance emitted in the 21st century. *Science*, 326(5949):123–125. https://doi.org/10.1126/science.1176985.

Reimann, S., Vollmer, M. K., Hill, M., Schlauri, P., Guillevic, M., Brunner, D., Henne, S., Rust, D., and Emmenegger, L. (2020). Long-term observations of atmospheric halogenated organic trace gases. *Chimia*, 74(3):136–136. https://doi.org/10.2533/chimia.2020.136.

Rigby, M., Park, S., Saito, T., Western, L. M., Redington, A. L., Fang, X., Henne, S., Manning, A. J., Prinn, R. G., Dutton, G. S., et al. (2019). Increase in CFC-11 emissions from eastern China based on atmospheric observations. *Nature*, 569:546–550. https://doi.org/10.1038/s41586-019-1193-4.

Robinson, J., Smale, D., Pollard, D., and Shiona, H. (2020). Solar tracker with optical feedback and continuous rotation. *Atmospheric Measurement Techniques*, 13(11):5855–5871. https://doi.org/10.5194/amt-13-5855-2020.

Rodgers, C. D. (2000). *Inverse methods for atmospheric sounding: theory and practice*, volume 2. World scientific.

Ronsmans, G., Langerock, B., Wespes, C., Hannigan, J. W., Hase, F., Kerzenmacher, T., Mahieu, E., Schneider, M., Smale, D., Hurtmans, D., et al. (2016). First characterization and validation of FORLI-HNO_3 vertical profiles retrieved from IASI/Metop. *Atmospheric Measurement Techniques*, 9(9):4783–4801. https://doi.org/10.5194/amt-9-4783-2016.

Rothman, L. S., Gordon, I. E., Babikov, Y., Barbe, A., Benner, D. C., Bernath, P. F., Birk, M., Bizzocchi, L., Boudon, V., Brown, L. R., et al. (2013). The HITRAN2012 molecular spectroscopic database. *Journal of Quantitative Spectroscopy and Radiative Transfer*, 130:4–50. https://doi.org/10.1016/j.jqsrt.2013.07.002.

Rothman, L. S., Gordon, I. E., Barbe, A., Benner, D. C., Bernath, P. F., Birk, M., Boudon, V., Brown, L. R., Campargue, A., Champion, J.-P., et al. (2009). The HITRAN2008 molecular spectroscopic database. *Journal of Quantitative Spectroscopy and Radiative Transfer*, 110(9-10):533–572. https://doi.org/10.1016/j.jqsrt.2009.02.013.

Salawitch, R. J., McBride, L. A., Thompson, C. R., Fleming, E. L., McKenzie, R. L., Rosenlof, K. H., Doherty, S. J., and Fahey, D. W. (2022). *Twenty Questions and Answers About the Ozone Layer: 2022 Update, Scientific Assessment of Ozone Depletion: 2022*. World Meteorological Organization. https://ozone.unep.org/sites/default/files/2023-05/Final_20Qs%202022%20full%20document_26April2023_digital%20version.pdf.

Schuck, T. J., Degen, J., Hintsa, E., Hoor, P., Jesswein, M., Keber, T., Kunkel, D., Moore, F., Obersteiner, F., Rigby, M., Wagenhäuser, T., Western, L. M., Zahn, A., and Engel, A. (2024). The interhemispheric gradient of SF_6 in the upper troposphere. *Atmospheric Chemistry and Physics*, 24:689–705. https://doi.org/10.5194/acp-24-689-2024.

Sharpe, S. W., Johnson, T. J., Sams, R. L., Chu, P. M., Rhoderick, G. C., and Johnson, P. A. (2004). Gas-phase databases for quantitative infrared spectroscopy. *Applied spectroscopy*, 58(12):1452–1461. https://doi.org/10.1366/0003702042641281.

Shepherd, T. G. (2003). Large-scale atmospheric dynamics for atmospheric chemists. *Chemical reviews*, 103(12):4509–4532. https://doi.org/10.1021/cr020511z.

Simmonds, P., O'Doherty, S., Nickless, G., Sturrock, G., Swaby, R., Knight, P., Ricketts, J., Woffendin, G., and Smith, R. (1995). Automated gas chromatograph/mass spectrometer for routine atmospheric field measurements of the CFC replacement compounds, the hydrofluorocarbons and hydrochlorofluorocarbons. *Analytical Chemistry*, 67(4):717–723. https://doi.org/10.1021/ac00100a005.

SPARC (2013). SPARC Report on the Lifetimes of Stratospheric Ozone-Depleting Substances, Their Replacements, and Related Species. No. 6:256 pp. http://www.sparc-climate.org/publications/sparc-reports/.

Stolarski, R. S. and Cicerone, R. J. (1974). Stratospheric chlorine: a possible sink for ozone. *Canadian Journal of Chemistry*, 52(8):1610–1615. https://doi.org/10.1139/v74-233.

Sussmann, R., Borsdorff, T., Rettinger, M., Camy-Peyret, C., Demoulin, P., Duchatelet, P., Mahieu, E., and Servais, C. (2009). Harmonized retrieval of column-integrated atmospheric water vapor from the FTIR network–first examples for long-term records and station trends. *Atmospheric Chemistry and Physics*, 9(22):8987–8999. https://doi.org/10.5194/acp-9-8987-2009.

Tiedtke, M. (1989). A comprehensive mass flux scheme for cumulus parameterization in large-scale models. *Monthly weather review*, 117(8):1779–1800. https://doi.org/10.1175/1520-0493(1989)117<1779:ACMFSF>2.0.CO;2.

Tikhonov, A., Goncharsky, A., Stepanov, V., and Yagola, A. (1995). *Numerical methods for the approximate solution of ill-posed problems on compact sets*. Springer.

UCAR (2024). Center for science education - learning zone. https://scied.ucar.edu/learning-zone/; Accessed: 09/11/2024.

UNEP (2020). The Montreal Protocol on Substances that Deplete the Ozone Layer. https://ozone.unep.org/treaties/montreal-protocol; Accessed: 2024-10-11.

UWaterloo (2024). Atmospheric chemistry experiment. https://uwaterloo.ca/atmospheric-chemistry-experiment/; Accessed: 2024-12-10.

Velders, G. J., Daniel, J. S., Montzka, S. A., Vimont, I., Rigby, M., Krummel, P. B., Muhle, J., O'Doherty, S., Prinn, R. G., Weiss, R. F., et al. (2022). Projections of hydrofluorocarbon (HFC) emissions and the resulting global warming based on recent trends in observed abundances and current policies. *Atmospheric Chemistry and Physics*, 22(9):6087–6101. https://doi.org/10.5194/acp-22-6087-2022.

Velders, G. J., Fahey, D. W., Daniel, J. S., Andersen, S. O., and McFarland, M. (2015). Future atmospheric abundances and climate forcings from scenarios of global and regional hydrofluorocarbon (HFC) emissions. *Atmospheric Environment*, 123:200–209. https://doi.org/10.1016/j.atmosenv.2015.10.071.

Vigouroux, C., Blumenstock, T., Coffey, M., Errera, Q., García, O., Jones, N. B., Hannigan, J., Hase, F., Liley, B., Mahieu, E., et al. (2015). Trends of ozone total columns and vertical distribution from FTIR observations at eight NDACC stations around the globe. *Atmospheric Chemistry and Physics*, 15(6):2915–2933. https://doi.org/10.5194/acp-15-2915-2015.

Waugh, D. and Hall, T. (2002). Age of stratospheric air: Theory, observations, and models. *Reviews of Geophysics*, 40(4):1–26. https://doi.org/10.1029/2000RG000101.

WMO (2018). Scientific assessment of ozone depletion: 2018, global ozone research and monitoring project, Report no. 58. https://csl.noaa.gov/assessments/ozone/2018/.

WMO (2022). Scientific Assessment of Ozone Depletion: 2022, ozone research and monitoring, Report no. 278. https://csl.noaa.gov/assessments/ozone/2022/.

Zander, R., Duchatelet, P., Mahieu, E., Demoulin, P., Roland, G., Servais, C., Auwera, J. V., Perrin, A., Rinsland, C., and Crutzen, P. (2010). Formic acid above the Jungfraujoch during 1985–2007: observed variability, seasonality, but no long-term background evolution. *Atmospheric Chemistry and Physics*, 10(20):10047–10065. https://doi.org/10.5194/acp-10-10047-2010.

Zander, R., Mahieu, E., Demoulin, P., Duchatelet, P., Roland, G., Servais, C., De Mazière, M., Reimann, S., and Rinsland, C. P. (2008). Our changing atmosphere: Evidence based on long-term infrared solar observations at the Jungfraujoch since 1950. *Science of the total environment*, 391(2-3):184–195. https://doi.org/10.1016/j.scitotenv.2007.10.018.

Zander, R., Mahieu, E., Gunson, M., Abrams, M., Chang, A., Abbas, M., Aellig, C., Engel, A., Goldman, A., Irion, F., et al. (1996). The 1994 northern midlatitude budget of stratospheric chlorine derived from ATMOS/ATLAS-3 observations. *Geophysical Research Letters*, 23(17):2357–2360. https://doi.org/10.1029/96GL01792.

Zander, R., Stokes, G. M., and Brault, J. W. (1983). Simultaneous detection of FC-11, FC-12 and FC-22, through 8 to 13 Micrometers IR solar observations from the ground. *Geophysical research letters*, 10(7):521–524. https://doi.org/10.1029/GL010i007p00521.

Zhou, M., Vigouroux, C., Langerock, B., Wang, P., Dutton, G., Hermans, C., Kumps, N., Metzger, J.-M., Toon, G., and De Mazière, M. (2016). CFC-11, CFC-12 and HCFC-22 ground-based remote sensing FTIR measurements at Réunion Island and comparisons with MIPAS/ENVISAT data. *Atmospheric Measurement Techniques*, 9(11):5621–5636. https://doi.org/10.5194/amt-9-5621-2016.